Journal of Materials Chemistry C

ROYAL SOCIETY OF CHEMISTRY

REVIEW

View Article Online
View Journal | View Issue

Check for updates

Cite this: J. Mater. Chem. C, 2025, 13, 9410

Chiral lanthanide complexes in the history of circularly polarized luminescence: a brief summary

Diksha Thakur and Sivakumar Vaidyanathan *

Received 9th January 2025,
Accepted 27th March 2025

DOI: 10.1039/d5tc00097a

rsc.li/materials-c

Circularly polarized luminescence (CPL) has attracted considerable attention owing to its potential applications in practical life. Although CPL can be generated using a linear polarizer and a quarter-wave plate combination, the generated light emerges by compromising the total output brightness. Therefore, the above-mentioned drawback has led to the development of original CPL emitters. In this perspective, the CPL-based research field continues to flourish, and many CPL emissive small organic molecules, supramolecular assemblies, nano-assemblies, and metal complexes have been explored. The dissymmetry factor (g_{lum}) is the measure of the extent of circular polarization of light. Chiral organic small molecules possess very small g_{lum} values. The chiral lanthanide (Ln) complexes are ideal molecular structures to depict the high luminescence dissymmetry factor (g_{lum}). These Ln complexes have forbidden electric-dipole and allowed magnetic dipole 4f–4f transitions, which make them weak emissive candidates. However, the rational design of the antenna ligands can effectively transfer the energy to Ln metal ions and lower the symmetry of the overall complex, making the electric dipole 4f–4f transition partly allowed. This mini-review article presents the basic principles and key factors for assessing the CPL activity in the chiral Ln complexes. It discusses small Ln complexes with various antenna ligands and distinct chirality induction from the chiral ligands to metal complexes. Furthermore, it briefly examines the rational ligand design and the future uses of chiral Ln metal complexes. Finally, different types of CPL spectrometers are elaborately discussed.

Open Access Article. Published on 02 April 2025. Downloaded on 4/4/2026 1:46:32 AM.
This article is licensed under a Creative Commons Attribution-NonCommercial 3.0 Unported Licence.

1. Introduction

Concept of chirality comes into the picture when an object cannot superimpose on its mirror image. Chiral objects are observed around us in any field of science or the practical world, ranging from microscopic to macroscopic levels.[1] From chiral molecular centers in chemistry to electromagnetism (circularly polarized luminescence, CPL) in physics and practical life, such as human hands, billions of things cannot be superimposed on their mirror images. The chiral systems have their benefits, such as performance in drug activity and enzyme specificity. Chiral objects are all around us in daily life—from the asymmetry of our hands to the chirality of amino acids, proteins, sugars, and even the taste, smell, and effects of certain drugs and household items. Chirality can be mainly divided into five parts: point, axial, planar, helical, and propeller (Fig. 1).[2,3]

Point chirality is generally related to carbon atoms and arises when connected to four different groups. Axial chirality arises due to the spatial arrangement of groups around an axis. Examples of axially chiral systems include organic molecules, such as allenes, biaryls, and certain alkenes, having restricted rotation around a bond. Helical chirality arises from the spiral-like arrangement of atoms in a molecule. This property is commonly observed in DNA, helicenes, and inorganic complexes. Planar chirality arises in systems due to the spatial arrangement of atoms or groups in a planar structure. Symmetry plane is disrupted in this case, leading to non-superimposable mirror images. Cyclophanes, allenyls, and different types of macrocyclic rings show this type of chirality. In propeller chirality, a molecule or complex adopts a propeller-like shape, and the substituents around the central axis are arranged in a helical or twisted manner, resulting in non-superimposable mirror images.

CPL is the emission of either left-handed or right-handed light in the chiral luminescence systems.[4,5] CPL materials have gained popularity for sophisticated applications such as optical information storage, chiral recognition, 3D display, smart sensors *etc.*[6–8] Many articles have been published recently with a focus on CPL.[9–15] CPL can be generated by combining a linear polarizer and a quarter wave plate (Fig. 3a).[3] Shifting the phase between the two orthogonal components of linearly polarized light generates circularly polarized light. Generally, non-polarized light is passed through a linear polarizer to produce linear polarized light. This linearly polarized light is made to pass through a quarter wave

Department of Chemistry, Indian Institute of Technology Hyderabad, Sangareddy, Kandi, Telangana 502285, India. E-mail: vsiva@chy.iith.ac.in

This journal is © The Royal Society of Chemistry 2025

Open Access Article. Published on 02 April 2025. Downloaded on 4/4/2026 1:46:32 AM.
This article is licensed under a Creative Commons Attribution-NonCommercial 3.0 Unported Licence.

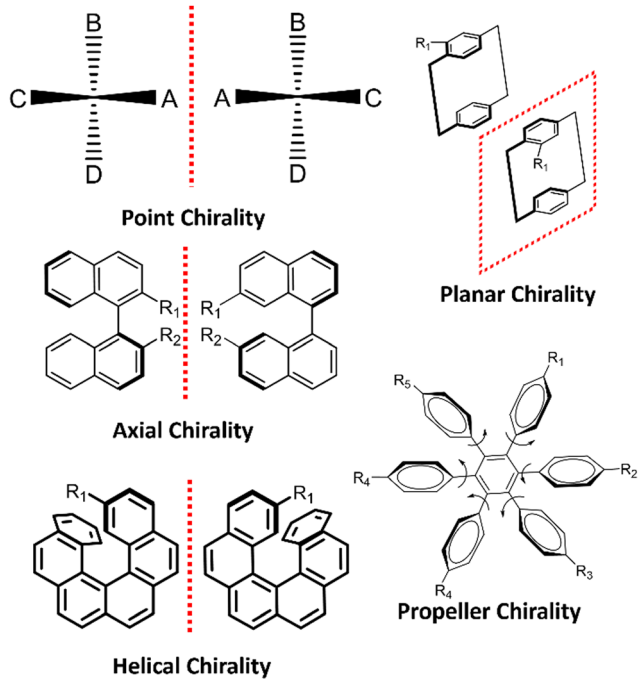

Fig. 1 Different types of chirality [redrawn from ref. 3].

plate placed at an angle of 45° to its optical axis.[3] Right and left-handed CP light can be produced by adjusting the orientation and phase relationship of the light components.

Most display devices use antiglare filters to reduce the reflection from external light (Fig. 2).[16] The anti-glare filters are made by connecting the linear polarizer with the quarter-wave plate. At the same time, this anti-glare filter reduces almost 50% of light generated by normal organic light-emitting diode (OLED) devices (Fig. 2). Using CPL emitter-based OLEDs/LEDs results in less attenuation of the emitted light, leading to very bright images with low power consumption.[3]

In recent years, there has been an increased interest in synthesizing organic compounds capable of generating CPL for possible use in optoelectronic devices.[5] A quarter-wave plate can convert linearly polarized light into CP light.[17] However, this results in low transformation efficiency due to absorption and reflection of incident light.[17] Therefore, chiral luminescent materials (organic and inorganic) are preferred to produce CP light. Mirror-structured enantiomers emit left and right-handed CP light when excited by a suitable source.[17] Various chiral luminous materials, including lanthanide complexes, have been extensively studied to generate CP light.[17,18]

As mentioned earlier, CPL can be considered an emerging technology in biomedical imaging, diagnostics, organic optoelectronics, *etc.*[19,20] CPL is increasingly used in OLEDs, lasers, and displays. Circular polarization can advance the efficiency and performance of devices. This leads to brighter, more color-pure displays and light sources. CPL also has potential significance in developing advanced chiral sensors for detecting specific enantiomers. Moreover, the selective polarization properties open pathways for quantum computing and encryption technologies. He *et al.* highlighted the challenge of achieving high emission efficiency and a large luminescence asymmetry factor (g_{lum}) in a single molecule.[21] They developed a liquid-

Diksha Thakur

Diksha Thakur completed her PhD at the School of Chemical Sciences, Indian Institute of Technology, Mandi, with Prof. Subrata Ghosh in 2023. Her research interests include synthesizing small organic conjugated materials for application in OLEDs. She joined as a national post-doctoral fellow at the Indian Institute of Technology, Hyderabad, with Dr Sivakumar Vaidyanathan, where she is currently working on chiral TADF materials.

Sivakumar Vaidyanathan

Prof. Sivakumar Vaidyanathan received his bachelor's and master's degrees in chemistry from Muthurangam Government Arts College, Vellore (affiliated with the University of Madras), and his PhD in solid-state chemistry (2007) from the Indian Institute of Technology, Madras, with Prof. U. V. Varadaraju. Then, he moved to Prof. Duk Young Jeon's group at the Korea Advanced Institute of Science and Technology, Republic of Korea, as a brain Korea 21 post-doctoral research fellow (2007–2009). He also worked for a year as a post-doctoral fellow at the Commissariat à l'Énergie Atomique (CEA), Saclay, France. After spending a decade at NIT Rourkela as a faculty member in the department of chemistry, he moved to the department of chemistry at the Indian Institute of Technology Hyderabad. His research focuses on lanthanide photochemistry and photophysics, molecular materials (including deep blue) for organic light emitting diodes (OLEDs), pure organic room temperature phosphorescence materials, phosphors for LEDs (solid-state lighting), and NIR-II dyes for biomedical and organic fluorophores for diverse applications.

Open Access Article. Published on 02 April 2025. Downloaded on 4/4/2026 1:46:32 AM.
This article is licensed under a Creative Commons Attribution-NonCommercial 3.0 Unported Licence.

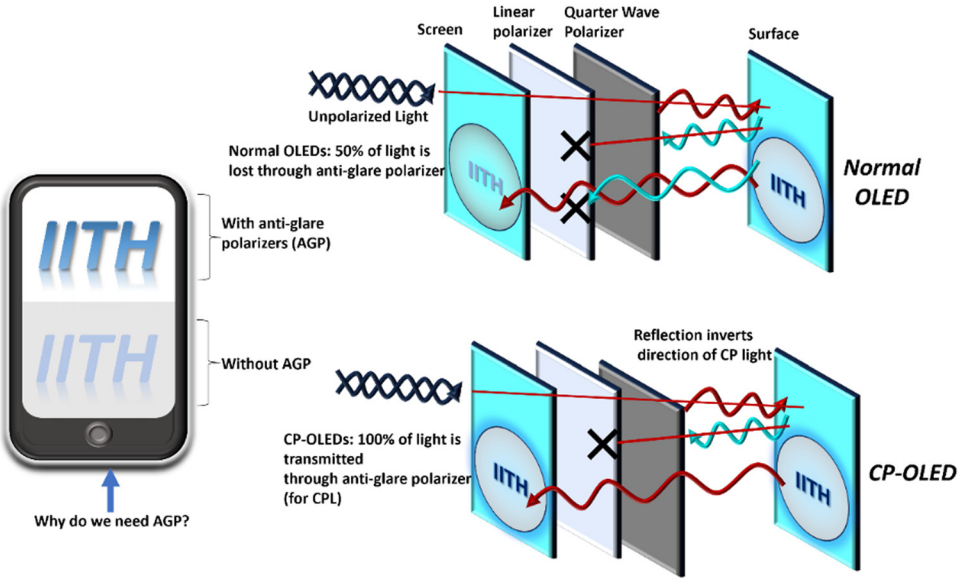

Fig. 2 Diagram depicting the benefits of CP-OLEDs over normal OLEDs [redrawn from ref. 16].

crystalline CP-TADF molecule with a high g_{lum} value of 0.11, demonstrating these materials' potential in practical applications. Further, they fabricated the solution-processed devices using the synthesized compounds as dopants. The devices depicted a very high maximum external quantum efficiency (EQE) of 21.2%. Liao *et al.* developed a planar chiral [2.2]paracyclophane-based TADF molecule.[22] They combined a bulky planar chiral phenoxazine-phane donor with a triazine acceptor to achieve high luminescence performance and excellent CPL properties. They fabricated the CP-OLED devices using the developed chiral emitters and could achieve a maximum brightness of up to 34 293 cd m^{-2} and a maximum EQE of 7.8%. Qu *et al.* designed and synthesized intrinsically chiral biphenoxazine-based TADF materials with potential application in CP-OLEDs.[23] They used an axially chiral electron-donor biphenoxazine core combined with two electron-acceptor fragments, 2,4,6-triphenyl-*s*-triazine. They fabricated the solution-processed CP-OLEDs and achieved a luminance of 1.66 × 10^4 cd m^{-2}, current efficiency of 35.2 cd A^{-1}, EQE of 11.3%, and a dissymmetry factor of 0.88 × 10^{-3}.

Circular dichroism (CD) and CPL spectroscopic techniques are two methods that are used to quantify the extent of circular polarization. The pictorial representations of CD and CPL mechanisms are given below in Fig. 3b and c. The CD measures differences in the absorption of left-handed (L) CPL and right-handed (R) CPL by chiral molecules. The extent of absorption of L-CPL and R-CPL differs for chiral molecules. This difference arises as the chiral molecule interacts differently with the L- and R-CPL. A CD spectrum comprises a plot of the difference in absorption of L and R-CPL against the wavelength of light. The peaks in the CD plot represent wavelengths where the molecule absorbs L-CPL and R-CPL differently. The positive peaks depict that the chiral molecule absorbs more L-CPL, while negative peaks show greater absorption of R-CPL. CPL spectroscopy is a technique that measures the difference in the emission of L-CPL and R-CPL from a chiral molecule after excitation. The chiral molecules emit either L-CPL or R-CPL.

CD spectroscopy typically measures molar circular dichroism ($\Delta\varepsilon$) as a function of wavelength.[3] The absorptive dissymmetry factor (g_{abs}) can be defined by the following equations:[3]

$$\Delta\varepsilon = \varepsilon_L - \varepsilon_R \quad (1)$$

$$g_{abs} = (\varepsilon_L - \varepsilon_R)/\varepsilon \quad (2)$$

ε_L = extinction coefficient for L-CPL, ε_R = extinction coefficient for R-CPL.

Also,

$$\varepsilon = (\varepsilon_L + \varepsilon_R)/2 \quad (3)$$

Therefore,

$$g_{abs} = 2(\varepsilon_L - \varepsilon_R)/(\varepsilon_L + \varepsilon_R) \quad (4)$$

Experimentally, g_{abs} can be calculated as

$$g_{abs} = \text{ellipiticity}/(\text{absorbance} \times 32\,980) \quad (5)$$

The ellipticity and absorbance can be obtained from CD spectra.[3]

In CPL spectroscopy, the emission intensity (ΔI) difference between L- and R-CPL is defined as follows.[3]

$$\Delta I = I_L - I_R \quad (6)$$

$$g_{lum} = 2(I_L - I_R)/(I_L + I_R) \quad (7)$$

where

$$I_L = \text{L-CPL};\ I_R = \text{R-CPL} \quad (8)$$

However, determining absolute I and ΔI values is challenging. The luminescence dissymmetry factor (g_{lum}) measures the degree of dissymmetry in CPL as given in the above equation.[3] It is clear from the g_{abs} and g_{lum} that the CD and CPL values vary

 This journal is © The Royal Society of Chemistry 2025

Open Access Article. Published on 02 April 2025. Downloaded on 4/4/2026 1:46:32 AM.
This article is licensed under a Creative Commons Attribution-NonCommercial 3.0 Unported Licence.

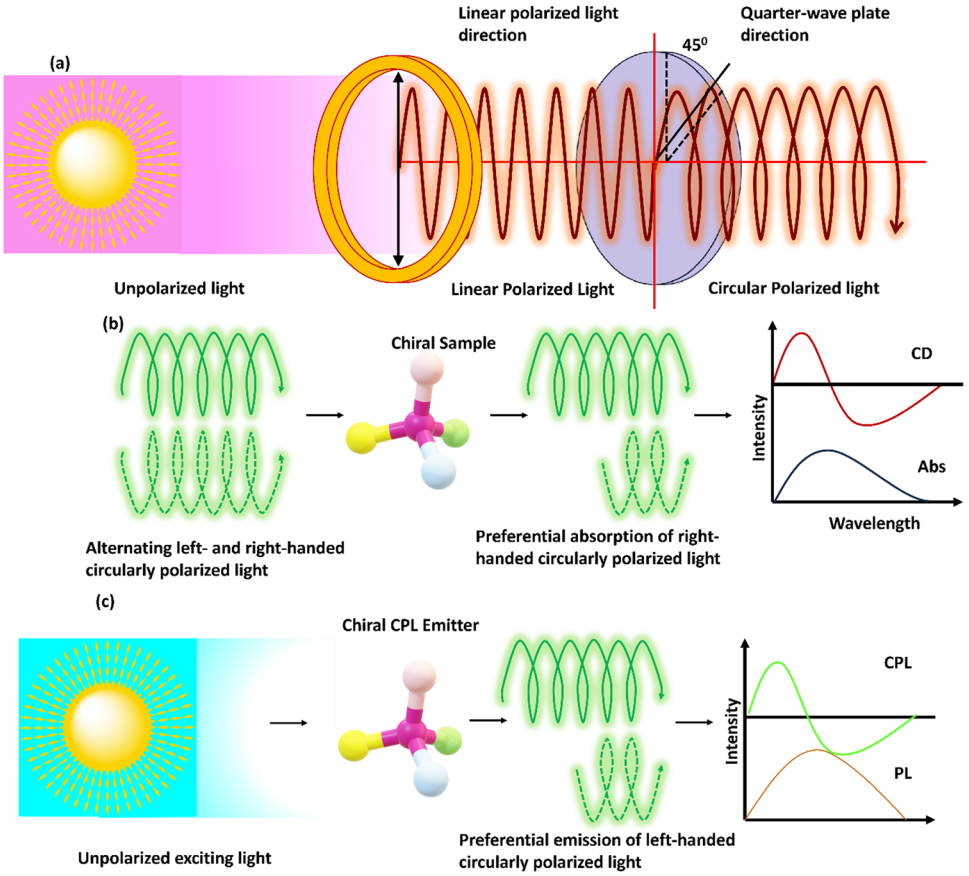

Fig. 3 (a) Mechanism of generating circularly polarized luminescence (CPL) from unpolarized light with the help of a quarter wave plate; (b) illustration of circular dichroism (CD) mechanism; and (c) illustration of CPL mechanisms [redrawn from ref. 3].

from +2 to −2. A maximum value of $g_{lum} = \pm 2$ indicates optimal left- and right-handed polarization of emitted light, whereas $g_{lum} = 0$ indicates no circular polarization of light.[3]

The rotatory strength R theoretically parallels to the experimental CPL intensity for an electronic S_1 to S_0 transition. R can be expressed as shown below.[24]

Velocity form of the equation:[24]

$$R = \left\langle \Psi_{s_1} | \vec{\mu}_e | \psi_{s_0} \right\rangle \times \left(\frac{i}{2c}\right) \left\langle \Psi_{s_1} | \vec{m}_e | \psi_{s_0} \right\rangle \quad (9)$$

$$= \frac{\left\langle \Psi_{s_1} \left| e\vec{\nabla} \right| \psi_{s_0} \right\rangle}{E_{S_1} - E_{S_0}} \times \left(\frac{i}{2c}\right) \left\langle \Psi_{s_1} \left| -e\vec{r} \times \vec{\nabla} \right| \psi_{s_0} \right\rangle \quad (10)$$

Length form of the equation:[24]

$$R = \left\langle \Psi_{s_1} | \vec{\mu}_e | \psi_{s_0} \right\rangle \times \left(\frac{i}{2c}\right) \left\langle \Psi_{s_1} | \vec{m}_e | \psi_{s_0} \right\rangle \quad (11)$$

$$= \left\langle \Psi_{s_1} | -e\vec{r} | \psi_{s_0} \right\rangle \times \left(\frac{i}{2c}\right) \left\langle \Psi_{s_1} \left| -e\vec{r} \times \vec{\nabla} \right| \psi_{s_0} \right\rangle \quad (12)$$

For S_1 to S_0 transition: e = the elementary charge of an electron; $\vec{\mu}_e$ = electric dipole transition moment; $\vec{r}$ = position operator; c = the speed of light (c^{-1} is approximately equal to 1/137 atomic units (a.u.)); $\vec{m}_e$ = magnetic dipole transition moment; $\vec{\nabla}$ = curl operator. The calculated R-value is commonly reported in cgs units of 10^{-40} esu^2 cm^2.[24]

Using the length form of the equation, the g-factor becomes:[24]

$$g = \frac{4R}{D} = \frac{4\left\langle \Psi_{s_1} | \vec{\mu}_e | \psi_{s_0} \right\rangle \times \left\langle \Psi_{s_1} \left| \left(\frac{i}{2c}\right) \vec{m}_e \right| \psi_{s_0} \right\rangle}{D} \quad (13)$$

$$\frac{4\left\langle \Psi_{s_1} | -e\vec{r} | \psi_{s_0} \right\rangle \times \left\langle \Psi_{s_1} \left| \left(\frac{-ie}{2m_e \times c}\right) \vec{L}_n + g_e \vec{S}_n \right| \psi_{s_0} \right\rangle}{D} \quad (14)$$

where $g \sim 2$, the free electron g-factor; m_e is the mass of the electron; $\vec{S}$ is spin angular momentum; n represents the components of the Cartesian coordinate system; $\vec{L}$ is orbital angular momentum; D is dipole strength.[24]

Lanthanoids are mostly stable trivalent ions from cerium (Ce) to lutetium (Lu). Ln metals have a general electronic configuration as [Xe] $4f^n5d^{0-1}6s^2$ (n can range from 1 to 14). In the +3 oxidation state, these elements typically lose two 6s electrons and one 4f electron. The remaining electrons in the 4f subshell are relatively stable. In Ln contraction, the effective nuclear charge increases with atomic number. This contraction results in smaller ionic radii and leads to greater stabilization of the +3 oxidation state. The smaller ionic radii lead to

Open Access Article. Published on 02 April 2025. Downloaded on 4/4/2026 1:46:32 AM. This article is licensed under a Creative Commons Attribution-NonCommercial 3.0 Unported Licence.

stronger interactions with ligands. Two significant investigations show the beginning of the luminous lanthanide complexes between the 1930s and the early 1940s. Freed *et al.* demonstrated how the absorption lines band's intensity varied for Eu(III) in various solvents.[25] Weissman found that some of the Eu(III) complexes produce characteristic lanthanide emission when exposed to ultraviolet (UV) light.[26] The scientific community did not show significant interest in luminous lanthanide complexes until the early 1990s, after the efficient use of these materials in medical diagnostics.[27] Luk and Richardson originally identified CPL in Eu(III) and Tb(III) complexes containing chiral carboxylic acid in 1975.[28] After this finding, they also noted elevated CPL activity in an Eu(III) complex containing chiral 3-trifluoro acetyl camphorate ligands.[29] Following this, several studies have been conducted on CPL.[30,31] The prevalence of CPL measuring methods in the twenty-first century led to a steady rise in CPL reports. The chiroptical characteristics of $Cs[Eu((+)\text{-hfbc})_4]$ were reported by Lunkley *et al.* in 2011.[32] Recently, many reviews have mentioned chirality and Ln complexes.[2,17,33]

Chiral Ln(III) complexes comprise a luminous core and chiral organic ligands.[34] The 4f orbital in Ln is protected from its environment by the outer filled 5s and 5p orbitals.[34] Electronically, 4f–4f transitions yield strong emission lines, and the chiral ancillary ligands have significant CPL activity at these transitions.[35,36] Ln coordination with ligands involves outer 5d/6s orbitals in bond formation. The driving factor for Ln-ligand complexation might be electrostatic interactions with low covalency.[17] The Ln^{3+} nondirectional coordinating nature allows for flexible bonding with coordination numbers ranging from 3 to 12, with a preference for 8–9 coordination.[17,37] The steric and electronic properties of coordinated ligands *via* the chelating effect influence the stability of the lanthanide complexes.[17] The conventional hard-acid-soft-base theory classifies Ln^{3+} as a hard acid, while F, O and N are considered hard bases. The oxophilicity in oxygen stems from its hard-base character. Numerous electron-donating ligands with O, N, and F components have been designed to stabilize Ln^{3+} in highly coordinated surroundings.[17,32,38–41]

Ln ions are famous for their unique 4f to 4f emission, which extends over the visible and near infrared (NIR)-I, II regions.[17] The partial fulfillment of electrons in the 4f orbital results in "line-shaped" excitation and emission, independent of the coordinating ligands. Their 4f to 4f transitions are magnetic-dipole-allowed and electric-dipole-forbidden, making them ideal for reaching higher g_{lum} values.[9,17,42] Richardson classified the 4f to 4f transitions in various Ln^{3+} ions into three forms (DI, DII, and DIII) based on luminescence dissymmetry values.[17,43] The luminescence dissymmetry values decreased from DI to DII to DIII. The author discovered that type DI transitions only comprise the $^5D_0$ to $^7F_1$ transition of Eu^{3+}, whereas type DII transitions include the $^4G_{5/2}$ to $^6H_{5/2}$ transition of Sm^{3+} and the $^5D_4$ to $^7F_5$ transition of Tb^{3+}. The electric dipole-forbidden nature of 4f to 4f transitions allows for long-lasting Ln^{3+} emission. Due to their long-lasting emission, the Lanthanide complexes' emission may be separated from biological fluorescence and light scattering *in vivo*.[17] This makes them useful as biological probes and imaging agents.[17,44] Thus, the electronic features of chiral Ln complexes produce strong CPL signals with high dissymmetry, which are helpful in many optoelectronics and biomedical applications. Moreover, Ln complexes possess longer excited-state lifetimes than organic materials, allowing for sustained emission. This long-lived emission is valuable for applications such as time-resolved bioimaging. The CPL-active materials provide greater signal contrast in biomedical imaging. Hence, it helps monitor biological processes in real-time. Stachelek *et al.* designed a CPL laser scanning confocal microscopy system for the sub-cellular tracking of emissive chiral sub-cellular probes.[45] Their work demonstrated the feasibility of two-photon excitation in conjunction with CPL. They also developed a well-controlled inert CPL test target as a standard for enantioselective chiral-contrast imaging using enantiopure solutions of a Eu complex. They imaged both enantiomers of the chiral Eu complex within mouse skin fibroblast cells. Each enantiomer displayed a strong co-localization with common lysosomal and mitochondrial tracker dyes. Kunnen *et al.* explored the applicability of circularly and elliptically polarized light in the context of optical biopsy to achieve non-invasive diagnostic techniques for cancer detection in biological tissues.[46] They observed that the response of incident elliptically polarized states can be effectively measured. This was demonstrated by the phantom study using intralipid and microspheres water solutions. The mapping of the Stokes vector of backscattered light on a Poincaré sphere could reveal changes in the polarization state. These changes correlate with the concentration and size of scattering particles and preliminary tests show that the technique distinguishes between cancerous and non-cancerous tissues. The changes in nuclear size within cells could be characterized using this method. Thus, their work suggests that CPL light can be a promising tool for the non-invasive diagnosis of diseases.

Lanthanide complexes are good for CPL materials because of their large Stokes shift, low self-quenching, and resistance to photobleaching. However, they have low molar extinction coefficients, resulting in feeble emission.[17] Due to the low molar absorption coefficients of Ln(III) ions, the total brightness of Ln(III)-containing luminous compounds remains limited when samples are stimulated into the f–f transitions. The "antenna effect" can sensitize the Ln phosphors by transferring the absorbed energy to these metal ions. Weissman observed that light emission in Ln complexes with organic ligands may be initiated by stimulating the ligand electronic states.[26] Intramolecular energy transfer is then used to direct energy to the excited metal ions. Compounds or materials containing Ln are significantly affected by the antenna effect. The molar absorption coefficients of the surrounding ligands are largely responsible for determining the luminosity of the Ln phosphors.[35]

$4f^n$ configurations provide many electronic energy levels defined by three quantum numbers: total spin, total orbital, and total angular quantum number.[35] These levels are further divided by weak ligand field effects. G. H. Dieke provided the first summary of the $4f^n$ energy levels of all trivalent lanthanides doped in different crystals, covering UV, visible, and NIR spectral ranges (Fig. 4).[47] Eu(III) and Tb(III) are among the most

 This journal is © The Royal Society of Chemistry 2025

Open Access Article. Published on 02 April 2025. Downloaded on 4/4/2026 1:46:32 AM.
This article is licensed under a Creative Commons Attribution-NonCommercial 3.0 Unported Licence.

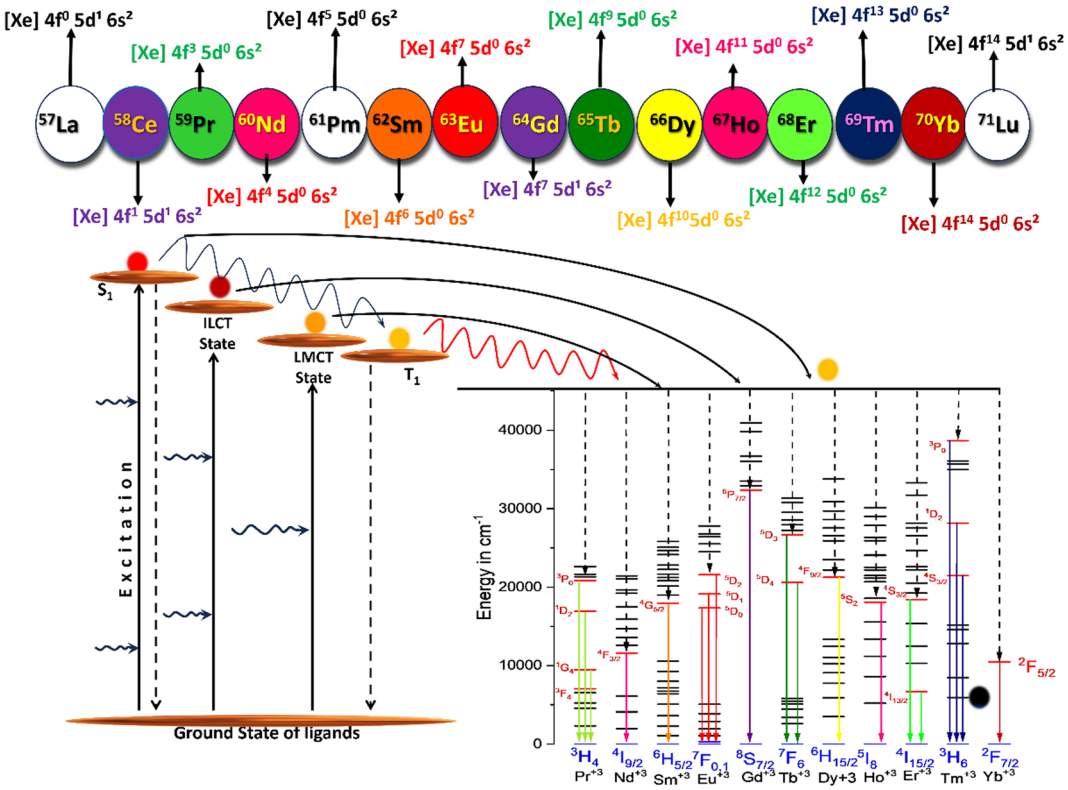

Fig. 4 Dieke diagram representing the various energy levels and energy transfer from antenna ligand energy levels to the Ln ions' energy levels (different energy levels of Ln ions have been depicted in the form of $^{2S+1}L_J$). The superscript is the spin multiplicity of the state, and the subscript is the total angular momentum quantum number. ILCT stands for intraligand charge transfer, LMCT stands for ligand to metal charge transfer, and S_1 and T_1 are the first excited singlet and triplet state, respectively (redrawn from ref. 17).

emissive lanthanide ions, with ground states ($^7F_0$ and $^7F_6$) and long-lived excited states ($^5D_0$ and $^5D_4$, respectively).[48] Eu(III) emits at 595 nm for the $^5D_0$ to $^7F_1$ transition. While Eu(III) and Tb(III) are the most often used lanthanides in luminescence applications, additional lanthanides have sparked interest despite their lower luminous qualities, including Dy(III), Sm(III), Yb(III), and Nd(III) in the near-IR.[48]

Lanthanide compounds have three optical transitions: allowed f–d, charge-transfer, and forbidden f–f transitions. The f–d transitions for free ions typically occur in the UV or visible spectral regions. As the 5d orbitals are expanded outermost, ligand-field splitting can push some of the Stark sublevels far into the visible region.[35] The localized and shielded nature of the f–f transitions causes their minimum environment interactions, resulting in narrow spectral lines. Meanwhile, the f–d transitions are broad due to the greater number of interactions of the 5d orbitals with the ligands.

The unique electronic configurations of Ln elements make the f–d transitions intense. Therefore, their energies can be fine-tuned across a wide range. This is why the Ln elements possess a good share in various optical applications. We have already mentioned that the f–f transitions are forbidden. Therefore, ligand-to-metal charge transfer (LMCT) transitions are important in sensitizing the luminescence in phosphors that contain lanthanides.[35] The transfer of energy from ligand to metal ion is important as it helps enhance the efficiency of the Ln phosphors. However, the LMCT transitions are typically observed in the electromagnetic spectrum's visible and ultraviolet (UV) ranges.[49] It is possible to modulate the LMCT by adjusting the nature of the antenna ligands. The ligand design plays a crucial role in deciding factors about its triplet energy levels; therefore, the luminescent properties of the material can be altered drastically. In contrast, metal-to-ligand charge transfer (MLCT) states are more commonly found in d–d-transition metal compounds due to their electronic structures. The MLCT transitions involve an electron transfer from a metal to a ligand. However, MLCT transitions are negligible in Ln, except Ce, because the energy required is generally too high.[35] Upon light excitation, the electron in the material jumps to a higher energy orbit. The Laporte parity selection rule says that the electric dipole transitions between energy levels of the same parity are forbidden.[35] Following this rule, the f–f transitions in Ln are prohibited under normal conditions, as the initial and final states have the same parity. Therefore, these f–f transitions are generally very weak. However, the symmetry of the electronic environment is disturbed when Ln ions are connected to the unsymmetrical ligands. This non-centrosymmetric environment causes the mixing of electronic states with different parities. Mixing the electronic states relaxes the strict selection rules, allowing the f–f transitions. The perturbation of the ligand field induces these transitions; therefore, these are known as induced dipole transitions.[35] Hence, the forbidden

Open Access Article. Published on 02 April 2025. Downloaded on 4/4/2026 1:46:32 AM.
This article is licensed under a Creative Commons Attribution-NonCommercial 3.0 Unported Licence.

f–f transitions are partially allowed following the relaxation of the selection rules. Lanthanide-based materials benefit from this relaxation of selection rules because it enhances their ability to absorb and emit light efficiently.

According to Laporte's forbidden f–f transitions, the Ln(III) ions naturally have weak absorption and emission intensities. However, an indirect method can lift these weak intensities. We can indirectly excite the Ln(III) ions by connecting chromophoric ligands to the metal ions. This method is known as the 'antenna effect,' which involves connecting a chromophoric group to the Ln(III) ion, which helps enhance its absorption and luminescence efficiency.[48] The indirect excitation method can optimize energy transfer processes in Ln(III)-based systems by choosing potential ligand moieties.[48] The antenna effect mentions the efficient energy transfer from organic ligands' excited states to lanthanide ions' excited states. The energy transfer mechanism from the organic ligand has been pictorially represented in Fig. 5 (above). The process involves energy absorption by the organic ligands, usually in the UV or visible regions. The absorption of the electromagnetic wave or light results in the excitation of the electron in the ligand. The excited electron reaches the longer-lived low-energy triplet state of the ligand *via* the intersystem crossing process. This triplet excited state transfers energy to the excited state energy level of the Ln ion non-radiatively. The resonance energy transfer from the ligand to the Ln ion requires a compatible energy gap between the ligand triplet state and the excited state of the Ln. The Ln ion receives energy and gets into the excited state, followed by a longer-lived Laporte forbidden transition to the ground state. Many factors drastically influence this energy transfer process,

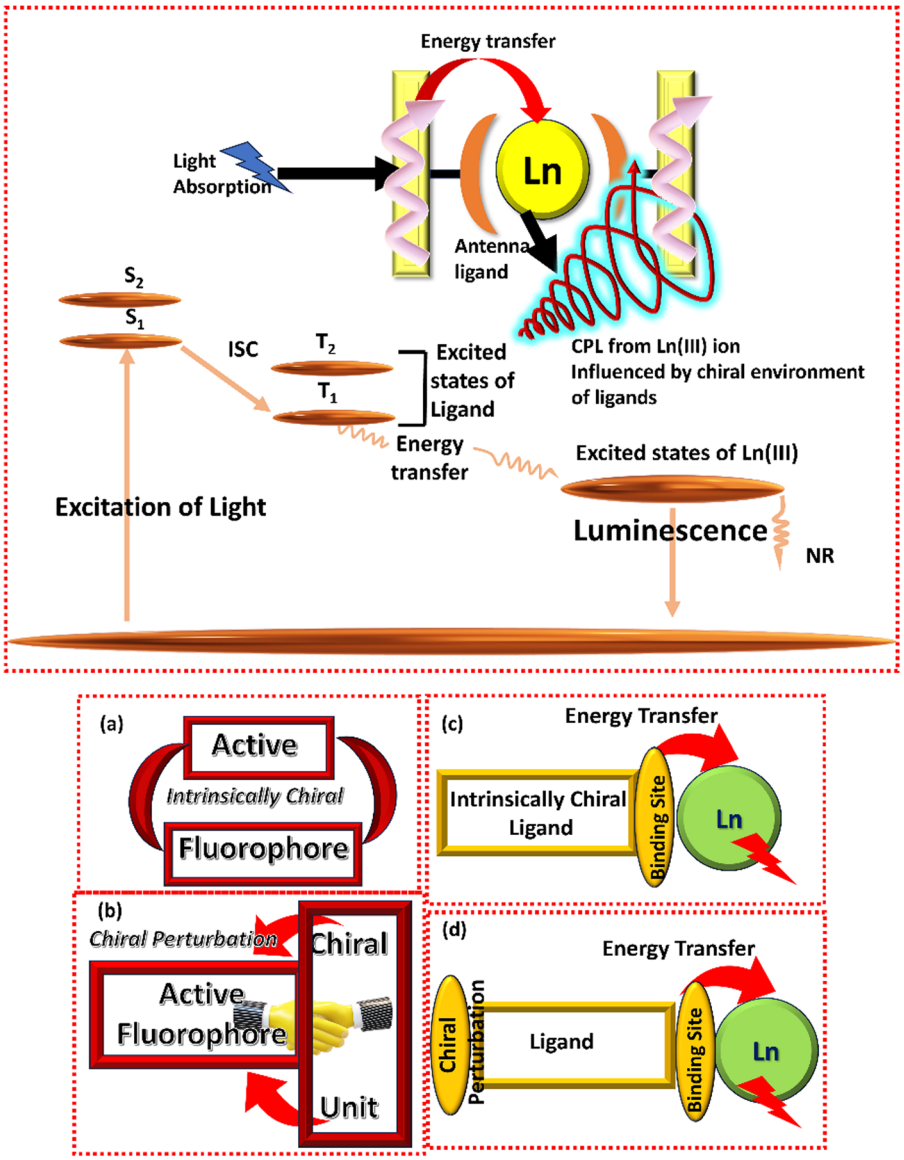

Fig. 5 (Above) Illustration of energy transfer from the antenna ligand to the lanthanide ion energy level.[48] (Below) Design strategies for developing intrinsically chiral (a) and perturbated chiral (b) thermally activated delayed fluorescence (TADF) fluorophores.[16] Proposed design strategies for developing (c) intrinsically chiral ligands and (d) perturbated chiral ligands for binding to Ln ions.

 This journal is © The Royal Society of Chemistry 2025

Open Access Article. Published on 02 April 2025. Downloaded on 4/4/2026 1:46:32 AM. This article is licensed under a Creative Commons Attribution-NonCommercial 3.0 Unported Licence.

like the distance between the ligand and the Ln ion, the energy gap between the ligand excited (triplet) state and the Ln ion excited state, and the binding ability of the ligand to the Ln ion.

Triplet states are important in the energy transfer between organic ligands and Ln(III) ions. The Ln ions can be sensitized when the lowest energy triplet state of the ligand is above the emitting Ln ion excited state.[35] These ligand triplet states may also quench the metal (Ln)-centered excited state when these are below it.[35] The function of singlet excited states in ligand-to-metal energy transfer is usually overlooked. The first reason for this is the effective interpretation of energy transfer in numerous Eu(III) and Tb(III) chelates using a singlet–triplet–Ln(III) route.[35] Second, the relatively short lifetimes of singlet states makes it difficult to demonstrate their role in the transfer process without rapid spectroscopic equipment.[35]

Energy transfer by the antenna effect involves excitation of the ligand followed by intramolecular energy transfer to the lanthanide ion. Energy is a scalar quantity and it lacks directional properties. Thus, the chirality cannot be directly transferred by scalar energy transfer. The asymmetry of the chiral ligand can cause circular polarization of the light emitted by the Ln complex. Forbes *et al.* observed that light can interact with chiral molecules during fluorescence and Förster resonance energy transfer (FRET) in many ways.[50] The most significant process is the absorption and emission of a single photon. They claimed that the chiral signal can be doubled when circularly polarized light is absorbed. There is no way the chirality can be transferred during the energy transfer process. They concluded that the physics of single photon absorption and emission always takes preference.

Two different design approaches are available in the literature for synthesizing chiral TADF or luminescent molecules.[16] The intrinsic chirality in the TADF molecule is the first method for developing chiral molecules (Fig. 5a, below). The axial, helical, planar, or central chirality can generate this intrinsic design approach in the molecule. The second method is referred to as the chiral perturbation strategy. The chiral and fluorescent/TADF units are connected in the chiral perturbation approach (Fig. 5b, below). Together, these two components provide a whole set of chiral luminous molecules. These two methods are well-known for designing and developing chiral TADF molecules. Developing the chiral ligands for the Ln complexes is also possible following these two approaches. The two approaches have been depicted pictorially in Fig. 5c and d (below).

Looking at the benefits of the CPL in our daily lives and the enthusiasm of the research community in this field, we have included different chiral Ln complexes in this mini-review article. We have already mentioned the advantage of antenna ligands in transferring the energy to the Ln ions and efficiently enhancing its luminescence despite the involvement of electric dipole forbidden 4f–4f transitions. We have categorized this article based on the different binding ligands to the Ln metal ions. The binding ligands include β-ketonate-based ligands, cyclen-based ligands, pyridine dicarboxylate-based ligands, multiple oxygen atoms-based ligands, and multiple nitrogen atom-based ligands. In this review, we briefly explain the characteristics of the chiral Ln complexes based on these ancillary ligands and conclude with the rational ligand design and advantages of these complexes.

2. Various types of ligand-based Ln complexes

2.1. β-Diketonate-based ligands and chiral Ln complexes

Because of the lipophilicity of Ln^{3+}, β-diketones are considered to be among the most successful coordinating ligands. Cui *et al.* (2021) synthesized and structurally characterized two homochiral Sm(III) and Eu(III) tris(β-diketonate) enantiomers.[51] These complexes of Eu and Sm were supported by (*R* or *S*) *N*,*N*′-donor and fluorinated β-diketone ligands (Scheme 1, left). They exhibited intense emissions with long lifetimes and high photoluminescence quantum yield (PLQY) in solid-state and in solution. This was due to the proper match of energy levels between the triplet energy state of Hbtfa ligand and the energy levels of the Eu(III) ($^5D_0$) and Sm(III) ($^4G_{5/2}$) ions, respectively. Specifically, the addition of a chiral *N*,*N*′-donor ligand caused the deformed non-centrosymmetric structures in the Sm(III) and Eu(III) tris(β-diketonate) precursors. Consequently, the homochiral Eu(III) and Sm(III) tris(β-diketonate) enantiomeric pairs exhibited better optical properties compared to the majority of their centrosymmetric counterparts. They observed that in the solid state and DCM solvent, *R*-2-Sm/*S*-2-Sm and *R*-1-Eu/*S*-1-Eu displayed strong, distinctive emissions of Eu(III) (red) and Sm(III) (orange-red) ions with extended lifetimes and high PLQY. The CD and UV-vis absorption spectra of the homochiral *R*-1-Eu and *S*-1-Eu pairs have been depicted in Scheme 1a and b (right). The g_{lum} values for *R*-1-Eu/*S*-1-Eu were obtained up to $+2.56 \times 10^{-3}/-2.90 \times 10^{-3}$ (Table 1). They used the Raman optical activity (ROA) technique to measure the CPL. In *R*-1-Eu, the total PLQY could reach up to 61% and 53% in the solid and solution states (DCM), respectively. The rare Sm(III) tris(β-diketonate) complexes, *R*-2-Sm, could reach up to 6.5% (solid-state) and 3.1% (DCM). The *R*-2-Sm and *R*-1-Eu exhibited a significant triboluminescence phenomenon that was apparent to the unaided eye.

The same group used the chiral N^N-donor ligand (Scheme 2, left) to bind with Pr and Ho and synthesized two chiral mononuclear Ln(III) complexes [Ln(dbm)$_3$(L)] [Ln = Ho (2) and Pr (1)].[58] When exposed to visible light (410 nm), 1 and 2 exhibited typical NIR emissions of Pr(III) and Ho(III) ions. The CD spectra of complexes 1 and 2 were depicted in Scheme 2a and b (right). The study on their nonlinear optical responses revealed that 1 and 2 concurrently displayed significant third and second-harmonic generation responses brought on by their non-centrosymmetric molecular architectures.

Based on X-ray crystallographic investigations, the CPL of chiral Eu(III) complexes with nona- and octa-coordinated Eu structures, 1-*R*,/1-*S*, 2-*SS*, and 3 (Scheme 3) has been described, and their structural characteristics were addressed by Harada *et al.* in 2012.[52] It was anticipated that inserted Pybox ligands will enclose the Eu(III) core from surrounding solvents and

Open Access Article. Published on 02 April 2025. Downloaded on 4/4/2026 1:46:32 AM.
This article is licensed under a Creative Commons Attribution-NonCommercial 3.0 Unported Licence.

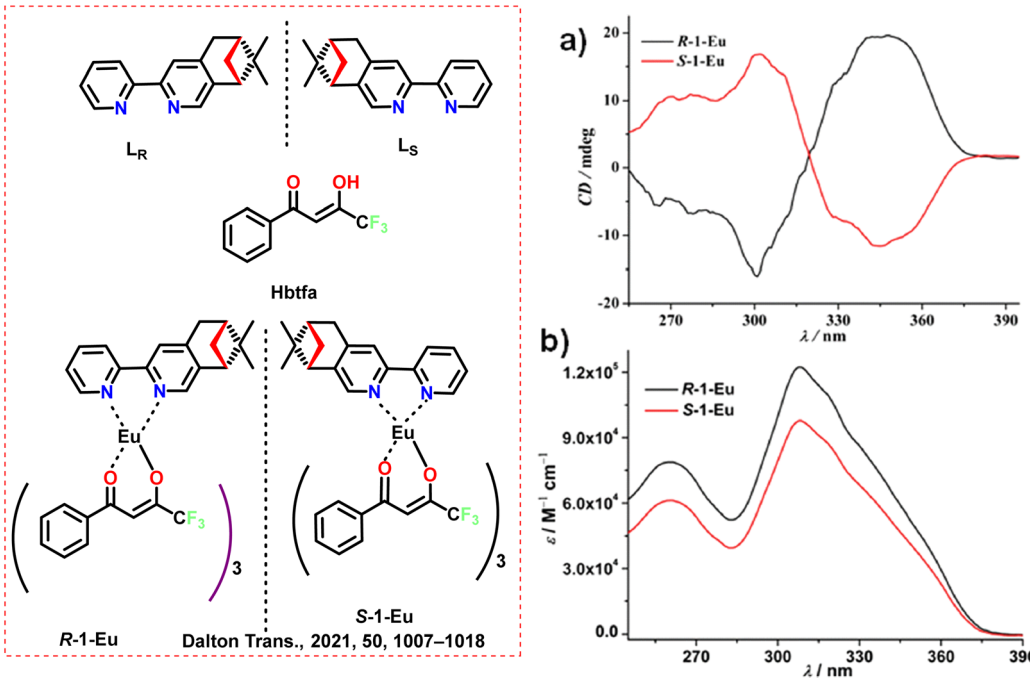

Scheme 1 (Left) Chemical structures of the ligands and Ln complexes (*R*-1-Eu and *S*-1-Eu).[51] (Right) (a) Electronic circular dichroism (ECD) spectra and (b) UV-vis absorption spectra of homochiral *R*-1-Eu and *S*-1-Eu enantiomeric pairs in DCM (1×10^{-5} M). Reproduced from ref. 51 with permission from the Royal Society of Chemistry, copyright [2021].[51]

would inhibit the excited state's vibrational decay. They also anticipated the particular stereoselective interactions between Pybox and D-facam, which were two different kinds of ligands. The interactions between ligands were anticipated to inhibit pseudo-racemization and promote enhanced chiroptical purity in complexes. The Pybox ligands were added as a chiral tridentate ligand to [Eu(D-facam)$_3$]. These chiral Eu(III) complexes with their $^5D_0$ to $^7F_1$ (magnetic-dipole) and $^5D_0$ to $^7F_2$ (electric-dipole) transitions demonstrated comparatively strong photoluminescence. The dissymmetry factor of CPL of complex 3 at the $^5D_0$ to $^7F_1$ transition was relatively moderate (g_{CPL} = −0.46). However, the dissymmetry factors of CPL in the $^5D_0$ to $^7F_1$ band of 1-*R* and 1-*S* were −1.0 and −0.8, respectively (Table 1). The CPL spectra were detected at room temperature with JASCO FP-6500 spectrometers. X-ray crystallographic data in these compounds showed ligand-to-ligand hydrogen bonding, which was predicted to maintain their chiral geometries even in the solution phase.

Based on the twisting motion of a ligand, BIPYPO exhibits sign reversal of CPL signal in a *cis–trans* isomerization of chiral Eu(III) complexes (Scheme 4).[59] The work of Kawai's group in 2014 shows that the twisting motion of BIPYPO produces the *s-cis* and *s-trans* geometries of a chiral Eu(III) complex containing either D-1 or D-2 ligands (Scheme 4). The chelate between

Table 1 Photophysical properties of β-diketonate-based chiral Ln complexes

Ln complex	Transition	Wavelength (nm)	Dissymmetry factor (g_{lum})	PLQY (%)	Ref.
R-1-Eu	$^5D_0$ to $^7F_1$	602	$+2.56 \times 10^{-3}$	61 (solid state)	*Dalton Trans.*, 2021, **50**, 1007–1018[51]
S-1-Eu	$^5D_0$ to $^7F_1$	602	-2.90×10^{-3}	—	*Dalton Trans.*, 2021, **50**, 1007–1018[51]
1-*R*	$^5D_0$ to $^7F_1$	594	−1.0 (acetone-d_6)	0.89 ± 0.09 (acetone-d_6)	*Inorg. Chem.*, 2012, **51**, 6476–6485[52]
1-*S*	$^5D_0$ to $^7F_1$	594	−0.8 (acetone-d_6)	0.89 ± 0.10 (acetone-d_6)	*Inorg. Chem.*, 2012, **51**, 6476–6485[52]
2-*SS*	$^5D_0$ to $^7F_1$	594	−1.0 (acetone-d_6)	0.50 ± 0.15 (acetone-d_6)	*Inorg. Chem.*, 2012, **51**, 6476–6485[52]
3	$^5D_0$ to $^7F_1$	594	−0.46 (acetone-d_6)	0.54 ± 0.17 (acetone-d_6)	*Inorg. Chem.*, 2012, **51**, 6476–6485[52]
Na[Eu((+)-hfbc)$_4$]	$^5D_0$ to $^7F_1$	591	+0.08 ($CHCl_3$)	—	*Inorg. Chem.*, 2011, **50**, 12724–12732[32]
K[Eu((+)-hfbc)$_4$]	$^5D_0$ to $^7F_1$	591	+0.14 ($CHCl_3$)	—	*Inorg. Chem.*, 2011, **50**, 12724–12732[32]
Rb[Eu((+)-hfbc)$_4$]	$^5D_0$ to $^7F_1$	585	+0.47 ($CHCl_3$)	—	*Inorg. Chem.*, 2011, **50**, 12724–12732[32]
Cs[Eu((+)-hfbc)$_4$]	$^5D_0$ to $^7F_1$	585	+0.55 ($CHCl_3$)	—	*Inorg. Chem.*, 2011, **50**, 12724–12732[32]
CsYb((+)-hfbc)$_4$	—	985	−0.38 (CH_2Cl_2)	—	*Dalton Trans.*, 2022, **51**, 518–523[53]
(CsYb((−)-hfbc)$_4$)	—	985	+0.31 (CH_2Cl_2)	—	*Dalton Trans.*, 2022, **51**, 518–523[53]
CsEu((+)-hfbc)$_4$	$^5D_0$ to $^7F_1$	595	+1.41 ($CHCl_3$)	—	*Adv. Mater.*, 2015, **27**, 1791–1795[54]
CsEu((−)-hfbc)$_4$	$^5D_0$ to $^7F_1$	595	−1.41 ($CHCl_3$)	—	*Adv. Mater.*, 2015, **27**, 1791–1795[54]
CsEu((−)-hfbc)$_4$	$^5D_0$ to $^7F_1$	595	−1.35 ± 0.10 (in PMMA)	—	*Adv. Funct. Mater.*, 2017, **27**, 1603719[55]
Cs[Eu((*S*)-hfbcv)$_4$]	$^5D_0$ to $^7F_1$	594	0.82 (solid state, thin film)	—	*Chem. Commun.*, 2015, **51**, 11903–11906[56]
D-1	$^2F_{5/2}$ to $^2F_{7/2}$	985	0.072 (solid state)	—	*Dalton Trans.*, 2023, **52**, 17758–17766[57]
D-2	$^2F_{5/2}$ to $^2F_{7/2}$	982	0.045 (solid state)	—	*Dalton Trans.*, 2023, **52**, 17758–17766[57]

This journal is © The Royal Society of Chemistry 2025

Open Access Article. Published on 02 April 2025. Downloaded on 4/4/2026 1:46:32 AM.
This article is licensed under a Creative Commons Attribution-NonCommercial 3.0 Unported Licence.

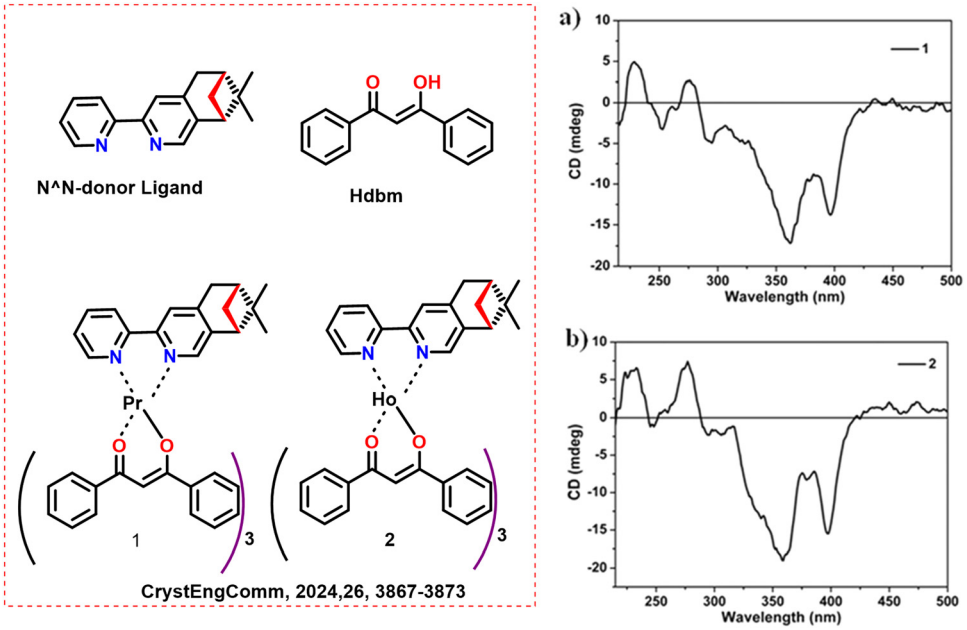

Scheme 2 (Left) Chemical structures of the ligands and Ln complexes (1 and 2);[58] (right) solid state electronic circular dichroism (ECD) spectra of (a) 1 and (b) 2. Reproduced from ref. 58 with permission from the Royal Society of Chemistry, copyright [2024].[58]

the phosphoryl oxygen and the Eu(III) ion forces the *s-cis* geometry of BIPYPO, resulting in eight coordination around the Eu(III) ion in the *s-cis* Eu(III) complexes. The phosphorus-nitrogen interaction induces a quasi-seven-coordinate Eu(III) complex, which provides a conformational lock on the *s-trans* geometry of the BIPYPO ligand. The sign of the CPL signals between the *s-cis* and *s-trans* isomers changes due to the variation in coordination geometry. For the $^5D_0$ to $^7F_1$ transition, the *s-cis* and *s-trans* isomers of Eu(III) complexes show positive and negative CPL signals, respectively. When the solvent is changed from acetonitrile-d_3 to acetone-d_6, the ratio of *s-trans*-D-1 to *s-cis*-D-1 rises, which causes a shift in the sign of the CPL signals. The luminescence dissymmetry factor value of D-2 for the $^5D_0$ to $^7F_1$ (g_{MD}) transition continuously changes from the positive value of g_{MD} = 0.66 to the negative value of g_{MD} = −0.17 with an increasing acetone-d_6 ratio. The lifetime studies depicted a bi-exponential decay, suggesting the two emitting species (*s-cis* and *s-trans* isomers). They irradiated the sample with a 375 nm excitation laser in the CPL measuring system. A 50 kHz modulated photo-elastic modulator (Hinds, PEM-90) was used to adjust the retardation of the emitted light. They calibrated their EI-CPL instrument using a reference to data acquired from a CPL spectrometer (JASCO, CPL-200).

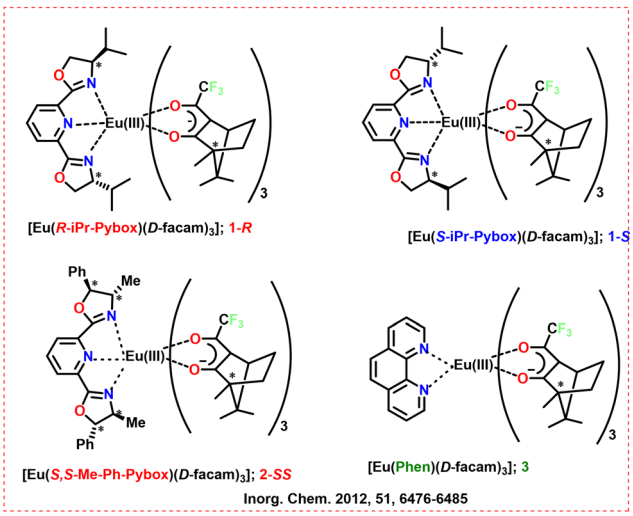

Scheme 3 Chemical structures of the ligands and Ln complexes (1-*R*, 1-*S*, 2-*SS*, and 3).[52]

Lunkley *et al.* (2011) studied the chiroptical spectra of Eu complexes in different solvents.[32] When the chiral systems have well-defined symmetries and strong CPL activity, it may be possible to create a "helicity rule" that determines helicity configuration (clockwise and anti-clockwise) based on CPL sign patterns. The precise chiral configuration in solution was revealed by analyzing the luminosity and CPL of Cs[Sm((+)-hfbc)$_4$] in chloroform and of M^I[Eu((+)-hfbc)$_4$] complexes (M^I = K, Na, Rb, and Cs, Scheme 5) in chloroform, acetonitrile, and ethanol. When the alkali metal ions and solvents were changed, the CPL and PL spectra of M^I[Eu((+)-hfbc)$_4$] exhibited behavior that was comparable to the exciton CD in the intraligand π–π* transitions. They measured the CPL using a custom-built spectrometer. Table 1 depicts the measured g_{lum} values of the complexes.

Bari's group investigated chiroptical characteristics such as CD and CPL in the near-infrared range of two sets of Yb, Tm, and Er complexes in 2022.[53] The two complexes were a tetrakis, *C*4 symmetric CsLn(hfbc)$_4$ (Ln = Yb, Tm, Er) and a *D*3 symmetric [TMG-H$^+$]$_3$Ln (BINOLate)$_3$ (Ln = Yb, Tm, Er) (Scheme 6, above). They used three distinct energy ranges for measuring the chiroptical activity of Yb (900–1040 nm), Tm (1180–1240 nm), and Er (1430–1600 nm). There are decent chiroptical characteristics in emission and absorption for the ytterbium set

Open Access Article. Published on 02 April 2025. Downloaded on 4/4/2026 1:46:32 AM. This article is licensed under a Creative Commons Attribution-NonCommercial 3.0 Unported Licence.

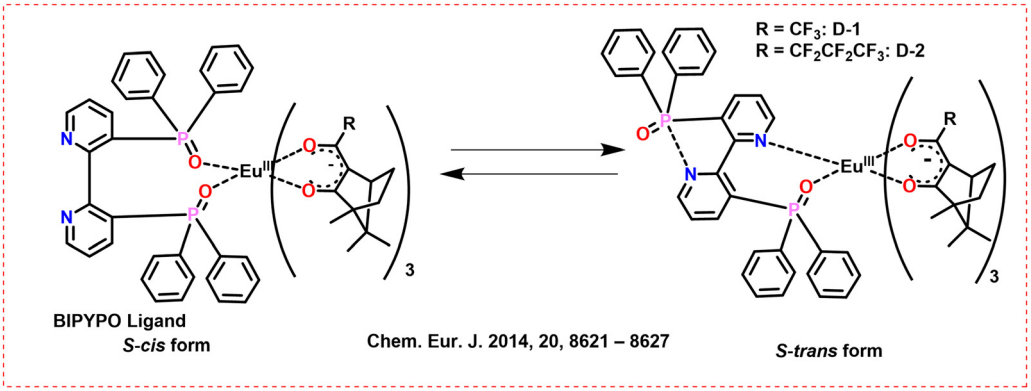

Scheme 4 Chemical structures of the ligands and Ln complexes (D-1 and D-2).[59]

of complexes, which results from Stark splitting of the $^2F_{7/2}$ to $^2F_{5/2}$ manifold. Outstanding g_{abs} values were also displayed by these complexes, reaching as high as |1.70| for $(CsEr(hfbc)_4)$ and |0.40| for the $([TMG\text{-}H^+]_3Er(BINOLate)_3)$ complex. The CD and CPL spectra of some complexes have been depicted in Scheme 6 (below). NIR-CPL spectra were recorded using a home-built spectrofluoropolarimeter, with a Hamamatsu R316 Ag–O–Cs photomultiplier tube. Table 1 depicts the measured g_{lum} values of the complexes.

The same group reported a new method for producing OLEDs with up to 70% of CPEL (CP red emission) in 2015.[54] The important elements determining g_{EL} value in CP-OLEDs were explored using a chiral lanthanide complex as the guest emitter. The chiral emitter selected for this prototype device was the Ln(III) complex, $CsEu(hfbc)_4$ (Scheme 7), which has the greatest CPPL (g_{PL} = 1.38 at 595 nm). The emissive layer consisted a blend of chiral Ln complex along with polyvinylcarbazole host and 1,3-bis[2-(4-*tert*-butylphenyl)-1,3,4-oxadiazo-5-yl]benzene additive. Despite having a low PLQY (3% as powder), this emitter offers an excellent trade-off between total luminescence and polarization. For Eu $^5D_0$ to $^7F_1$ at 595 nm, a g_{EL} value of +0.73/−0.79 is observed for the devices with the thinnest cathode. Similarly, they could observe a g_{EL} value of −0.09/+ 0.15 for the Eu $^5D_0$ to $^7F_2$ band at 612 nm. For Eu $^5D_0$ to $^7F_1$, at 595 nm, a g_{PL} value of +1.41/−1.41 (in $CHCl_3$) was observed for the emitters (Table 1). A custom-built system was used for the CPL measurement.

Similarly, they further demonstrate that appropriate active layer formulation and device architecture fine-tuning enhances the performance of chiral europium complex-based CP-OLEDs $(CsEu(-)\text{-}hfbc)_4$ in 2017 (Scheme 8).[55] The g_{PL} values of the emitter in poly(methyl methacrylate) (PMMA) reaches −1.35 ± 0.10 (595 nm, Table 1) in a custom-built CPL measurement system. Polarization capabilities of $g_{EL} = -1$ are achieved with an appropriate device design. The CP-OLEDs show remarkable polarization of emitted photons at 595 nm (about 65–75%) using polymer interlayers. The CP-OLED improved the EQE to 0.05% using a semi-transparent cathode, which was ten times greater than the control device. The fabricated devices attain g_{EL} values of −0.88 ± 0.14 (595 nm) and 0.14 ± 0.09 (612 nm) at 6 V.

In 2012, Bari's group used a bimetal complex $(MLn(hfbc)_4)$ (Scheme 9) prepared by Kaizaki *et al.* and provided a thorough structural study in solution as well as potential dynamic processes with the help of NMR.[60] They could attain a precise geometry for the $CsEu(hfbc)_4$ solution. The void of perfluorinated chains perfectly accommodate the Cs^+ ion. This creates a rigid structure with a small biting angle above the lanthanide ion. This small angle prevents axial binding. It provides strong binding interactions that inhibit dynamic rearrangement. This factor could also help avoid the quenching of Eu-luminescence commonly seen in hydrated complexes.

Similarly, they developed an Eu-based chiral complex (*R*/*S*-$Cs[Eu(hfbcv)_4]$) (Scheme 10) that exhibits high CPL in the solid state and near-UV excitation in 2015.[56] Eu has a high tendency to be bound by diketonate ligand that was based on carvone. In the solid state, the Eu complex exhibits high red CPL with a g_{lum} value of 0.82 at 594 nm (deposition of a few drops of the CH_3CN solution followed by slow solvent evaporation) (Table 1). The CPL spectra measured using a home-made spectrometer with a PEM are depicted in Scheme 10 (right) along with the *g* values. The main focus of this work was to prevent unwanted (far)-UV irradiation by pushing the excitation wavelength toward visible light and high CPL. The developed complex could achieve both targets. In light of

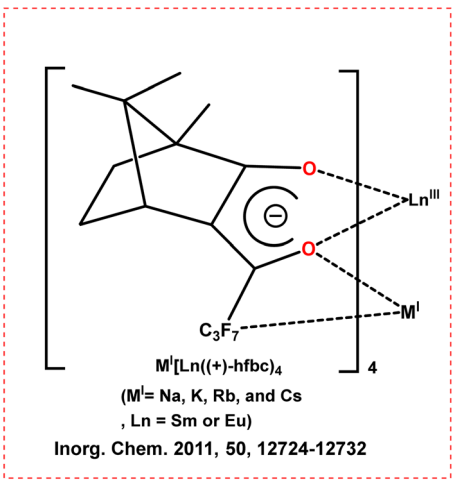

Scheme 5 Chemical structures of the ligands and Ln complexes $(M^I[Ln((+)\text{-}hfbc)_4])$.[32]

 This journal is © The Royal Society of Chemistry 2025

Open Access Article. Published on 02 April 2025. Downloaded on 4/4/2026 1:46:32 AM.
This article is licensed under a Creative Commons Attribution-NonCommercial 3.0 Unported Licence.

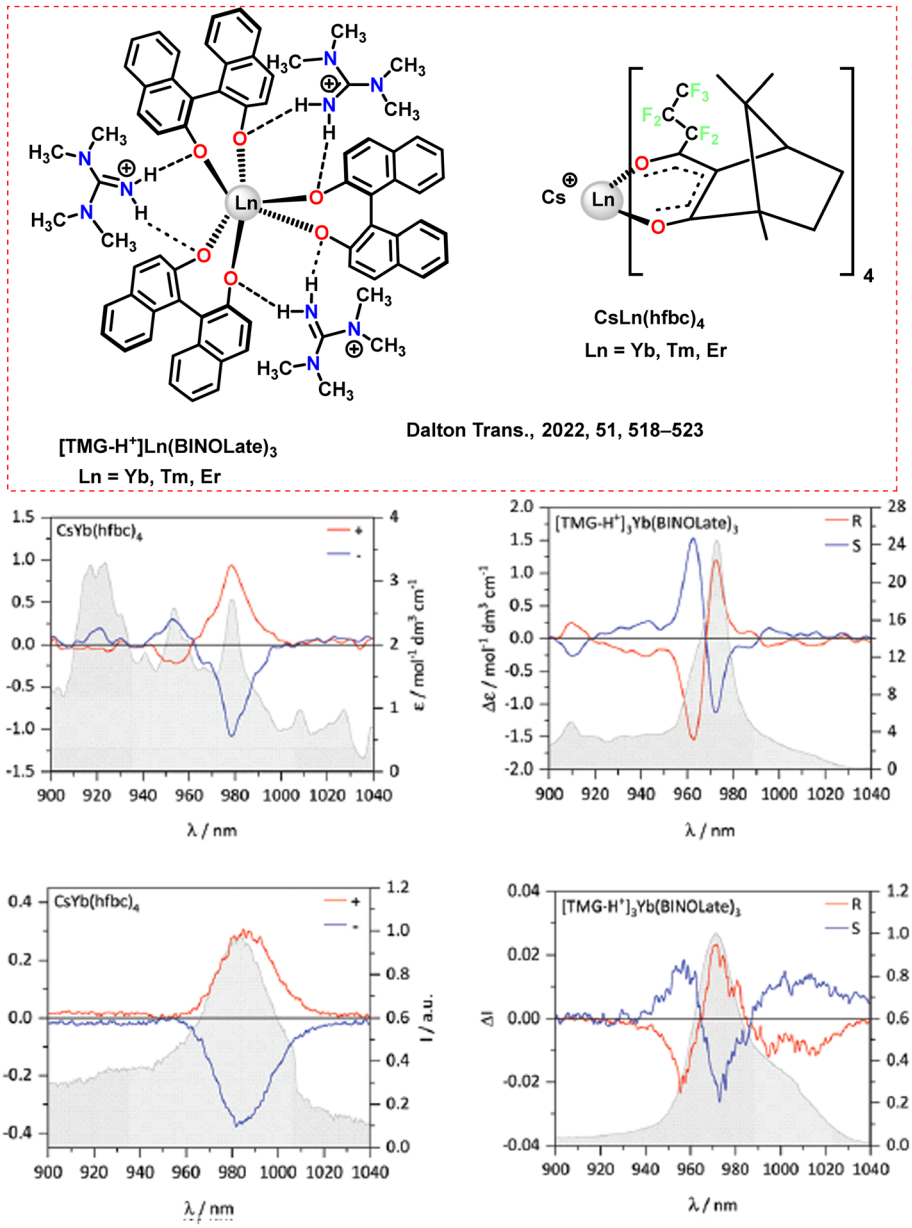

Scheme 6 (Above) Chemical structures of the ligands and Ln complexes.[53] (Below) Top: NIR-CD spectra of $CsYb(hfbc)_4$ (4 mM) and $[TMG\text{-}H^+]_3Yb(BINOLate)_3$ (8 mM) with average total absorption traced in the background. Bottom: NIR-CPL spectra of $CsYb(hfbc)_4$ (1 mM) and $[TMG\text{-}H^+]_3Yb(BINOLate)_3$ (1 mM) with normalised average total emission traced in the background spectra recorded in CH_2Cl_2 at room temperature. λ_{exc} = 365 nm, Reproduced from ref. 53 with permission from the Royal Society of Chemistry, copyright [2022].[53]

this, carvone, a chiral ketone was chosen and the diketone was produced by a Claisen reaction using ethyl perfluorobutyrate.

Du *et al.* (2023) developed two sets of chiral Yb(III) enantiomers, D-1/L-1 and D-2/L-2, by inserting enantiomerically pure mono-bidentate *N*-donor ligands (L_R/L_S) into $Yb(btfa)_3(H_2O)_2$ and $Yb(dbm)_3(H_2O)$, respectively (Scheme 11, above).[57] The Yb(III) ions in the mononuclear structures of D-1/L-1 were eight-coordinated. The D-2/L-2 displayed cocrystal structures with two Yb(III) ions that were eight ($Yb(dbm)_3(L_R/L_S)$) and seven ($Yb(dbm)_3(C_2H_5OH)$) coordinated. They exhibit diverse linear and nonlinear optical properties and various chemical architectures. Compared to chiral cocrystal D-2, chiral mononuclear D-1 exhibits superior NIR-PL and CPL. NIR-CPL spectra of D-1/L-1 and D-2/L-2 with total NIR emission profiles are depicted in Scheme 11 (below) (g_{lum} in Table 1). CPL was recorded on an Olis NIRCPL SOLO instrument.

2.2. Cyclen based ligands and chiral Ln complexes

The most often used ligands to stabilize Ln^{3+} are derivatives of the macrocyclic skeleton cyclen ring.[17] The macrocyclic rings in cyclen structures have a quadrangular conformation. By bridging N with various functional groups, chirality may be imported into the inner part of the macrocyclic ring.[17] Through macroring-sidearm cooperativity, the macrocyclic rings and

Open Access Article. Published on 02 April 2025. Downloaded on 4/4/2026 1:46:32 AM.
This article is licensed under a Creative Commons Attribution-NonCommercial 3.0 Unported Licence.

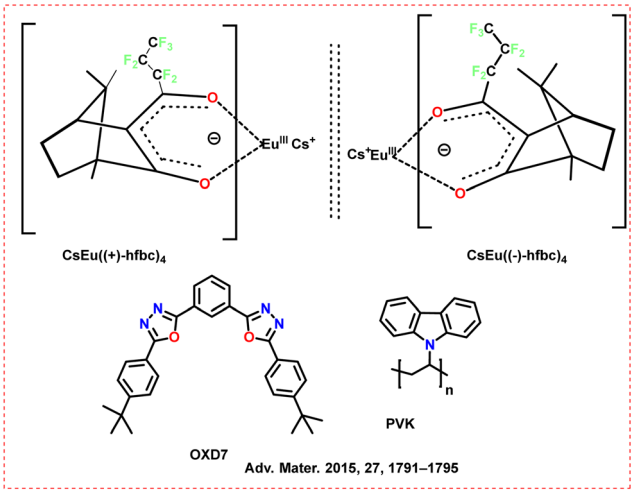

Scheme 7 Chemical structures of the ligands and Ln complexes $CsEu(hfbc)_4$.[54] OXD7 = 1,3-bis[2-(4-*tert*-butylphenyl)-1,3,4-oxadiazo-5-yl]benzene; PVK = polyvinylcarbazole.

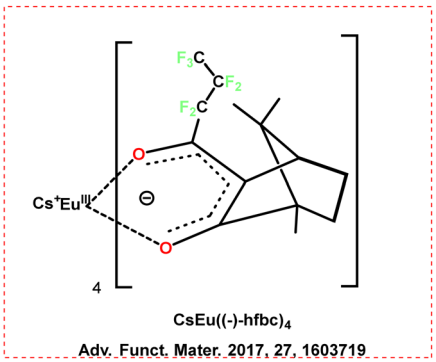

Scheme 8 Chemical structures of the ligands and Ln complexes $CsEu((-)\text{-}hfbc)_4$.[55]

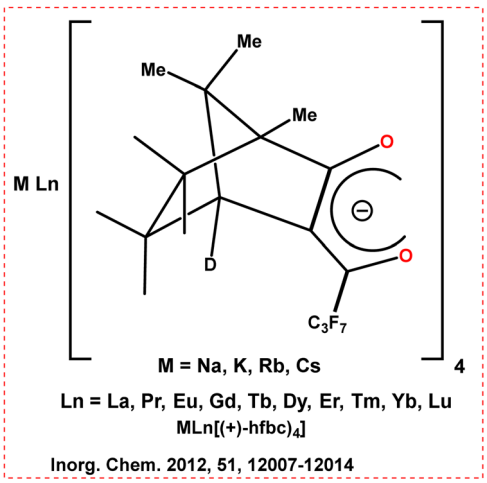

Scheme 9 Chemical structures of the ligands and Ln complexes $(MLn(hfbc)_4)$.[60]

connected coordinating sidearms are prone to bonding with lanthanide ions. Walton *et al.* (2011) developed an isostructural series of lanthanide complexes of a pyridylphenylphosphinate ligand, L^3 (Scheme 12, left).[61] The molecular core of the ligand was based on triazacyclononane. The *C*3-symmetric clockwise and anti-clockwise complexes of Eu and Tb are strongly emissive. They developed a phosphinate-based L3 ligand, which results in *C*3-symmetry chiral Ln complexes. The phosphorus substituents tend to be orientated away from the 9-N_3 ring in the phosphinate-based ligand complex (LnL^3, Ln = Eu and Tb). Due to the formation of steric bulk across from the macrocyclic ring, the bound Ln(III) ion is protected from the solvent environment. Nine ligand donors coordinate the lanthanide ion, including the N atoms of the 1,4,7-triazacyclononane ring, the N atoms of the pyridyl moiety and oxygen of the phosphinate. A pseudo-*C*3 axis passes through the center of the macrocyclic ring in the deformed tricapped trigonal prism that surrounds the Ln(III) ion. The Eu and Tb complexes are highly emissive in aqueous solution, with overall PLQY of 0.11 and 0.50, respectively. The CPL spectra of the resolved complexes show mirror-image forms with an emission dissymmetry factor (Table 2) of up to 0.4 (Scheme 12, right).

The same group observed that the helicity of the (*SSS*)-Δ enantiomer was inverted upon binding of a Tb(III) and Eu(III) complex to serum albumin's "drug site II" in 2008 (Scheme 13, left).[70] The Δ-(*SSS*)-Eu, Gd, and Tb complexes of ligand L^1 selectively bound to serum albumin. A change in its CPL indicated the inversion in helicity. They measured the CP emission spectra of $\Delta\text{-}[Tb{\cdot}L^1]^{3+}$ and $\Lambda\text{-}[Tb{\cdot}L^2]^{3+}$ with or without additional BSA. No emission polarization or spectrum shape change is seen with the Λ isomer between 0.03–0.3 mM BSA. In contrast, the Δ-isomer causes a 35% drop in intensity and an inversion of the emission sign. This is particularly noticeable in the magnetic dipole-allowed $^5D_4$–$^7F_5$ transitions at 545 nm (Scheme 13, right). For the Δ-isomer, this behavior aligns with an inversion of the complex's helicity in its protein-bound state. Their helicity was reversed to maximize binding, and their structure was controlled during this procedure. This process is quick and reversible. This behavior is not seen with (*R*)-Λ complexes, which defines a distinct chiroptical probe of albumin binding.

Similarly, they observed that serum albumin increases the emission intensity of a monocationic Tb or Eu(III) complex of a bis(1-azaxanthone) ligand in 2010 (Scheme 14, left).[71] The Ln complex stains the dividing cells, making mitotic chromosomes visible. HeLa cells were used in cell uptake studies to investigate the complexes $[TbL^2]^+$ and $[TbL^1]^+$, and cellular staining was seen using luminescence microscopy. The staining pattern (at high concentrations of the added complex in the medium) aligns with an endosomal/lysosomal distribution. Less than 10% of the cells are stained at lower complex addition concentrations. The staining pattern and the nuclear localization profile's characteristics align with the idea that cells going through the "M" phase of division are being specifically labelled (Scheme 14, right).

Dai *et al.* outlined a productive method for creating water-soluble chiral DOTA complexes with a very high ratio of twisted

This journal is © The Royal Society of Chemistry 2025

Open Access Article. Published on 02 April 2025. Downloaded on 4/4/2026 1:46:32 AM.
This article is licensed under a Creative Commons Attribution-NonCommercial 3.0 Unported Licence.

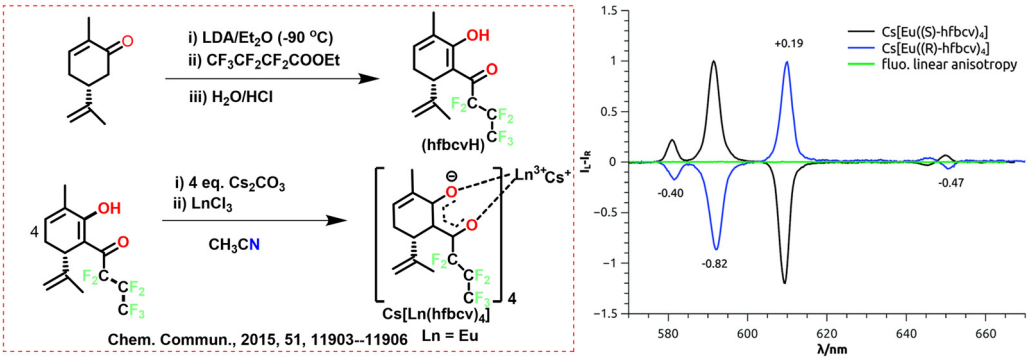

Scheme 10 (Left) Chemical structures of the ligands and Ln complexes (*R*/*S*-Cs[Eu(hfbcv)$_4$]).[56] (Right) CPL spectra of Cs[Eu((*S*)-hfbcv)$_4$] (black) and Cs[Eu((*R*)-hfbcv)$_4$] (blue) on a quartz plate upon irradiation at 370 nm, with calculated g_{lum} values and fluorescence linear anisotropies (green). Reproduced from ref. 56 with permission from the Royal Society of Chemistry, copyright [2015].[56]

square antiprismatic (TSAP) coordination geometry in 2019 (Scheme 15).[62] $[LnL4]^{5-}$ Complexes form with up to 93% of the TSAP isomer and exhibit excellent water solubility. With its strong relaxivity, $[GdL4]^{5-}$ is a promising and effective MRI contrast agent. High g_{lum} values are observed in buffer solutions: 0.285 ($\Delta J = 1$) for $[TbL3]^{-}$ and 0.241 ($\Delta J = 1$) for $[TbL4]^{5-}$ (Table 2). CPL spectra were measured using a custom-built spectrometer.

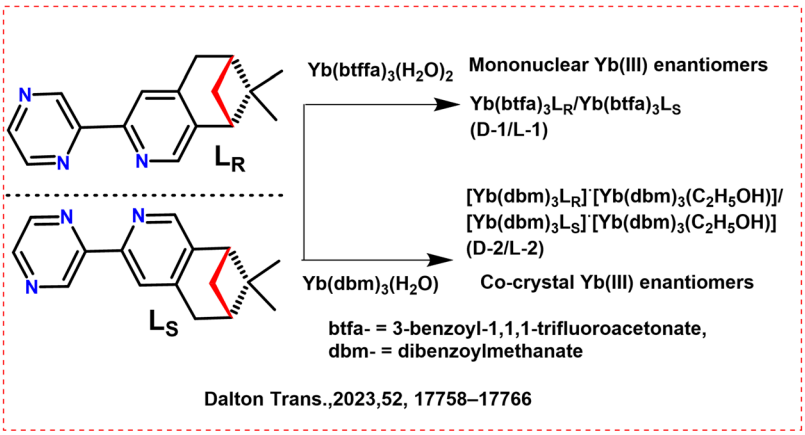

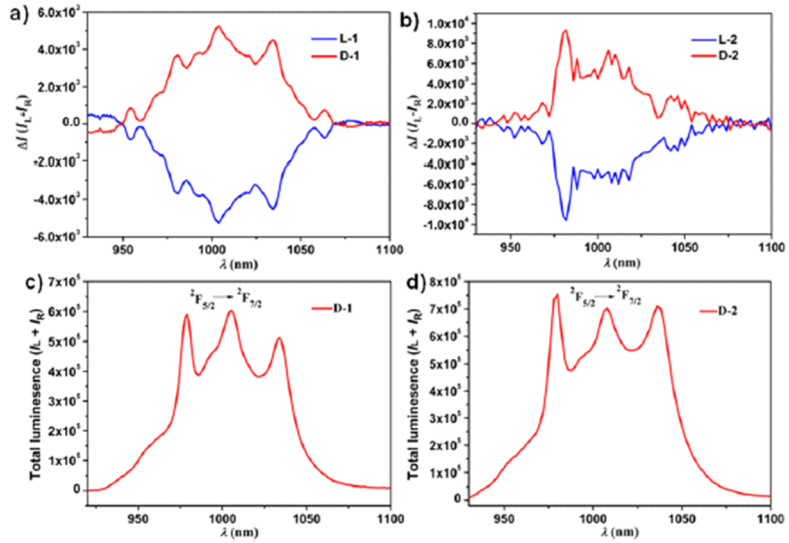

Scheme 11 (Above) Chemical structures of the ligands and Ln complexes (D-1/L-1 and D-2/L-2).[57] (Below) NIR-CPL spectra of D-1/L-1 (a) and D-2/L-2 (b) with total NIR emission profiles (c) and (d) for each enantiomeric pair in the solid state at room temperature. Reproduced from ref. 57 with permission from the Royal Society of Chemistry, copyright [2023].[57]

Open Access Article. Published on 02 April 2025. Downloaded on 4/4/2026 1:46:32 AM.
This article is licensed under a Creative Commons Attribution-NonCommercial 3.0 Unported Licence.

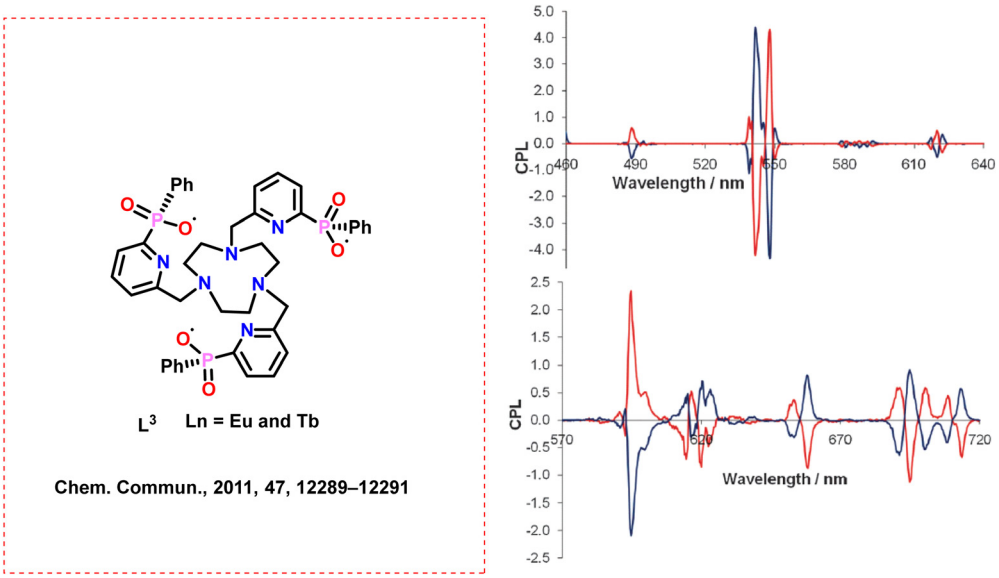

Scheme 12 (Left) Chemical structures of the ligands (L^3) and Ln complexes.[61] (Right) Circularly polarised luminescence spectra for the Δ (red) and Λ(blue)-[Tb·L^3] (upper) and [Eu·L^3] (lower) (295 K, 1 : 1 aq. MeOH). Reproduced from ref. 61 with permission from the Royal Society of Chemistry, copyright [2011].[61]

In 2016, the same group introduced a class of chiral cyclen derivative-based, highly emissive, stable Ln compounds with strong CPL characteristics and high PLQYs (Scheme 16a).[63] The Eu(III) based complex, 5, could achieve high luminescence intensity and the g_{lum} value of +0.3 (DMSO) at the $^5D_0$ to $^7F_1$ transition. Similarly, the macrocyclic Eu(III) based complex, 7, could achieve the absolute g_{lum} of −0.23 at 589 nm in aqueous solution (Table 2). In DMSO solution, the macrocyclic Eu(III) based complex, 2, 3 and 4, could achieve the absolute g_{lum} of −0.18, 0.17 and −0.11 at 591 nm, respectively. The CPL spectra was measured using a custom-built spectrometer.

DeRosa *et al.* investigated the effects of solvents on the CPL and racemization kinetics of nine-coordinate chiral Eu(III) complexes ([Eu·L^{1-3}], Scheme 16b).[72] The nature of the solvent significantly affects the magnitude and sign of the emitted CPL signal. The allowed electric dipole $\Delta J = 2$ and $\Delta J = 4$ transitions depicted this behavior. Low-polarity aprotic solvents such as NMP and ethyl acetate enhance the CPL signal's intensity in the $\Delta J = 2$ manifold. They measured the CPL using a home-built (modular, PEM-CPL) spectrometer. They also observed that the choice of donor groups coordinating to Eu(III) and the polarity of the solvent influence the rate of racemization. Their work concluded that certain systems exhibit very long half-lives at room temperature in the non-polar medium.

2.3. Pyridine dicarboxylate-based ligands and chiral Ln complexes

The Ln^{3+} ions can strongly bind O atoms on the carboxyl and nitrogen atoms on the pyridine ring in pyridine dicarboxylate ligands. Muller *et al.* synthesized a chiral ligand (L^4) with asymmetric carbon-containing unit on the 4-position of the pyridine ring in 2001 (Scheme 17, above).[73] The synthesized

Table 2 Photophysical properties of cyclen and pyridine dicarboxylate-based chiral Ln complexes

Ln complex	Transition	Wavelength (nm)	Dissymmetry factor (g_{lum})	PLQY (%)	Ref.
ΔEuL^3	—	600	0.33 (1 : 1 MeOH/H_2O)	0.11	*Chem. Commun.*, 2011, **47**, 12289–12291[61]
ΔTbL^3	—	620	0.28 (1 : 1 MeOH/H_2O)	0.50	*Chem. Commun.*, 2011, **47**, 12289–12291[61]
[TbL3]$^-$	$^5D_4$ to $^7F_5$	542.5	0.285 (0.1 M of HEPES buffer)	—	*Inorg. Chem.*, 2019, **58**, 12506–12510[62]
[TbL4]$^{5-}$	$^5D_4$ to $^7F_5$	542.5	0.241 (0.1 M of HEPES buffer)	—	*Inorg. Chem.*, 2019, **58**, 12506–12510[62]
5	$^5D_0$ to $^7F_1$	591	+0.3 (DMSO)	40.4	*Inorg. Chem.*, 2016, **55**, 9065–9070[63]
7	$^5D_0$ to $^7F_1$	589	−0.23 (H_2O)	49.7	*Inorg. Chem.*, 2016, **55**, 9065–9070[63]
[Eu(3)$_3$]	—	619	0.06 (methanol)	—	*Dalton Trans.*, 2011, **40**, 12056–12059[64]
Eu(1*SS*)$_3$ (CF_3SO_3)$_3$	$^5D_0$ to $^7F_1$	—	0.22 (methanol)	4.4	*Chem. – Eur. J.*, 2013, **19**, 16181–16186[65]
Eu(2*RR*)$_3$ (CF_3SO_3)$_3$	$^5D_0$ to $^7F_1$	—	−0.24 (methanol)	4.4	*Chem. – Eur. J.*, 2013, **19**, 16181–16186[65]
Eu(1(*S*))$_3$	$^5D_0$ to $^7F_1$	589	0.16 (methanol)	1.6 ± 0.5	*Chem. Sci.*, 2015, **6**, 457–471[66]
Eu(1(*R*))$_3$	$^5D_0$ to $^7F_1$	589	−0.15 (methanol)	2.1 ± 0.1	*Chem. Sci.*, 2015, **6**, 457–471[66]
Eu·[2·(*S*,*S*)]$_3$	$^5D_0$ to $^7F_1$	589	0.16 (H_2O)	—	*Faraday Discuss.*, 2015, **185**, 413–431[67]
Eu·[2·(*R*,*R*)]$_3$	$^5D_0$ to $^7F_1$	589	−0.18 (H_2O)	—	*Faraday Discuss.*, 2015, **185**, 413–431[67]
[Eu·(1a)$_3$](CF_3SO_3)$_3$	$^5D_0$ to $^7F_1$	—	−0.016 (CH_3CN)	—	*Chem. – Eur. J.*, 2016, **22**, 486 – 490[68]
Sm·1$_3$	$^4G_{5/2}$ to $^6H_{5/2}$	—	−0.44 (CH_3CN)	—	*Dalton Trans.*, 2019, **48**, 11317–11325[69]
Sm·2$_3$	$^4G_{5/2}$ to $^6H_{5/2}$	—	0.29 (CH_3CN)	—	*Dalton Trans.*, 2019, **48**, 11317–11325[69]

This journal is © The Royal Society of Chemistry 2025

Open Access Article. Published on 02 April 2025. Downloaded on 4/4/2026 1:46:32 AM.
This article is licensed under a Creative Commons Attribution-NonCommercial 3.0 Unported Licence.

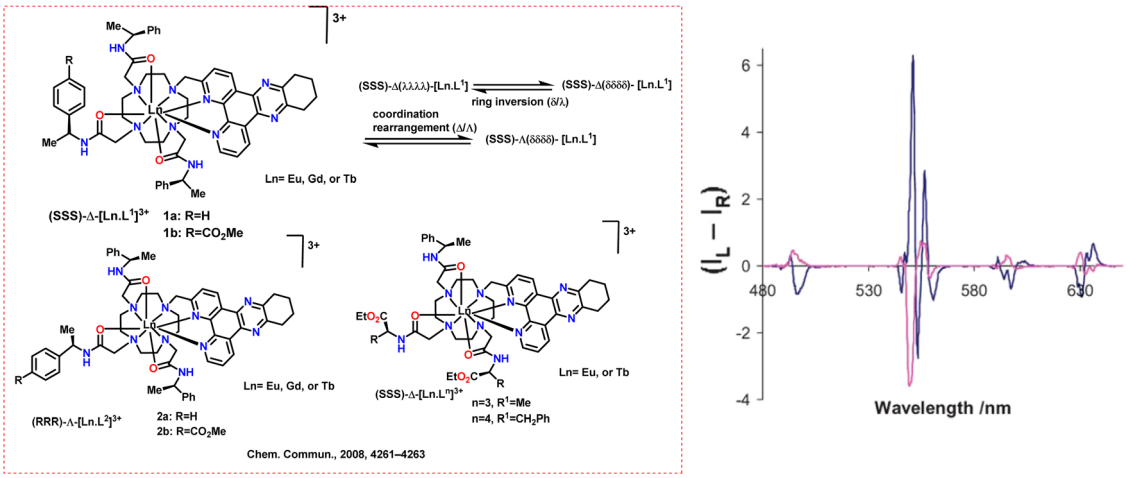

Scheme 13 (Left) Chemical structures of the ligands and Ln complexes.[70] (Right) CPL spectra for (*SSS*)-Δ-$[Tb{\cdot}L^{1b}]^{3+}$ (blue) and in the presence of added BSA (red) (295 K, D_2O, λ_{exc} 348 nm, 15 mM complex, and 30 mM protein; relative (I_L + I_R) = 60 on this scale). Reproduced from ref. 70 with permission from the Royal Society of Chemistry, copyright [2008].[70]

ligand depicts the interaction with trivalent Ln ions. In acetonitrile, the chiral binding ligand, L^4, produces stable $[Ln(L^4)_3]^{3+}$ complexes with stability constant values ($\log \beta_3$) between 19 and 20. The specific rotational dispersion of the complexes is around 10 times greater than that of the ligand alone. The NMR data shows only one time-averaged species with a trigonal symmetry present in the acetonitrile solution. The helical *P* to *M* interconversion quickly occurs on the NMR time scale. CPL depicts weak effects on the Eu and Tb triple helical complexes, suggesting little diastereomeric excess in the solution. The CPL spectra of $[Ln(L^4)_3]^{3+}$ for the $^5D_0$ to $^7F_1$(Eu) transition and $^5D_4$ to $^7F_5$ (Tb) transition is depicted in Scheme 17 (below). The CPL spectrum of the $^5D_4$ to $^7F_5$ (Tb) transition displays peaks corresponding to crystal-field splitting of the electronic levels and the calculated g_{lum} factor is 0.02.

A few symmetrical lanthanide bundles of the chiral Ln(1 or 2)$_3$ (Ln(III) = (Tb, Sm, Eu, Nd, and Yb)) complex were reported by Gunnlaugsson's group in 2007.[74] The enantiomers of 1-[1-naphthyl]-ethylamine and 2,6-pyridinedicarbonyl dichloride were reacted in a mixed solvent of triethylamine and anhydrous THF to yield chiral ligands 1 or 2 (Scheme 18). Two naphthalene sidearms on the pyridine ring in chiral ligands 1 or 2 have a "winglike" conformation that primarily contributes to its chirality. Different chiral ligands and $Ln(CF_3SO_3)_3$ combinations were reacted to synthesize the complex. These ligands could interact with Ln^{3+} through the N atoms on the pyridine ring and the O atoms on the side carboxamide groups. Through π–π staking interactions, the naphthalene units on the neighbouring two ligands encircle the central pyridine ring on one ligand, completely arranging in a helical style to wrap around Ln^{3+}. For 1·Sm and 2·Sm, the CPL

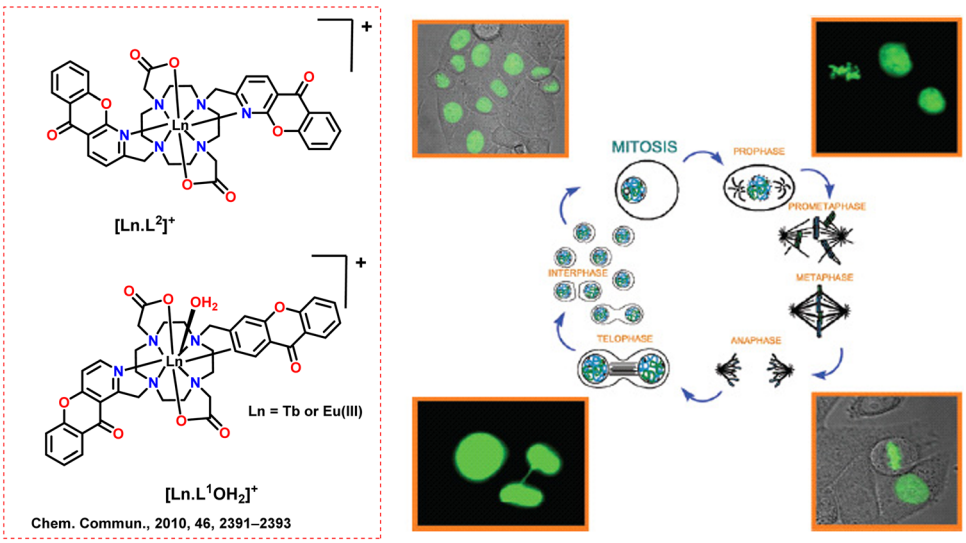

Scheme 14 (Left) Molecular structures of some cyclen-based ligands and chiral Ln complexes ($[LnL^2]^+$ and $[LnL^1]^+$).[71] (Right) Bright field (upper left and lower right) and fluorescence microscopy images of HeLa cells undergoing mitosis, with an illustrative of the cell cycle (0.5 mM, $[Tb{\cdot}L^2]Cl$, 3 h, λ_{exc} 350 nm). Reproduced from ref. 71 with permission from the Royal Society of Chemistry, copyright [2010].[71]

Open Access Article. Published on 02 April 2025. Downloaded on 4/4/2026 1:46:32 AM.
This article is licensed under a Creative Commons Attribution-NonCommercial 3.0 Unported Licence.

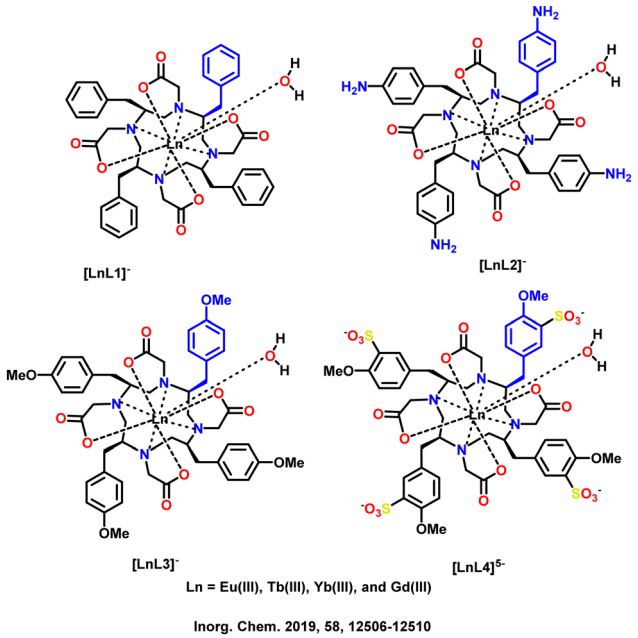

Scheme 15 Molecular structures of some cyclen-based ligands and chiral Ln complexes. Adapted from ref. 62.

signals are of equal and opposite sign and are 0.28 and 0.50 for the 600 and 560 nm bands, respectively.

The same group in 2011 showed the synthesis of chiral Eu complexes *via* 3 (*R*) and 4 (*S*) ligands (Scheme 19, left) and $Eu(CF_3SO_3)_3$ with 3 : 1 stoichiometry in acetonitrile solution using time-dependent UV-vis absorption and emission spectra.[64] The developed complexes had "half helicates" geometry. Three outer ligands were oriented toward the "half helicates" in the crystal structures of [Eu(3 or 4)$_3$], leaving the methyl groups outside of the central Eu^{3+}. The π–π interactions between neighbouring antennas allowed for this design. Consequently, [Eu(3)$_3$] exhibits g_{lum} factors of 0.06 and −0.15 at 619 and 600 nm, respectively (Table 2). The CPL and CD spectra of $3_3{\cdot}Eu_1$(red) and $4_3{\cdot}Eu_1$ (blue) are depicted in Scheme 19 (right).

Similarly, when ligands 1 (*S*,*S*) and 2 (*R*,*R*) (Scheme 20, above) are combined with Tb or Eu to form self-assembly complexes, they only produce the 2 : 1 (Ligand : Ln) stoichiometry rather than the predicted 3 : 1 stoichiometry.[75] When 0.5 equivalents of $Tb(CF_3SO_3)_3$ are added to the ligand, the absorption intensity shows a hyperchromic effect in *in situ* UV-vis spectra. Raising $Tb(CF_3SO_3)_3$ to one equivalent only results in a small absorption intensity increase. Absorption saturation is reached when the equivalent of $Tb(CF_3SO_3)_3$ is above 1. Similarly, the emission of Tb^{3+} increases between 0 to 1 equivalents before stabilizing at over one equivalent of Tb^{3+}. This verifies that the preferred self-assembly complexes in this chemical system are [Ln(1 or 2)$_2$] rather than the anticipated [Ln(1 or 2)$_3$]. The variations in the UV-vis absorption spectrum of 1 upon titration with $Tb(CF_3SO_3)_3$ and the corresponding deviations in the Tb(III) emission are depicted in Scheme 20 below.

They also investigated the impact of ligand isomerism in solution and the solid state.[65] They developed several chiral 1- and 2-naphthyl derivatives of picolinic acid (1(*S*,*S*) and 2(*R*,*R*), 1′(*S*,*S*) or 2′(*R*,*R*)) (Scheme 21) and their Eu(III) complexes ($EuL_3(CF_3SO_3)_3$) that can self-assemble in methanol and acetonitrile. The Eu(III) center is completely shielded from solvent molecules by these species' strong binding constants with the Eu(III) ion. This leads to the formation of assemblies with 1 : 3 Ln to ligand stoichiometries. Every Ln complex produces CPL emission, verifying the enantiomer pairs. The chirality of the Eu(III) complexes of 1(*S*,*S*) and 2(*R*,*R*) is validated by the X-ray crystal structure data. This crystal structure also shows that the ion is more densely packed because of higher π–π stacking between the pyridyl and naphthalene groups than for those formed from 1′(*S*,*S*) or 2′(*R*,*R*).

The same group synthesized chiral asymmetrical ligands 1(*S*) and 1(*R*) in 2015. Following their reaction with Eu(III) ions, these ligands form red emissive complexes of Eu(1(*S*))$_3$ and Eu(1(*R*))$_3$, respectively (Scheme 22, left).[66] The complexes have PLQY of around 2% in acetonitrile solution. The self-assembly formation between chiral ligands and Eu compounds was analyzed using various spectroscopic techniques. In each case, the analysis points to the sequential development of M:L, M:L$_2$, and M:L$_3$ assemblies with similar binding constant values. The chirality transfer from the ligand to the metal centers displays the distinctive Eu(III) CPL bands (Scheme 22, right). This makes it possible to determine the absolute stereochemistry of the self-assemblies for Eu(1(*S*))$_3$ (clockwise) and Eu(1(*R*))$_3$ (anticlockwise). They confirmed it for Eu(1(*R*))$_3$ by comparing it with the solid-state crystallographic data. The luminescence dissymmetry factors g_{lum} for $^5D_0$ to $^7F_1$ transitions are 0.16 and −0.15, while g_{lum} for $^5D_0$ to $^7F_2$ transitions for the Eu(III) complex with 1(*S*) and 1(*R*) are −0.09 and 0.10, respectively. An argon ion laser was used as a pump source. The optical detection system comprised of a PEM (Hinds Int.) operating at 50 kHz and a linear polarizer. The emitted light is detected by a cooled EM1-9558QB photomultiplier tube.

In the same year, they reported the synthesis and use of water-soluble chiral ligands (2(*R*,*R*) and 2(*S*,*S*)) (Scheme 23, above) in the Ln self-assembled structure building process.[67] The synthesized ligands unit had two naphthalene moieties acting as sensitizing antennae, which could be employed to fill the excited state of Ln ions. These ligands were structurally altered by adding a water-solubilizing sulfonate motif using 3-propanesulfone. Eu(III) and these ligands form chiral complexes using microwave synthesis in 1 : 3 (M : L) stoichiometries. The red Eu(III)-based emission from these developed complexes has PLQY of 12% in water. The chiroptical studies (CD and CPL analysis, Scheme 23 (below)) indicate that the compounds are chiral. The self-assembly between chiral ligands with Eu(III) *in situ* was also examined using variations in the Eu(III) centered emission and the ligands' absorption. Through these modifications, they could investigate the different stoichiometries of the metals and ligands. The g_{lum} values calculated from the Eu(III) transitions in the CPL spectra of Eu·[2·(*R*,*R*)]$_3$ and Eu·[2·(*S*,*S*)]$_3$ (in H_2O) are 0.16 and −0.18 at 589 nm, respectively. Excitation of Eu(III) (560–581 nm) was accomplished using a Coherent 599 tunable dye laser with an argon ion laser as a pump source. The

This journal is © The Royal Society of Chemistry 2025

Open Access Article. Published on 02 April 2025. Downloaded on 4/4/2026 1:46:32 AM.
This article is licensed under a Creative Commons Attribution-NonCommercial 3.0 Unported Licence.

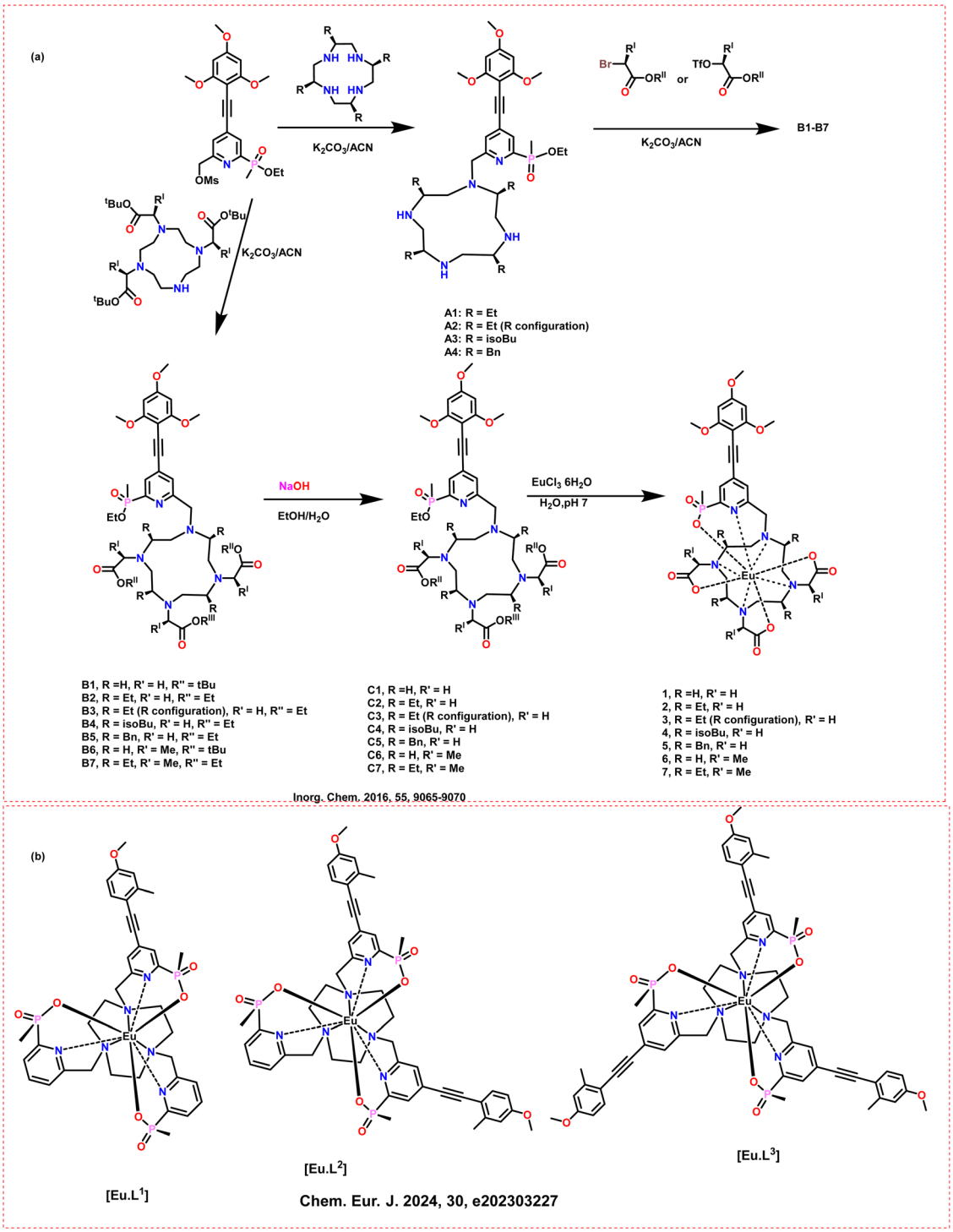

Scheme 16 Molecular structures of some cyclen-based ligands and chiral Ln complexes (a) (1 to 7);[63] (b) ([Eu·L$^{1-3}$]) complex.[72]

optical detection system consisted of a photoelastic modulator (PEM, Hinds Int.) operating at 50 kHz and a linear polarizer. The emitted light was detected by a cooled EM1-9558QB photomultiplier tube.

Gunnlaugsson's group demonstrate easy synthesis of enantiomers of chiral ligands (1–3, Scheme 24) from chiral amines and bisalkyne in 2016.[68] They grew the crystal structures for enantiomers of ligand 1. These ligands could complex with Eu(III) and Tb(III), which shows luminescence centered on Ln(III). The chiral character of the ligands was investigated using CD and CPL spectroscopy (Table 2). The g_{lum} for the most intense transitions in the Eu(III) complex for $^5D_0$ to $^7F_1$ and $^5D_0$ to $^7F_2$ transitions are −0.016 and +0.023, respectively for 1a. The dissymmetry factor for the $^5D_0$ to $^7F_3$ transition of

Open Access Article. Published on 02 April 2025. Downloaded on 4/4/2026 1:46:32 AM.
This article is licensed under a Creative Commons Attribution-NonCommercial 3.0 Unported Licence.

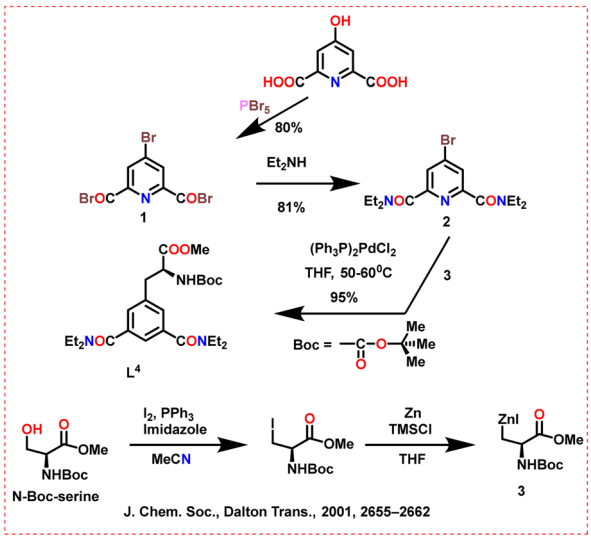

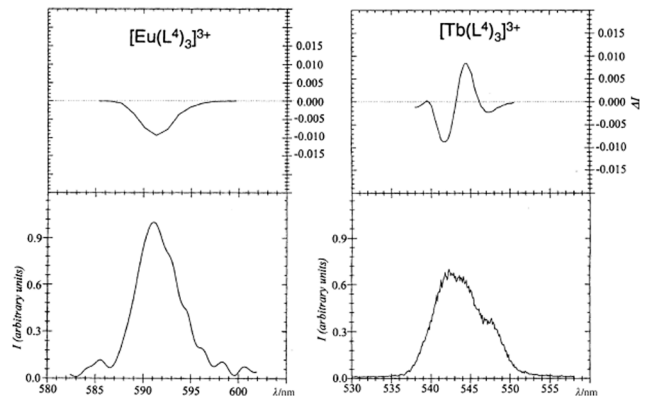

Scheme 17 (Above) Chemical structures of the ligands.[73] (Below) CPL spectra of $[Ln(L^4)_3]^{3+}$, 10^{-3} M in anhydrous CH_3CN at 298 K, upon excitation at 320 nm. Left: $^5D_0$ to $^7F_1$(Eu) transition, right: $^5D_4$ to $^7F_5$ (Tb) transition. Reproduced from ref. 73 with permission from the Royal Society of Chemistry, copyright [2001].[73]

the TbIII complexes are +0.085 for 1a and −0.081 for 1b. A tuneable dye laser was used to excite Ln(III) emission with an argon ion laser as a pump source. The optical detection system consists of a photoelastic modulator operating at 50 kHz and a linear polarizer. Emitted light was detected by a cooled photomultiplier tube.

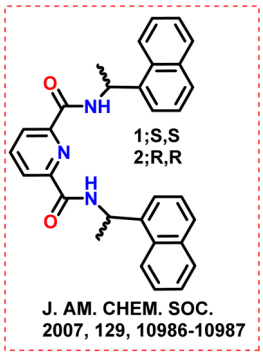

Scheme 18 Chemical structures of ligands 1 and 2.[74]

Further, the same group synthesized chiral 2,6-pyridine dicarboxylic acid-based ligands in 2019 (1 and 2, Scheme 25, left).[69] The different Ln salts used for the complexation process of $Ln(CF_3SO_3)_3$ were Lu(III), Sm(III), Tb(III), and Dy(III). They used the expected formation of 1 : 3 and 1 : 1 Ln : ligand species in solution for evaluation. They also measured the CD and CPL spectroscopic studies for Tb(III) and Sm(III). The changes in CD spectra of 1*R* upon the addition of $Sm(CF_3SO_3)_3$ is depicted in Scheme 25 (right). Ligand chirality was preserved and transferred to the lanthanide center upon complexation. High dissymmetry factor values were obtained for the Sm(III) complexes (g_{lum} = −0.44 and 0.29 for the $^4G_{5/2}$ to $^6H_{5/2}$ transitions of $Sm{\cdot}1_3$ and $Sm{\cdot}2_3$, Table 2). Excitation was performed using a Coherent 599 tuneable dye laser with an argon ion laser as a pump source. The optical detection system comprised of a PEM (Hinds Int.) operating at 50 kHz and a linear polarizer. The emitted light was sensed by a cooled EM1-9558QB photomultiplier tube.

2.4. Linking through multiple oxygen and nitrogen atoms: some polydentate ligands and chiral Ln complexes

Petoud *et al.* described significant CPL activity of chiral-, octadentate-, and 2-hydroxyisophthalamide ligands in 2007.[76] These ligands exhibit excellent luminescence characteristics when combined with lanthanide ions in solution. They achieved one ligand system (Scheme 26) that can sensitize four distinct luminous lanthanide cations (Sm(III) and Eu(III), Dy(III) and Tb(III), [Ln*R*(+) and *S*(−)BnMeH22IAM]). Furthermore, the developed Sm(III) complex with chiral ligand has CPL activity. The total PLQY of the Eu(III) complex is low, even though it exhibits high CPL intensities. Although the Tb(III) complex has a significantly higher quantum yield, the CPL effect is less pronounced. The g_{lum} and quantum yield values of the complexes is depicted in Table 3.

High CPL brightness is needed to realize the promising potential of CPL emitters. Deng *et al.* 2020 reported the synthesis of enantiopure H8-Binol ligand-based Ln complexes ($[(R/S\text{-}H_8\text{-Binol})_3LnNa_3(thf)_6]$; Ln = Sm, Tb, and Dy) with *C*3-symmetry (Scheme 27, above).[77] These complexes demonstrate visible luminescence in solution, displaying strong CPL for Sm, Tb, and Dy with high luminescence dissymmetry factors (maximum $|g_{lum}| \sim 0.44$). These metal complexes also possess high PLQYs for Sm (4%) and Dy (17%). The spectra of the two enantiomers $[(R/S\text{-}H_8\text{-Binol})_3SmNa_3]$ are exact mirror images (Scheme 27, below). The transition from $^4G_{5/2}$ to $^6H_{7/2}$ has the largest dissymmetry factor (0.44) at 603 nm. At 576 nm, a marginally lower CPL active signal ($|g_{lum}|$ = 0.31) was noted during the $^4G_{5/2}$–$^6H_{5/2}$ transition, (Table 3). CPL was measured with an Olis CPL Solo instrument.

Further, the same group attained CPL in two near-infrared subregions in 2022.[78] They synthesized the rigid binolate complexes (Scheme 28) of erbium $[(Binol)_3ErNa_3]$ with a very high dissymmetry factor ($|g_{lum}|$) of 0.47 at 1550 nm. These chiral erbium compounds could emit beyond 1200 nm. Their group observed that compounds of ytterbium and neodymium also show substantial CPL ($|g_{lum}|$ = 0.17 and 0.05, respectively, Table 3) in a higher energy wavelength region (800–1200 nm).

This journal is © The Royal Society of Chemistry 2025

Open Access Article. Published on 02 April 2025. Downloaded on 4/4/2026 1:46:32 AM.
This article is licensed under a Creative Commons Attribution-NonCommercial 3.0 Unported Licence.

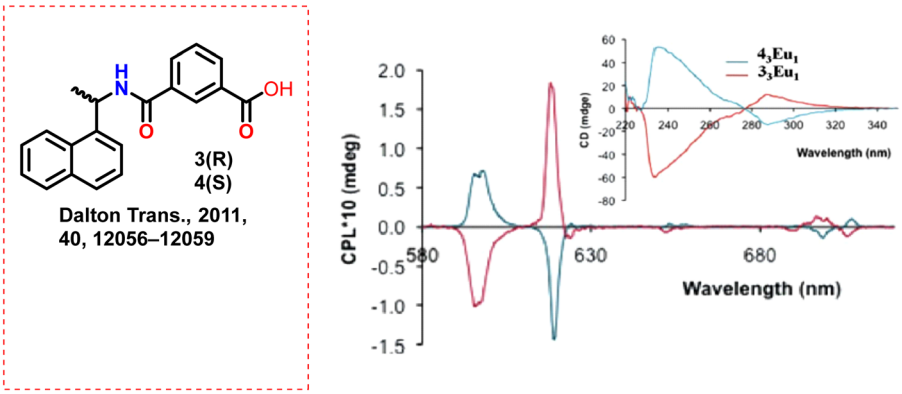

Scheme 19 (Left) Chemical structures of ligands 3 and 4.[64] (Right) Eu(III) circular polarised emission spectra arising from 3_3·Eu_1(red) and 4_3·Eu_1 (blue). Inset: CD spectra of both complexes. Reproduced from ref. 64 with permission from the Royal Society of Chemistry, copyright [2011].[64]

All the developed complexes show high PLQYs (Er: 0.58%, Yb: 17%, Nd: 9.3%). For [(*S*-Binol)$_3$ErNa$_3$], a tetrasignate pattern is seen at 1540 nm with an extraordinarily high maximum dissymmetry factor of +0.47. The enantiomer [(*R*-Binol)$_3$ErNa$_3$] shows a dissymmetry value of −0.47 at 1540 nm and its spectra are a perfect mirror image. The CPL was measured using an Olis NIRCPL Solo instrument.

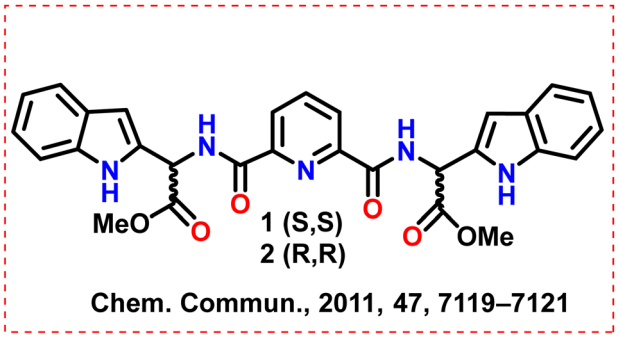

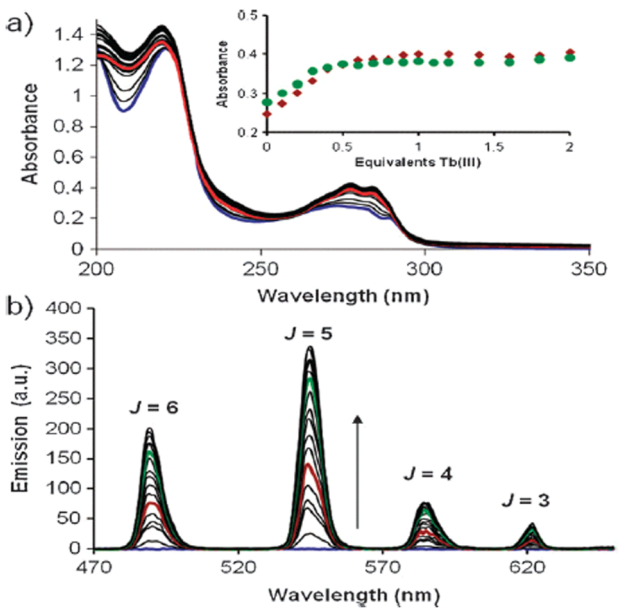

Scheme 20 (Above) Chemical structures of ligands 1 and 2.[75] (Below) (a) Changes in the UV-vis absorption spectrum of 1 (upon titration with Tb(CF_3SO_3)$_3$) in CH_3CN. Inset: The changes at 275 nm for 1_2Tb and 2_2Tb. (b) Corresponding changes in Tb(III) emission. Reproduced from ref. 75 with permission from the Royal Society of Chemistry, copyright [2011].[75]

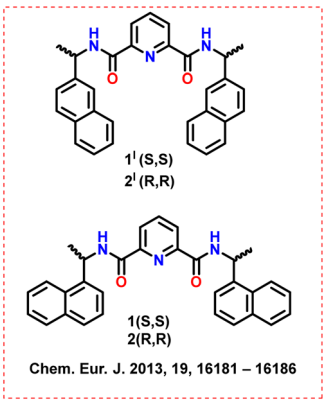

Scheme 21 Chemical structures of the ligands (1(*S*,*S*) and 2(*R*,*R*), 1′(*S*,*S*) or 2′(*R*,*R*)).[65]

Raymond's group present a novel class of Ln compounds assembled on chelating units of 2-hydroxyisophthalamide in 2003.[99] Their group synthesized the macrobicycle H_3L^1 and the octadentate ligand H_4L^2. These ligands develop stable and luminous Ln complexes (Ln = Sm, Eu, Tb, and Dy, Scheme 29a). Reaction of ligands with Ln(NO_3)$_3$ or $LnCl_3$ (where Ln = Sm, Eu, Tb, or Dy), two molecules of H_3L^1 or one of H_4L^2 yield the complexes [(Ln(H_2L^1)$_2$)]Br and [Ln(H_2L^2)]Br, respectively. They developed single crystals of the [(Eu(H_2L^1)$_2$)]Br complex by slowly allowing acetone to diffuse into a complex solution in a DMF, water, and MeOH combination. The developed ligands effectively sensitized several lanthanide cations emitting in the visible spectrum. When the lanthanide was introduced to the ligand solution, the emission from the ligand disappeared, indicating effective ligand-to-lanthanide energy transfer. The same group in 2007 synthesized multidentate ligands ($H_4$1 and $H_4$2, Scheme 29b) and highly emissive, enantiopure, and water-soluble Eu(III) and

Open Access Article. Published on 02 April 2025. Downloaded on 4/4/2026 1:46:32 AM.
This article is licensed under a Creative Commons Attribution-NonCommercial 3.0 Unported Licence.

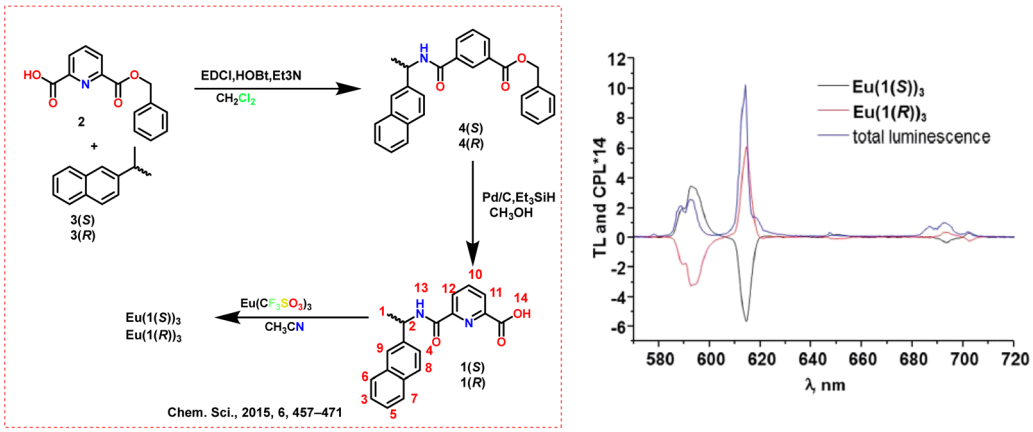

Scheme 22 (Left) Chemical structures of the ligands (1(*S*), 1(*R*)) and Ln complexes Eu(1(*S*))$_3$ and Eu(1(*R*))$_3$.[66] (Right) CPL spectra for EuL$_3$ in CH_3OH (L = 1(*S*), 1(*R*)). Reproduced from ref. 66 with permission from the Royal Society of Chemistry, copyright [2015].[66]

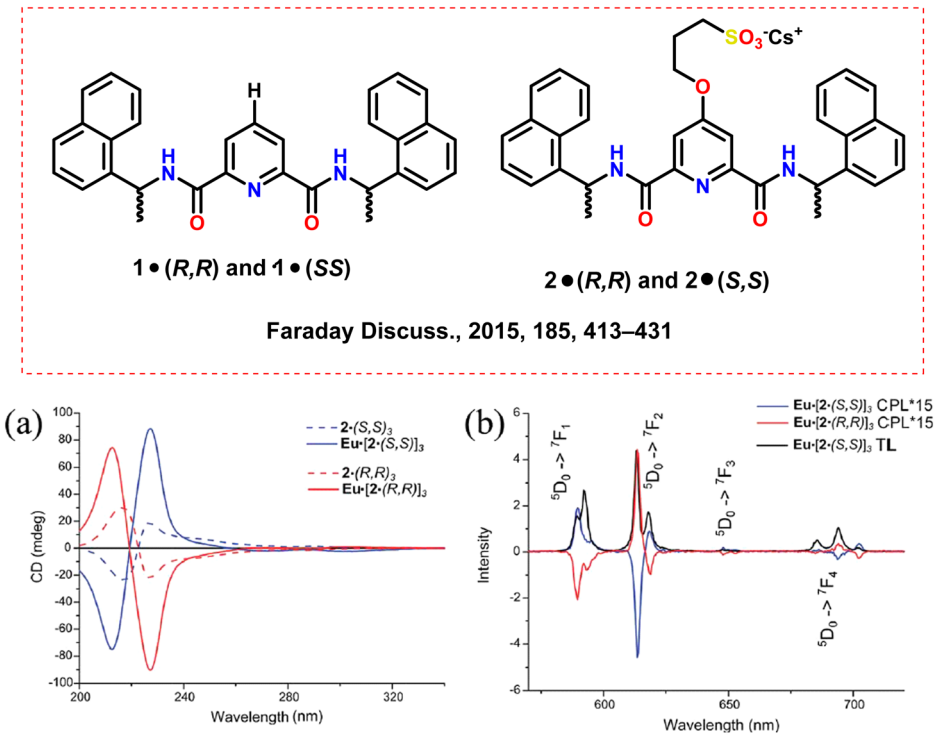

Scheme 23 (Above) Chemical structures of the ligands (2(*R*,*R*) and 2(*S*,*S*)).[67] (Below) (a) Overlaid CD spectra from 2·(*S*,*S*)$_3$, 2·(*R*,*R*)$_3$ (dashed) at 1×10^{-5} M and Eu·[2·(*R*,*R*)]$_3$, Eu·[2·(*S*,*S*)]$_3$ (solid) at 3.3×10^{-6} M in water at 24 °C (b) CPL and total luminescence (TL) spectra recorded for Eu·[2·(*R*,*R*)]$_3$ and Eu·[2·(*S*,*S*)]$_3$ in water. Reproduced from ref. 67 with permission from the Royal Society of Chemistry, copyright [2015].[67]

Tb(III) complexes.[79] Both [Tb(H$_2$)] and [Eu(H$_1$)(H$_2$O)] complexes exhibit high luminescence and are soluble in aqueous solutions. Complex [Eu(H$_1$)(H$_2$O)] has the same position of the UV absorption maximum for the n–σ* transition as in a similar complex with the achiral ligand. In aqueous environments, the quantum yield for [Tb(H$_2$)] is very high (~0.57). Similarly, the PLQY of [Eu(H$_1$)(H$_2$O)] (0.077) falls within the range of commercially available Eu(III) luminous probes. These Tb- and Eu-containing water-soluble compounds show comparatively high CPL activity (g_{lum}), with −0.083 {Tb($^5D_4$ to $^7F_5$)} and −0.12 {Eu($^5D_0$ to $^7F_1$)} (Table 3).

Harada *et al.* synthesized Eu(III) complexes with point- and axis-chiral ligands that exhibit CPL: [Eu((*R*/*S*)-BINAPO)(D-facam)$_3$], [Eu(TPPO)$_2$(D-facam)$_3$], [Eu(BIPHEPO)(D-facam)$_3$] and [Eu((*R*)-BINAPO)(hfa)$_3$] in 2009 (Scheme 30).[80] The CPL dissymmetry factors are 0.44 [Eu((*R*)-BINAPO)(D-facam)$_3$], 0.34 [Eu((*S*)-BINAPO)-(D-facam)$_3$], 0.24 [Eu(BIPHEPO)(D-facam)$_3$], and 0.47 [Eu(TPPO)$_2$-(D-facam)$_3$] (Table 3). There is a somewhat lesser dissymmetry factor for [Eu((*R*)-BINAPO)(hfa)$_3$] ($|g_{CPL}|$ = 0.03). CPL spectra were measured with a JASCO CPL-200 spectrometer. The terminal P═O groups in ligands and TPPO interacted with Eu^{3+} to make

 This journal is © The Royal Society of Chemistry 2025

Open Access Article. Published on 02 April 2025. Downloaded on 4/4/2026 1:46:32 AM.
This article is licensed under a Creative Commons Attribution-NonCommercial 3.0 Unported Licence.

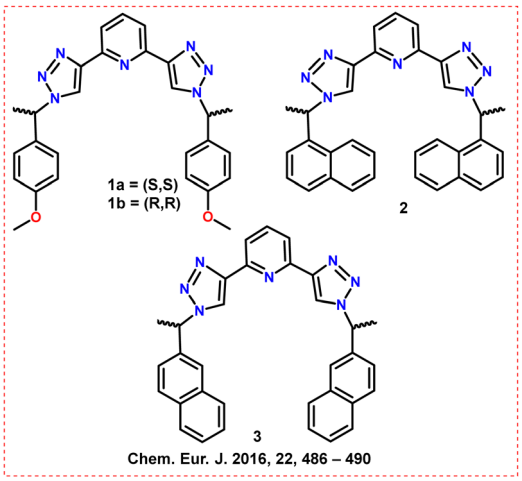

Scheme 24 Chemical structures of ligands 1, 2 and 3.[68]

Eu–O bonds. The $[Eu(TPPO)_2(D\text{-facam})_3]$ complexes crystallize in a square antiprism geometry.

Further, their group studied an Eu(III) chiral coordination polymer, $[Eu(hfa)_3((R)\text{-bidp})]_n$, using a structural transformation system in 2017 (Scheme 31).[81] The Eu(III) coordination polymer has a helical polymer structure and distinctive hydrogen–fluorine/π interactions in the crystal. The compound exhibits strong PLQY (76%) and high thermostability in the solid form. The emission spectra of the complex transformed in solution. Photophysical studies reveal that the coordination polymer in solution changes into distinct complexes. These individual complexes exhibit chiroptical features in liquid medium. CPL was measured using a JASCO CPL-300 spectrofluoropolarimeter.

Tsurui *et al.* synthesized four Eu(III) complexes in 2020: $[Eu(hfa)_3((R,R)/(S,S)\text{-B2QPO})]$ and $[Eu(hfa)_3((R)/(S)\text{-B3QPO})]$ (Scheme 32, above).[82] These complexes include point-chiral phosphine oxide ligands. $[Eu(hfa)_3((R,R)\text{-B2QPO})]$ shows a significant g_{CPL} value of 0.08 and high PLQY (55% in dichloromethane and 63% in solid). The ligands in $[Eu(hfa)_3((R,R)\text{-B2QPO})]$ have a higher structural strain. This large strain results in an additional LMCT band in the CD signals of this complex. The CPL spectra of the developed complexes are depicted in Scheme 32 (below).

Controlling stereoselectivity in self-assembly of lanthanide helicate is problematic due to low stereochemical preference and fluctuating coordination numbers in Ln(III). A pair of triple-stranded helical enantiomeric complexes were synthesized by Liu *et al.* in 2018 (Ln(TTEA)((*R/S*)-BINAPO), Ln = La, Eu, Gd, Scheme 33).[83] The chiral BINAPO ligand stimulates the assembly of achiral tris-β-diketone ligands (TTEA) with Ln(III) ion. This stimulation by the chiral ligand results in a homochiral helical-shaped structure. They grew the single crystal of the Ln complex. Examination of the crystal structure revealed that the formation of one-handed helical sense in achiral tris-β-diketone was induced by intramolecular hydrogen bonding. The chiroptical activities of the TTEA ligand in the excited state were also induced by the chiral BINAPO ligand. It causes intense CPL in the Eu(III) complexes and greatly increases their PLQYs. The developed complex displays PLQY of 32.8% and strong CPL with $|g_{lum}|$ values up to 0.072 (Table 3). CD and CPL were measured using an Olis DM 245 spectrofluorimeter.

Bari's group developed CPL-NIR emissive Yb and diketonate-based complexes in 2019 (Scheme 34a).[84] The developed complexes emit in the 920–1050 nm range through f–f transitions. The PLQY of the complexes show good quantum yields for $Yb(TTA)_3iPrPyBox$ (0.69%) and $Yb(TTA)_3PhPyBox$ (0.62%). The CPL of $Yb(TTA)_3iPrPyBox$ in DCM solution was measured between 900–1050 nm. A manifold with positive and negative bands was observed, which can be connected to the $^2F_{7/2}$ to $^2F_{5/2}$ transitions. The CPL band for the complexes was observed at 972 nm, with g_{lum} of −0.025 and +0.029 for the (*R,R*) and (*S,S*) enantiomers, respectively. The NIR-CPL spectra were measured using a home-built spectrofluoropolarimeter.

The same group investigated enantiopure chiral trivalent lanthanide complexes (Ln^{3+} = Eu^{3+}, Gd^{3+}, La^{3+}, Sm^{3+}, Tm^{3+}, and Yb^{3+}) using achiral tris(β-diketonate) based ligands and a chiral PyBox unit as a neutral auxiliary ligand in 2018 (Scheme 34b).[85] They investigated various optical and chiroptical characteristics (CD and CPL) in the UV to IR range. They recorded CPL and PL spectra in DCM for the iPrPyBox and PhPyBox ligands ($Sm(HFA)_3$-PyBox and $Sm(TTA)_3$-PyBox). Three distinct transitions were observed in the case of Sm(3+) complexes: $^4G_{5/2}$ to $^6H_{5/2}$ at 561 nm, $^4G_{5/2}$ to $^6H_{7/2}$ at 596 nm, and $^4G_{5/2}$ to $^6H_{9/2}$ at 643 nm. The CPL spectra show richer multiplets inside each

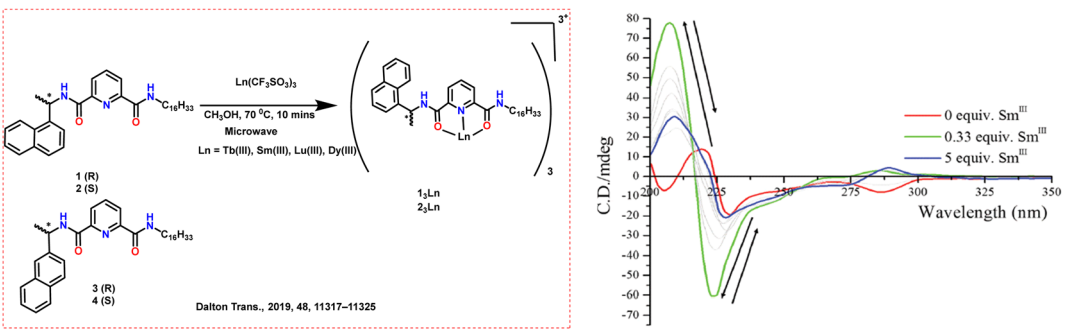

Scheme 25 (Left) Chemical structures of ligands and Ln complexes.[69] (Right) Overall changes in the CD spectra of 1(*R*) (3.4×10^{-5} M) upon titrating against increasing concentrations of $Sm(CF_3SO_3)_3$ (0 to 5 equiv.) at RT in CH_3CN. Reproduced from ref. 69 with permission from the Royal Society of Chemistry, copyright [2019].[69]

Open Access Article. Published on 02 April 2025. Downloaded on 4/4/2026 1:46:32 AM.
This article is licensed under a Creative Commons Attribution-NonCommercial 3.0 Unported Licence.

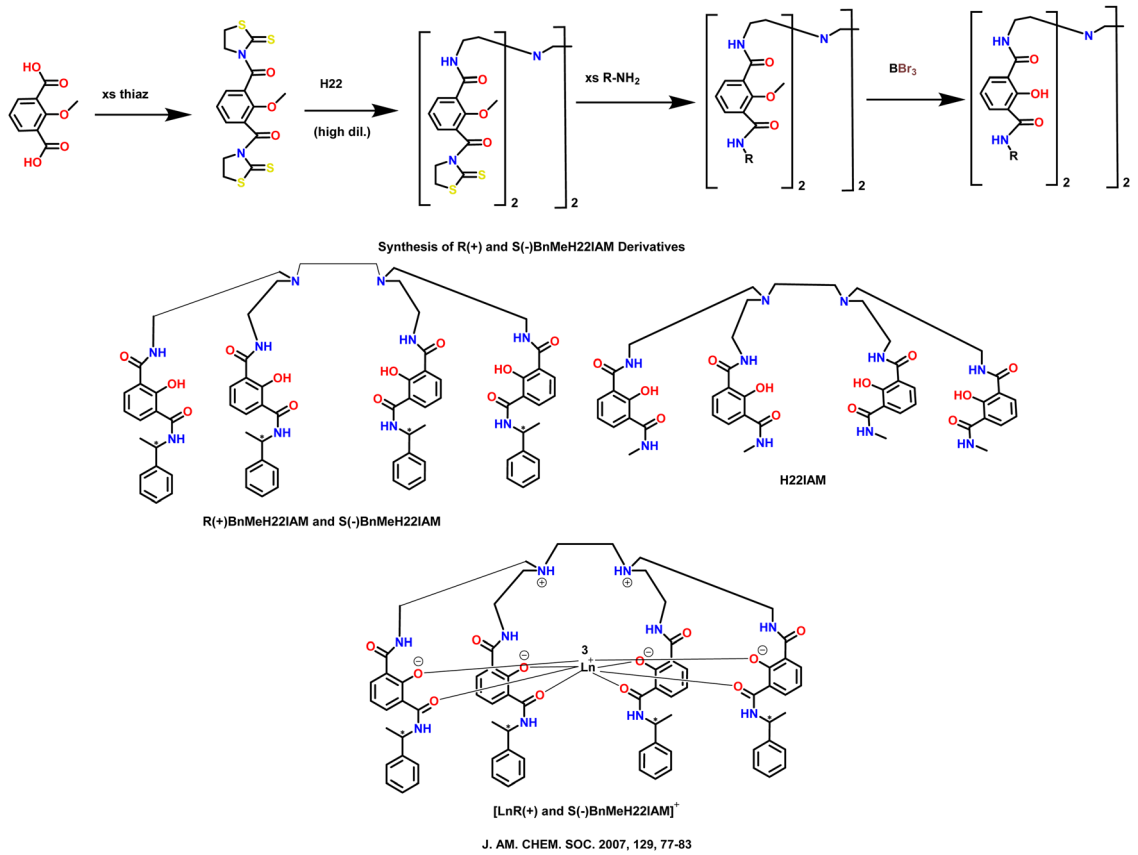

Scheme 26 Molecular structures of some polydentate ligands and complexes [Ln*R*(+) and *S*(−)BnMeH22IAM].[76]

spectroscopic term than their PL counterparts. The complexes of Sm^{3+} containing iPrPyBox exhibit the greatest $|g_{lum}|$ factors at the most intense CPL transition at 595 nm ($Sm(HFA)_3$-(*R*)-iPrPyBox) (|0.18|) and $Sm(TTA)_3$-(*R*)-iPrPyBox (|0.10|) (Table 3). The g_{lum} value is lower for complexes with PhPyBox (∼0.035).

In 2011, Yuasa *et al.* studied the opposite chiroptical activity of Europium-based complexes.[86] These complexes comprise achiral HFA and various chiral ligands (Scheme 35). Single crystal X-ray studies found noncovalent interactions between chiral pybox ligands and achiral HFA ligands in three complexes: π–π stacking in [(Eu(III)(*R*)-Ph-pybox)$(HFA)_3$], CH–F interactions in [(Eu(III)(*R*)-i-Pr-pybox)$(HFA)_3$,], and CH–π interactions in [(Eu(III)(*R*)-Me-Ph-pybox)$(HFA)_3$]. These intermolecular interactions cause asymmetric arrangements of surface HFA ligands, resulting in lanthanide complexes with inherent chirality. These intermolecular interactions also cause varying structural geometries in complexes. During the $^5D_0$ to $^7F_1$ transition of Eu^{3+}, [(Eu(III)(*R*)-Ph-pybox)$(HFA)_3$] has a positive g_{lum} of 0.15, whereas [(Eu(III)(*R*)-i-Pr-pybox)$(HFA)_3$], and [(Eu(III)(*R*)-Me-Ph-pybox)$(HFA)_3$] have negative g_{lum} of −0.46 and −0.35, respectively (Table 3).

Song *et al.* observed chirality transfer from D- and L-proline polymers to TTA-cooperated europium complexes (Scheme 36a), with the maximum g_{lum} factor of +0.41 for L-proline and ∼0.42 for D-proline at 596 nm for the $^5D_0$ to $^7F_1$ transition of Eu^{3+}.[87] Proline could cause circularly polarized luminescence in Eu(III) containing polymers. The polymer has a much larger optical anisotropy factor (g_{lum}) during the $^5D_0$ to $^7F_1/^7F_2$ transition than a single model molecule. CPL emission was amplified due to the conjugated polymer structure. CPL was measured using the DSM 17 CD polarization spectrophotometry system.

Leonzio *et al.* in 2018 developed a novel chiral complex, $[EuL(tta)_2(H_2O)]$, where the ligand L is mentioned in Scheme 36b.[88] The solid-state structure contains one chiral L, two tta, and one water molecule attached to the metal center. The ligand L and tta molecules efficiently capture and transport UV light absorbed between 250 and 400 nm to Eu(III). The $^5D_0$ to $^7F_2$ emission band dominates the Eu(III) emission spectra in solid state and acetonitrile or methanol solvent. The quantum yield of the metal ion was 40–50%. The enantiopure complex emitted highly polarized light, with a maximum emission dissymmetry factor (g_{lum}) of 0.2 in methanol solution. When Eu(III) is dissolved in methanol, its initial coordination sphere contains one CH_3OH molecule instead of water, as opposed to the solid state or acetonitrile solution. These two solvents have distinct Eu(III) CPL fingerprints. The CPL spectra were measured using a homemade spectrofluoropolarimeter.

Atzori's group observed magneto-chiral dichroism *via* light absorption in an enantiopure lanthanide complex in 2021.[100] The *P* and *M* enantiomers of [Yb(III)((X)-L)$(hfac)_3$] (X = *P*, *M*; L = 3-(2-pyridyl)-4-aza[6]-helicene; hfac = 1,1,1,5,5,5-hexafluoroacetylacetonate) (Scheme 36c) were examined in the near-infrared spectral window. Irradiating these chiral complexes

 This journal is © The Royal Society of Chemistry 2025

Open Access Article. Published on 02 April 2025. Downloaded on 4/4/2026 1:46:32 AM.
This article is licensed under a Creative Commons Attribution-NonCommercial 3.0 Unported Licence.

Table 3 Photophysical properties of chiral Ln complexes with polydentate ligands

Ln complex	Transition	Wavelength (nm)	Dissymmetry factor (g_{lum})	PLQY	Ref.
[Tb*R*(+)BnMeH22IAM]	$^5D_4$ to $^7F_5$	543	+0.044 (methanol)	63.0	*J. Am. Chem. Soc.*, 2007, **129**, 77–83[76]
[Tb*S*(−)BnMeH22IAM]	$^5D_4$ to $^7F_5$	543	−0.048 (methanol)	—	*J. Am. Chem. Soc.*, 2007, **129**, 77–83[76]
[Eu*R*(+)BnMeH22IAM]	$^5D_0$ to $^7F_1$	596	+0.298 (methanol)	2.3	*J. Am. Chem. Soc.*, 2007, **129**, 77–83[76]
[Eu*S*(−)BnMeH22IAM]	$^5D_0$ to $^7F_1$	596	−0.294 (methanol)	—	*J. Am. Chem. Soc.*, 2007, **129**, 77–83[76]
[Dy*R*(+)BnMeH22IAM]	$^4F_{9/2}$ to $^6H_{11/2}$	669	+0.013 (methanol)	1.3	*J. Am. Chem. Soc.*, 2007, **129**, 77–83[76]
[Sm*R*(+)BnMeH22IAM]	$^5G_{5/2}$ to $^6H_{7/2}$	565	−0.027 (methanol)	0.8	*J. Am. Chem. Soc.*, 2007, **129**, 77–83[76]
[(H_8Binol)$_3$SmNa$_3$]	$^4G_{5/2}$ to $^6H_{5/2}$	576	0.31 (THF)	4	*Chem. Commun.*, 2020, **56**, 14813–14816[77]
[(H_8Binol)$_3$TbNa$_3$]	$^5D_4$ to $^7F_6$	490	0.21 (THF)	27	*Chem. Commun.*, 2020, **56**, 14813–14816[77]
[(H_8Binol)$_3$DyNa$_3$]	$^4F_{9/2}$ to $^6H_{15/2}$	477	0.18 (THF)	17	*Chem. Commun.*, 2020, **56**, 14813–14816[77]
[(Binol)$_3$ErNa$_3$]	$^4I_{13/2}$ to $^4I_{15/2}$	1540	0.47 (THF)	0.0058	*J. Am. Chem. Soc.*, 2022, **144**, 6148–6153[78]
[(Binol)$_3$YbNa$_3$]	$^2F_{5/2}$ to $^2F_{7/2}$	975	0.17 (THF)	0.17	*J. Am. Chem. Soc.*, 2022, **144**, 6148–6153[78]
[(Binol)$_3$NdNa$_3$]	$^4F_{3/2}$ to $^4I_{9/2}$	900	0.04 (THF)	0.093	*J. Am. Chem. Soc.*, 2022, **144**, 6148–6153[78]
[Tb(H_2)]	$^5D_4$ to $^7F_5$	543.6	−0.083 (saturated aqueous solutions in 0.1 M Tris buffer, pH 7.4)	57	*J. Am. Chem. Soc.*, 2007, **129**, 15468–15470[79]
[Eu(H_1)(H_2O)]	$^5D_0$ to $^7F_1$	594.2	−0.12 (saturated aqueous solutions in 0.1 M Tris buffer, pH 7.4)	7.7	*J. Am. Chem. Soc.*, 2007, **129**, 15468–15470[79]
[Eu((*R*)-BINAPO)(D-facam)$_3$]	$^5D_0$ to $^7F_1$	594	0.44 (acetone-d_6)	—	*Inorg. Chem.*, 2009, **48**(23), 11242–11250[80]
[Eu((*S*)-BINAPO)(D-facam)$_3$]	$^5D_0$ to $^7F_1$	595	0.34 (acetone-d_6)	—	*Inorg. Chem.*, 2009, **48**(23), 11242–11250[80]
[Eu(BIPHEPO)(D-facam)$_3$]	$^5D_0$ to $^7F_1$	597	0.24 (acetone-d_6)	—	*Inorg. Chem.*, 2009, **48**(23), 11242–11250[80]
[Eu(TPPO)$_2$(D-facam)$_3$]	$^5D_0$ to $^7F_1$	594	0.47 (acetone-d_6)	—	*Inorg. Chem.*, 2009, **48**(23), 11242–11250[80]
[Eu((*R*)-BINAPO)(hfa)$_3$]	$^5D_0$ to $^7F_1$	593	0.03 (acetone-d_6)	—	*Inorg. Chem.*, 2009, **48**(23), 11242–11250[80]
[Eu(hfa)$_3$((*R*)-bidp)]$_n$	$^5D_0$ to $^7F_1$	595	0.0133 (acetone)	76	*Inorg. Chem.*, 2017, **56**, 5741–5747[81]
[Eu(hfa)$_3$((*R*,*R*)-B2QPO)]	$^5D_0$ to $^7F_1$	—	−0.083 (CH_2Cl_2)	63	*Dalton Trans.*, 2020, **49**, 5352–5361[82]
[Eu(hfa)$_3$((*R*)-B3QPO)]	$^5D_0$ to $^7F_1$	—	0.012 (CH_2Cl_2)	70	*Dalton Trans.*, 2020, **49**, 5352–5361[82]
Eu(TTEA)((*R*)-BINAPO)	$^5D_0$ to $^7F_1$	—	0.072 ($CHCl_3$)	32.4	*Inorg. Chem.*, 2018, **57**, 8332–8337[83]
Eu(TTEA)((*S*)-BINAPO)	$^5D_0$ to $^7F_1$	—	−0.073 ($CHCl_3$)	32.8	*Inorg. Chem.*, 2018, **57**, 8332–8337[83]
Yb(TTA)$_3$iPrPyBox (*R*,*R*)	$^2F_{7/2}$ to $^2F_{5/2}$	—	−0.025 (CH_2Cl_2)	—	*Chem. Commun.*, 2019, **55**, 6607–6609[84]
Yb(TTA)$_3$iPrPyBox (*S*,*S*)	$^2F_{7/2}$ to $^2F_{5/2}$	—	+0.029 (CH_2Cl_2)	—	*Chem. Commun.*, 2019, **55**, 6607–6609[84]
Sm(HFA)$_3$(*R*)-iPr-PyBox	$^4G_{5/2}$ to $^6H_{5/2}$	560	0.05 (CH_2Cl_2)	—	*Dalton Trans.*, 2018, **47**, 7166–7177[85]
Sm(HFA)$_3$(*R*)-Ph-PyBox	$^4G_{5/2}$ to $^6H_{5/2}$	560	0.03 (CH_2Cl_2)	—	*Dalton Trans.*, 2018, **47**, 7166–7177[85]
Sm(TTA)$_3$(*R*)-iPr-PyBox	$^4G_{5/2}$ to $^6H_{5/2}$	560	0.08 (CH_2Cl_2)	—	*Dalton Trans.*, 2018, **47**, 7166–7177[85]
Sm(TTA)$_3$(*R*)-Ph-PyBox	$^4G_{5/2}$ to $^6H_{5/2}$	560	0.03 (CH_2Cl_2)	—	*Dalton Trans.*, 2018, **47**, 7166–7177[85]
[(EuIII(*R*)-Ph-pybox)(HFA)$_3$]	$^5D_0$ to $^7F_1$	—	0.15 (CD_3CN)	34	*J. Am. Chem. Soc.*, 2011, **133**, 9892–9902[86]
[(EuIII(*R*)-i-Pr-pybox)(HFA)$_3$]	$^5D_0$ to $^7F_1$	—	−0.46 (CD_3CN)	41	*J. Am. Chem. Soc.*, 2011, **133**, 9892–9902[86]
[(EuIII(*R*)-Me-Ph-pybox) (HFA)$_3$]	$^5D_0$ to $^7F_1$	—	−0.35 (CD_3CN)	39	*J. Am. Chem. Soc.*, 2011, **133**, 9892–9902[86]
P3 + L-proline	$^5D_0$ to $^7F_1$	596	+0.41 (DMSO and H_2O) (v/v, 1.0%)	—	*Chem. Commun.*, 2013, **49**, 5772–5774[87]
P3 + D-proline	$^5D_0$ to $^7F_1$	596	−0.42 (DMSO and H_2O) (v/v, 1.0%)	—	*Chem. Commun.*, 2013, **49**, 5772–5774[87]
[EuL(tta)$_2$(H_2O)]CF_3SO_3	$^5D_0$ to $^7F_1$	590	0.202 (methanol)	52	*Inorg. Chem.*, 2018, **57**, 10257–10264[88]
1*S*	$^5D_0$ to $^7F_1$	593	0.013 (CH_2Cl_2)	—	*J. Mol. Struct.*, 2025, **1321**, 139780[89]
2*S*	$^5D_0$ to $^7F_1$	593	0.044 (CH_2Cl_2)	—	*J. Mol. Struct.*, 2025, **1321**, 139780[89]
3*S*	$^5D_0$ to $^7F_1$	593	0.065 (CH_2Cl_2)	—	*J. Mol. Struct.*, 2025, **1321**, 139780[89]
[(*R*-F_{12} Binol)$_3$Er][K]$_3$	—	1526	0.17 (THF)	3.5	*J. Am. Chem. Soc.*, 2024, **146**, 7097–7104[90]
(*S*,*S*)-[YbL]Cl	—	984	0.024 (H_2O)	—	*New J. Chem.*, 2024, **48**, 9627–9636[91]
(*R*,*R*)-[YbL]Cl	—	984	−0.017 (H_2O)	—	*New J. Chem.*, 2024, **48**, 9627–9636[91]
[Eu(hfa)$_3$(*S*-Bn-pybox)]	$^5D_0$ to $^7F_1$	—	0.366 (CH_2Cl_2)	41.4	*J. Mater. Chem. C*, 2024, **12**, 5097–5107[92]
[(sphenol)$_3$ErNa$_3$(thf)$_6$]	—	1540	0.77 (THF)	—	*Inorg. Chem.*, 2024, **63**, 7378–7385[15]
9*S*	$^5D_0$ to $^7F_2$	615	−0.3 (CH_3CN)	—	*Adv. Sci.*, 2024, **11**, 2307448[93]
10*R*	$^5D_0$ to $^7F_2$	615	0.3 (CH_3CN)	—	*Adv. Sci.*, 2024, **11**, 2307448[93]
R/*S*-Eu–Ph_3PO	$^5D_0$ to $^7F_1$	—	0.110 (methanol)	—	*Inorg. Chem. Front.*, 2024, **11**, 2039–2048[94]
[Eu(tta)$_3$(6 M)]	$^5D_0$ to $^7F_1$	—	-3×10^{-3} (CH_2Cl_2)	32	*Eur. J. Inorg. Chem.*, 2022, e202200010[95]
[Eu-(tta)$_3$(6*P*)]	$^5D_0$ to $^7F_1$	—	3×10^{-3} (CH_2Cl_2)	—	*Eur. J. Inorg. Chem.*, 2022, e202200010[95]
[(Spinol)$_3$TbNa$_3$(thf)$_6$]	$^5D_4$ to $^7F_5$	545	0.53 (THF)	84.6	*J. Am. Chem. Soc.*, 2022, **144**, 22421–22425[96]

Open Access Article. Published on 02 April 2025. Downloaded on 4/4/2026 1:46:32 AM.
This article is licensed under a Creative Commons Attribution-NonCommercial 3.0 Unported Licence.

Table 3 (*continued*)

Ln complex	Transition	Wavelength (nm)	Dissymmetry factor (g_{lum})	PLQY	Ref.
$[(Spinol)_3SmNa_3(thf)_6]$	$^4G_{5/2}$ to $^6H_{7/2}$	610	0.50 (THF)	2.8	*J. Am. Chem. Soc.*, 2022, **144**, 22421–22425[96]
Yb-*R*-1	—	980	0.077 (solid atate)	1.26	*Inorg. Chem.*, 2023, **62**, 4351–4360[97]
Yb-*R*-2	—	980	0.018 (solid state)	0.48	*Inorg. Chem.*, 2023, **62**, 4351–4360[97]
$CsEr(hfbc)_4$	—	1510	0.83 (THF)	—	*J. Mater. Chem. C*, 2023, **11**, 5290–5296[98]
$[TMG\text{-}H^+]_3Er(BINOLate)_3$	—	1545	0.29 (THF)	—	*J. Mater. Chem. C*, 2023, **11**, 5290–5296[98]
$Er(NTA)_3PhPyBox$	—	1523	0.06 (THF)	—	*J. Mater. Chem. C*, 2023, **11**, 5290–5296[98]

with unpolarized light in a magnetic field results in a significant magneto-chiral dichroism signal. This indicates the electronic transition of Yb(III) from $^2F_{7/2}$ to $^2F_{5/2}$. The low-temperature absorption and magneto-chiral dichroism spectra show a fine structure caused by crystal field splitting and vibronic interaction.

Wu *et al.* synthesized two mononuclear Dy complexes, which exhibited significant magnetic properties and stability in air (1 and 2, Scheme 37, left).[101] These complexes were synthesized using bulky equatorial macrocycles to prevent dimerization. The CD spectra of the 1 and 2 complexes are depicted in Scheme 37 (right), which confirms the mirror image relationship between the two enantiomers. These complexes show typical zero-field single-molecule magnet behavior, characterized by slow magnetic relaxation at low temperatures. They conducted temperature-dependent magnetic susceptibility measurements, revealing weak ferromagnetic intermolecular interactions and significant crystal field effects at the Dy(III) ion. They identified the Orbach and Raman processes as predominant magnetic relaxation pathways. Single-crystal X-ray diffraction analysis show that both complexes crystallize in a chiral space group ($P2_1$). The Dy(III) ion was found in an $N_6F_2O_1$ environment with a hula-hoop geometry.

The same group also synthesized Dy(III) based macrocyclic complexes with single-molecule magnet properties (*RRRR*-Dy-$D_{6h}F_{12}$ (1) and *SSSS*-Dy-$D_{6h}F_{12}$ (2), Scheme 38).[102] The synthesized complexes achieve a record anisotropy barrier exceeding 1800 K and a relaxation time of nearly 2500 s at 2.0 K. These Dy(III) based complexes exhibit axiality in their ground Kramer's doublet. This allows for open hysteresis loops up to 20 K in magnetically diluted samples. Both complexes crystallize in the polar space group *C*2 with D_{6h} symmetry and exhibit a decomposition temperature above 250 °C. Introducing fluorinated substituents enhances the magnetic anisotropy and stability of the complexes.

Liu *et al.* designed and synthesized three chiral binuclear Eu(III) complexes coordinated with different chiral Schiff base ligands (1-*R*/1-*S*, 2-*R*/2-*S* and 3-*R*/3-*S*, Scheme 39).[89] CPL is significantly enhanced through structural modification of ligands in chiral binuclear Eu(III) complexes. There is a five-fold increase in the luminescence dissymmetry factor based on the polarity of substituents at the chiral carbon sites of the ligands (Table 3). The synthesized Eu(III) complexes could recognize Co(II) ions and be applied in anti-counterfeiting and luminescence sensors. The steric hindrance and electronic effects of the substituents on the ligands could change the local symmetries of the Eu(III) centers. The transition from methyl to phenyl substituents increase the electron-withdrawing effects, further enhancing CPL.

Adewuyi and Ung synthesized two chiral erbium Shibasaki-type complexes, $[(R/S\text{-}F_{12}\ Binol)_3Er][M]_3$, where M = Li and K (Scheme 40).[90] They resolved the racemic mixture of F_{12}Binol ligand and coordinated it to erbium salts. The highest quantum yield of the synthesized complex is 11%. The CPL brightness values reached 317 M^{-1} cm^{-1} due to the total fluorination of the ligand, which mitigates nonradiative quenching from C sp^2-H vibrations. The developed complexes exhibit distinct chiroptical properties. The $[(R\text{-}F_{12}\ Binol)_3Er][K]_3$ complexes have a CPL signal between 1470 and 1520 nm and the strongest g_{lum} value

This journal is © The Royal Society of Chemistry 2025

Open Access Article. Published on 02 April 2025. Downloaded on 4/4/2026 1:46:32 AM.
This article is licensed under a Creative Commons Attribution-NonCommercial 3.0 Unported Licence.

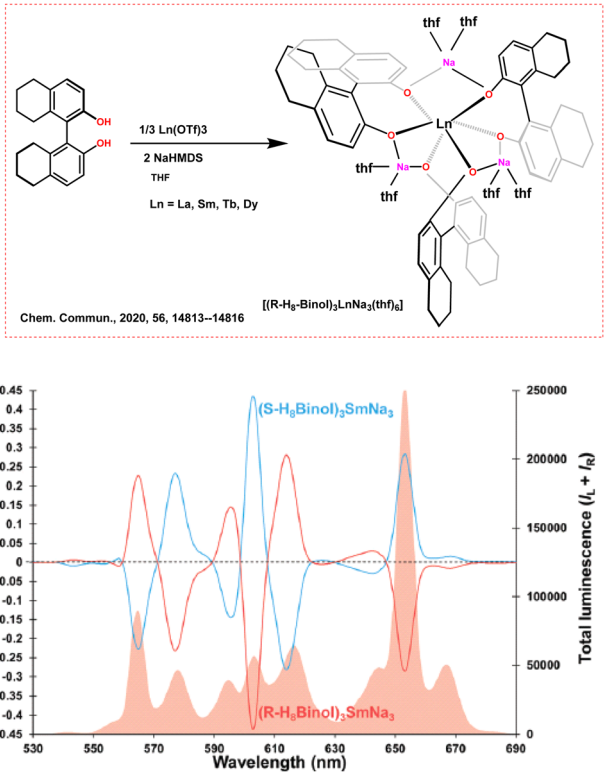

Scheme 27 (Above) Chemical structures of the ligands and Ln complexes ([(*R*/*S*-H_8-Binol)$_3$LnNa$_3$(thf)$_6$]).[77] (Below) Normalized CPL spectra of [(*R*-H_8-Binol)$_3$SmNa$_3$] (red) and [(*S*-H_8-BINOL)$_3$SmNa$_3$] (blue) in tetrahydrofuran solutions at room temperature. Reproduced from ref. 77 with permission from the Royal Society of Chemistry, copyright [2020].[77]

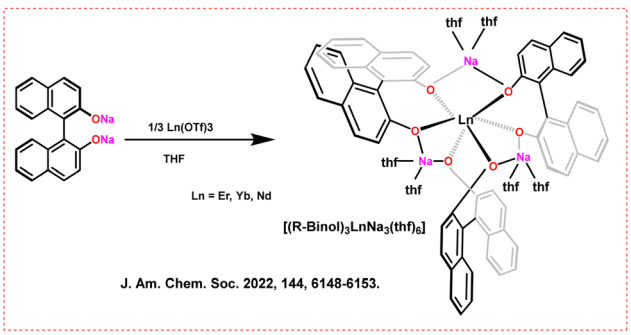

Scheme 28 Chemical structures of ligands and Ln complexes ([(*R*/*S*-Binol)$_3$ErNa$_3$]).[78]

of up to 0.17 (Table 3). They measured the CPL using an Olis NIR CPL Solo instrument.

Mizzoni *et al.* synthesized two enantiomeric complexes, (*R*,*R*)/(*S*,*S*)-[YbL]Cl (Scheme 41, left).[91] The ligand L is a conjugated chromophoric ligand, and the complexes were characterized in polar protic solvents. The Yb(III) complex emits at ~980 nm and is efficiently sensitized by the excitation of the picolinate antenna in the UV region around 330 nm. This indicates a strong energy transfer between the ligand and the metal ion. The complexes exhibit CPL (on a homemade apparatus) with g_{lum} values of |0.02| at 984 nm and |0.04| at 1021 nm. The CPL spectra in water and methanol are represented in Scheme 41 (right). The strong thermodynamic stability of the YbL species make it dominant at a physiological pH of 7.4. DFT calculations show that the *cis-O,O-N,N* isomer of the Yb(III) complex is the most predominant in aqueous solutions. Two-photon absorption in the NIR region could trigger Yb(III) luminescence.

Diogenis *et al.* developed a set of [Eu(hfa)$_3$(chiral)] complexes, where chiral = *S*-Bn-pybox, *S*-Ph-pyox, and (*R*)-Cl-(*S*)-Phpzox (Scheme 42, above).[92] This work presents significant findings regarding enhancing CPL brightness in Eu(III) β-diketone complexes with chiral auxiliary ligands. They analyzed how the dissymmetry factor (g_{lum}), CPL brightness, and overall emission quantum yield can be fine-tuned by varying the electronic structure and symmetry of the Eu(III) coordination polyhedron through opto-structural correlations of these complexes. The [Eu(hfa)$_3$-(*S*-Bn-pybox)] complex exhibits the highest CPL brightness at 465 M^{-1} cm^{-1} for the $^5D_0$–$^7F_2$ transition in dichloromethane (Scheme 42, below). The same complex also demonstrates a significant g_{lum} of 0.36 for the $^5D_0$–$^7F_1$ transition (Table 3). The overall emission quantum yield for [Eu(hfa)$_3$(*S*-Bn-pybox)] is 41.4%, which is attributed to the low local microsymmetry of Eu(III). They analyzed the bright CPL resulting from a combination of high emission quantum yield and a large branching ratio of the $^5D_0$–$^7F_2$ transition.

Sickinger *et al.* synthesized chiral Yb(III) complexes [Yb(*S*,*S*/*R*,*R*-L^{NHex2}$_3$(OTf)$_3$)] (Scheme 43, above) having a three-fold symmetry.[103] Single crystal structures reveal that both enantiomers crystallize in the orthorhombic $P2_12_12_1$ space group. The Yb(III) ion was coordinated by three ligands, which result in clockwise and anti-clockwise chirality based on the ligands' configurations. CPL spectra of the developed Yb(III) complexes were measured using a dual near-infrared CPL spectroscopy setup (on a homemade apparatus) across a wide temperature range from room temperature to 4 K. Decreasing the temperature to 77 K results in a narrowing of the emission bands. It also leads to a reduction in the contribution of hot bands. The CPL and ECD show that the g_{lum} is temperature-dependent (Scheme 43, below). CPL spectra are influenced by the thermal population of excited states, which varies with temperature.

Schnable and Ung synthesized two new CPL-active Ln complexes based on sphenol that emits in the NIR region ([(sphenol)$_3$LnNa$_3$(thf)$_6$ Ln = Y, Er and Yb] Scheme 44a).[15] Including a quaternary carbon in the sphenol ligand significantly enhances the CPL strength of the synthesized complexes. The g_{lum} for the [(sphenol)$_3$ErNa$_3$(thf)$_6$] complex reaches 0.77 (Table 3). The rigid structure of the sphenol ligand contributes to the high dissymmetry factors for Shibasaki-type complexes. However, chiroptical measurements are highly sensitive to variations in instrumental parameters. Therefore, standardized measurement techniques can improve the comparison of different CPL emitters (CPL was measured using an Olis NIR CPL Solo).

Caffrey *et al.* synthesized chiral pyridyl-diamide (pda) ligands (1–4, Scheme 44b).[93] These ligands were derived from chelidamic acid and 1-(1-naphthyl)-ethylamine through peptide

Open Access Article. Published on 02 April 2025. Downloaded on 4/4/2026 1:46:32 AM.
This article is licensed under a Creative Commons Attribution-NonCommercial 3.0 Unported Licence.

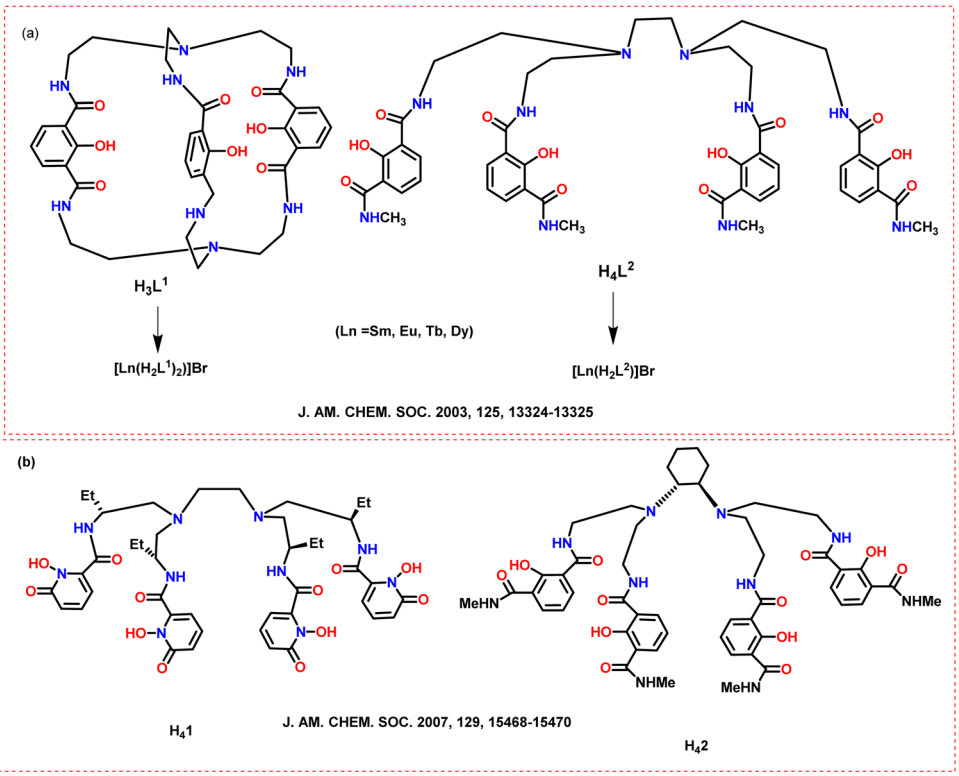

Scheme 29 Molecular structures of some polydentate ligands. (a) H_3L^1 and H_4L^2;[99] (b) H_41 and H_42.[79]

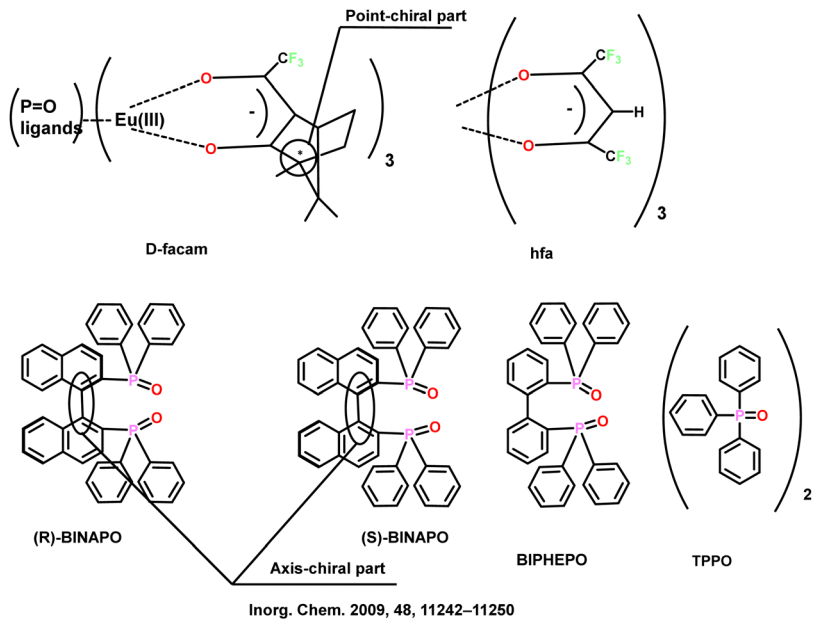

Scheme 30 Molecular structures of some polydentate ligands.[80]

coupling reactions. The ligands were reacted with $Eu(CF_3SO_3)_3$ to form 1 : 3 (Eu : L) complexes (5*S*–12*R*). The ligand chirality is preserved from the solution to the solid state. The chirality of the ligands significantly influences the luminescence characteristics of the complex. The complexes exhibit high g_{lum} (CPL measured using a photoelastic modulator spectrometer) due to the ligand chirality and the helical arrangement around the Eu(III) center.

Sickinger *et al.* synthesized enantiomers of erbium(III) complexes ([Er(*S*,*S*)/(*R*,*R*)-$(L)_3$][$(OTf)_3$), (Scheme 45, left) that exhibit

This journal is © The Royal Society of Chemistry 2025

Open Access Article. Published on 02 April 2025. Downloaded on 4/4/2026 1:46:32 AM.
This article is licensed under a Creative Commons Attribution-NonCommercial 3.0 Unported Licence.

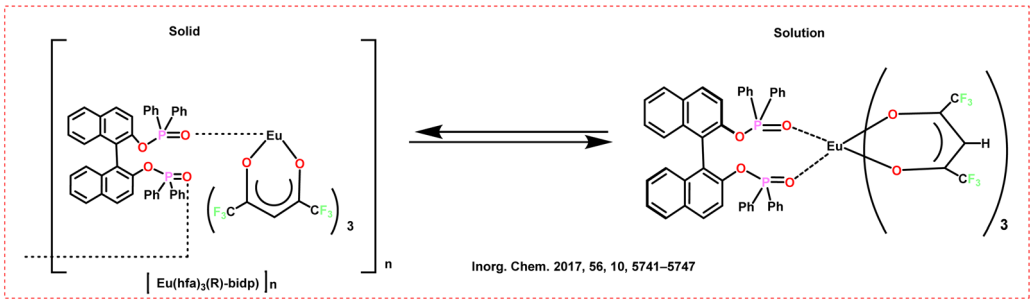

Scheme 31 Conceptual transformation of the Eu(III) coordination polymer with the chiral (*R*)-bidp ligands.[81]

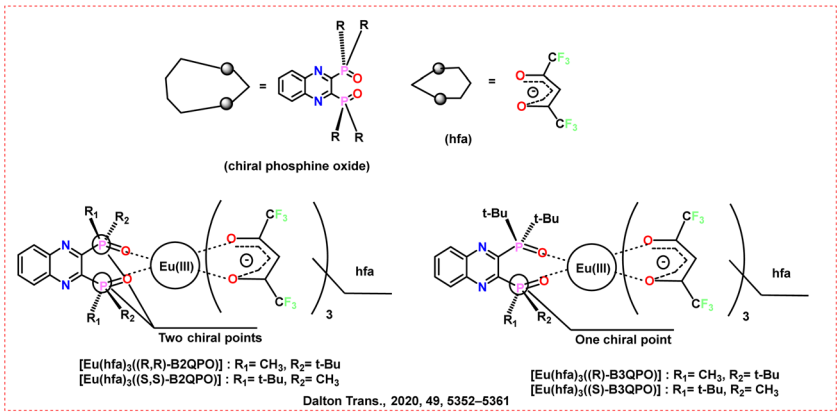

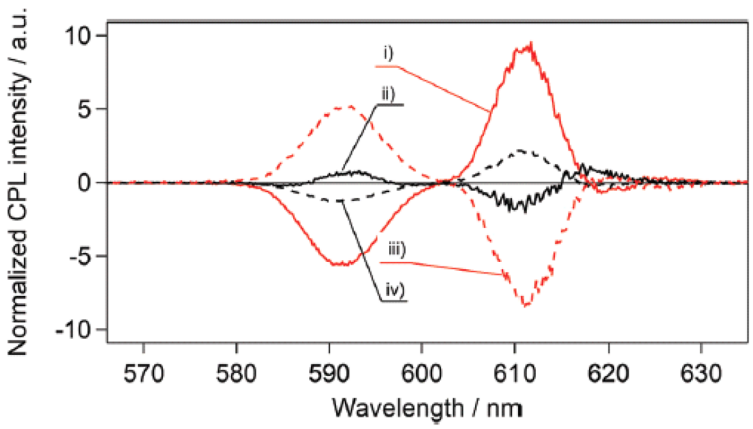

Scheme 32 (Above) Chemical structures of the ligands and Ln complexes [Eu(hfa)$_3$((*R*,*R*)/(*S*,*S*)-B2QPO)] and [Eu(hfa)$_3$((*R*)/(*S*)-B3QPO)].[82] (Below) CPL spectra of [Eu(hfa)$_3$((*R*,*R*)-B2QPO)] ((i), red solid line), [Eu(hfa)$_3$((*R*)-B3QPO)] ((ii), black solid line), [Eu(hfa)$_3$((*S*,*S*)-B2QPO)] ((iii), red dashed line) and [Eu(hfa)$_3$((*S*)-B3QPO)] ((iv), black dashed line) in dichloromethane. Reproduced from ref. 82 with permission from the Royal Society of Chemistry, copyright [2020].[82]

distinct clockwise and anti-clockwise helicity.[104] They analyzed these complexes using NMR and FTIR spectroscopies, and mass spectrometry. The crystal structure of the $[Er(R,R\text{-L})_3]^{3+}$ complex has a coordination environment of N_3O_6 around the Er(III) center. The complexes have a broad absorption band centered around 455 nm. This band is attributed to intra-ligand charge transfer transitions. There is no distinct absorption band for the free ligand, even at low concentrations. This confirms the stability of the complex. The characteristic erbium transition at 1520 nm is observed upon excitation, with a broad spectrum showing multiple bands. The reduced slit aperture improves CPL spectral resolution (measured on a homemade apparatus) but decreases signal intensity (Scheme 45, right). The different experimental bandwidths impact the dissymmetry factors. The maximum g_{lum} value of 0.66 is recorded at the lowest experimental bandwidths.

Tang *et al.* synthesized *R*/*S*-Ln complexes through a [2+2] imine condensation reaction (*R*/*S*-Ln and *R*/*S*-Eu–Ph_3PO,

Open Access Article. Published on 02 April 2025. Downloaded on 4/4/2026 1:46:32 AM.
This article is licensed under a Creative Commons Attribution-NonCommercial 3.0 Unported Licence.

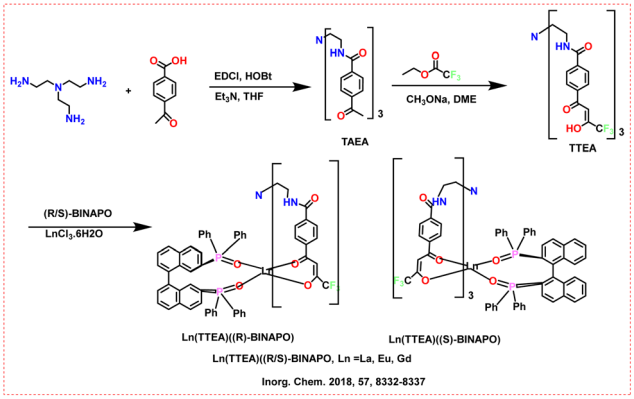

Scheme 33 Chemical structures of the ligands and Ln complexes.[83]

Ln = Eu, Gd, Scheme 46, above).[94] The developed *R*/*S*-Eu and *R*/*S*-Eu–Ph_3PO exhibit efficient CPL (recorded on a Jasco CPL-300 spectrometer) with maximum g_{lum} for these compounds of 0.098 and 0.110, respectively. The CD spectra of *R*/*S*-Eu is depicted in Scheme 46 (below). The *R*/*S*-Eu–Ph_3PO complex shows stronger emission intensity and a longer luminescence lifetime than *R*/*S*-Eu. This difference is attributed to the lower vibrational coordination structures surrounding the Eu(III) ion in the Ph_3PO complex. *R*/*S*-Gd reached high relaxivity values up to 35.04 and 34.09 mM^{-1} s^{-1} for the *R* and *S* enantiomers, respectively. Moreover, Gd(III)-chelates have low toxicity and are effective for MRI in A549 cells.

Liu *et al.* synthesized the chiral double-decker Dy(III) macrocycles with fluoride ions as their sole axial ligands (1/2, Scheme 47, left).[105] The macrocycles exhibit strong intramolecular ferromagnetic coupling. Both Dy(III) ions were coordinated with a hula-hoop coordination geometry with a C_{2v} symmetry. The developed Dy(III) macrocycles depict a two-step magnetization relaxation in a zero DC field. Moreover, this arrangement leads to different Dy–F distances for the two Dy(III) ions. The collinear arrangement of the magnetic anisotropy axes contribute to the stability of the macrocycles. The CD spectra of these two enantiomers are mirror images of each other (Scheme 47, right).

Helicenes are known for their intrinsic helical chirality and exceptional chiroptical properties. making them valuable in chiral materials research. Abhervé *et al.* synthesized the enantiopure versions of tridentate bis(pyrazolyl)pyridine (bpp) ligands with a helicene unit (6*M*/6*P*, Scheme 48a).[95] They characterized these ligands through their structural and chiroptical properties. The synthesized ligands were complexed to Eu(III) and Yb(III) ions to form emissive complexes ($Ln(tta)_3$6*M* or 6*P*). The bpp-helicene ligands could efficiently sensitize the luminescence of the Eu(III) center through energy transfer from the ligand's first triplet state. The developed Eu(III) and Yb(III) complexes could achieve a quantum yield of 32% for the Eu complex, indicating effective energy transfer. The chiral Eu(III) complexes exhibit CPL (g_{lum} values in Table 3, CPL recorded on a home-made spectrofluoropolarimeter), despite the helicene's

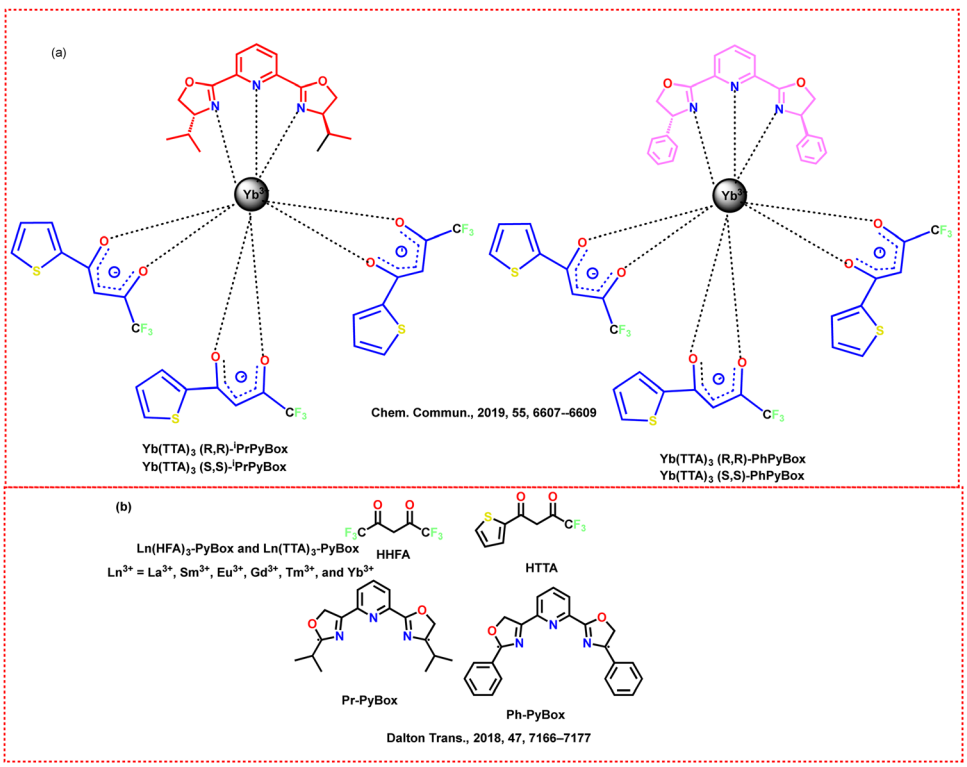

Scheme 34 Molecular structures of some polydentate ligands and Ln complexes. (a) $Yb(TTA)_3$iPrPyBox and $Yb(TTA)_3$PhPyBox.[84] (b) $Ln(HFA)_3$-PyBox/iPrPyBox and $Ln(TTA)_3$-PyBox/iPrPyBox.[85]

 This journal is © The Royal Society of Chemistry 2025

Open Access Article. Published on 02 April 2025. Downloaded on 4/4/2026 1:46:32 AM.
This article is licensed under a Creative Commons Attribution-NonCommercial 3.0 Unported Licence.

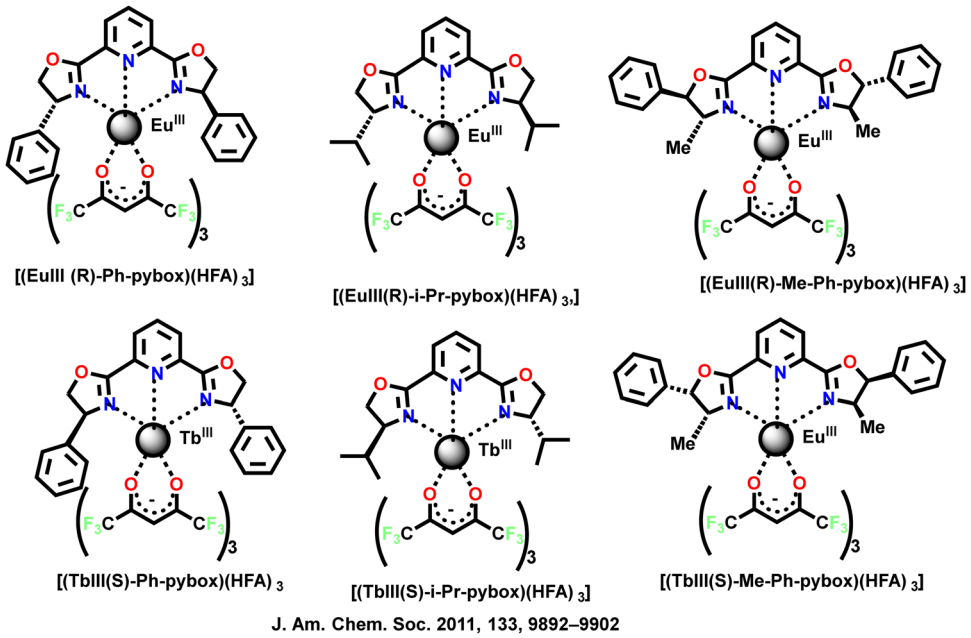

Scheme 35 Molecular structures of some polydentate ligands.[86]

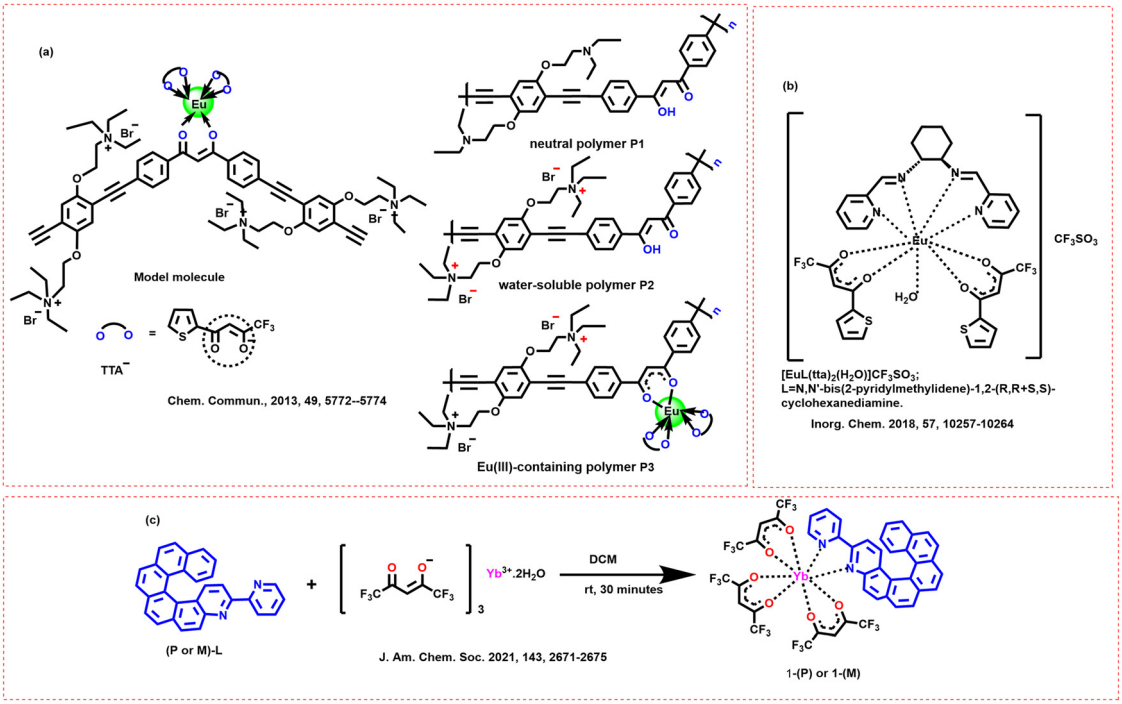

Scheme 36 Molecular structures of some polydentate ligands and Ln complexes (a) P1, P2 and P3;[87] (b) $[EuL(tta)_2(H_2O)]$;[88] (c) $[Yb(III)((X)\text{-}L)(hfac)_3]$ (X = *P*, *M*); L = 3-(2-pyridyl)-4-aza[6]-helicene.[100]

remote position relative to the coordination pocket of the ligand.

Willis *et al.* synthesized analogs of Shibasaki's complexes supported by enantiopure Spinol ($[(R\text{-Spinol})_3LnNa_3(thf)_6]$; Ln = Sm, Eu, Tb, Dy) (Scheme 48b).[96] The developed complexes could achieve a CPL (recorded on an Olis CPL Solo spectrofluorometer) with g_{lum} reaching up to 0.53 for Tb and Dy complexes and 0.50 for Sm complexes (Table 3). They could also achieve NIR emission with Sm complexes at around 980 nm. The Tb complex achieves a CPL brightness of 3760 M^{-1} cm^{-1}, which can be attributed to efficient sensitization of the complex. The developed complexes emit high quantum yields with values of

Open Access Article. Published on 02 April 2025. Downloaded on 4/4/2026 1:46:32 AM.
This article is licensed under a Creative Commons Attribution-NonCommercial 3.0 Unported Licence.

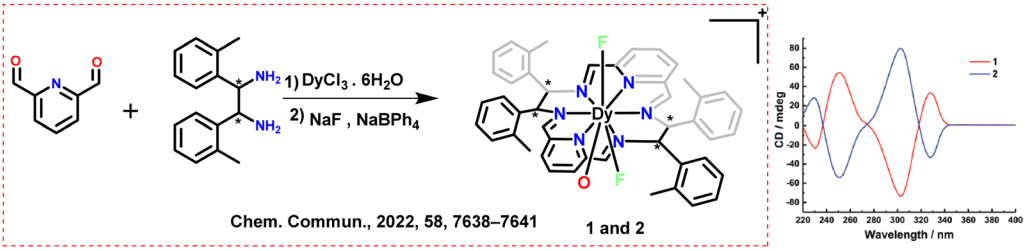

Scheme 37 (Left) Chemical structures of the ligands and Ln complexes (1 and 2).[101] (Right) CD spectra of 1 (red) and 2 (blue) in MeOH. Reproduced from ref. 101 with permission from the Royal Society of Chemistry, copyright [2022].[101]

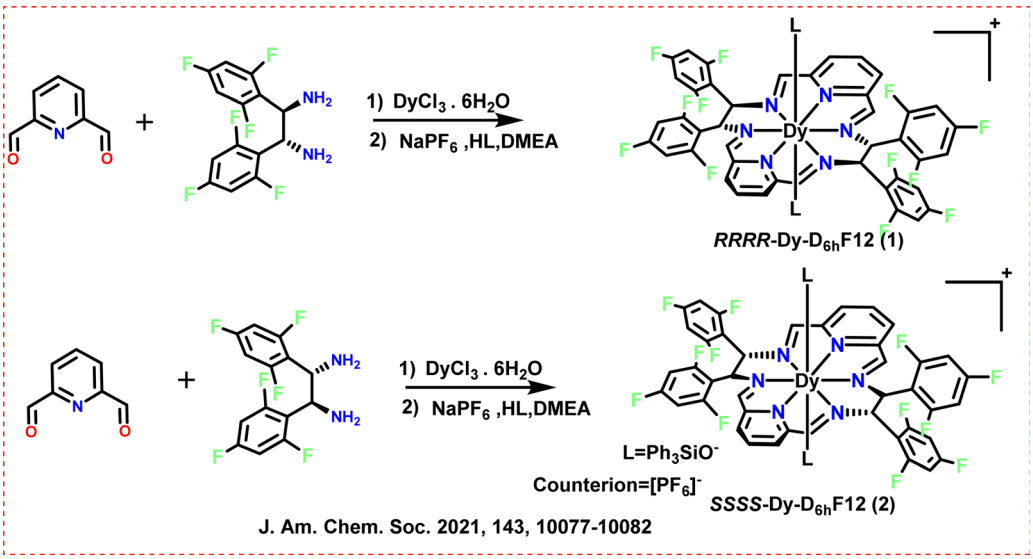

Scheme 38 Chemical structures of the ligands and Ln complexes (*RRRR*-Dy-$D_{6h}F_{12}$ (1) and *SSSS*-Dy-$D_{6h}F_{12}$ (2)).[102]

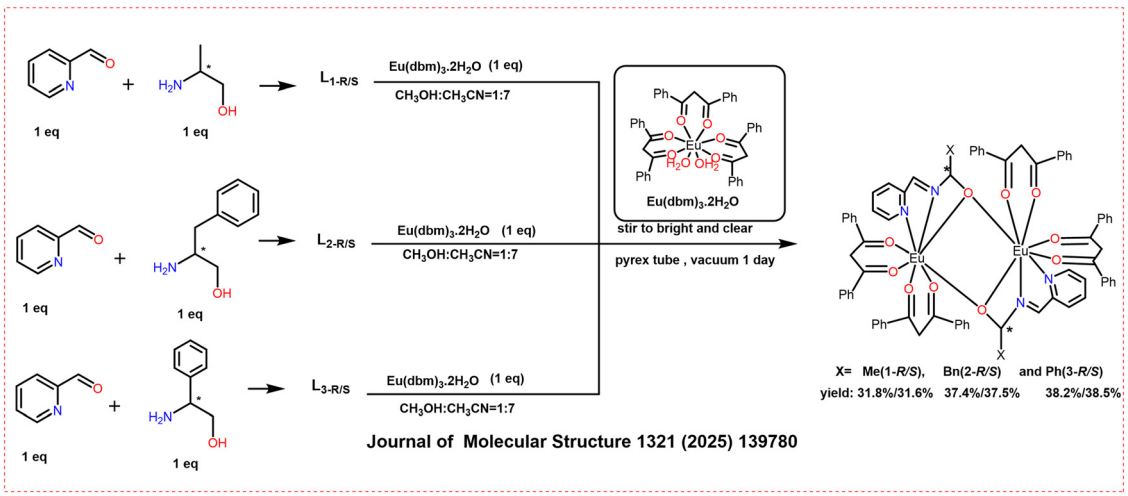

Scheme 39 Chemical structures of ligands and Ln complexes (1-*R*/1-*S*, 2-*R*/2-*S* and 3-*R*/3-*S*).[89]

84.6% for Tb and 15.5% for Dy. However, the Sm complex has a low quantum yield attributed to the nonradiative decay pathways. The complexes show long luminescence lifetimes (69.4 μs for Sm, 1180 μs for Tb, and 70.9 μs for Dy), indicating stable excited states.

 This journal is © The Royal Society of Chemistry 2025

Open Access Article. Published on 02 April 2025. Downloaded on 4/4/2026 1:46:32 AM.
This article is licensed under a Creative Commons Attribution-NonCommercial 3.0 Unported Licence.

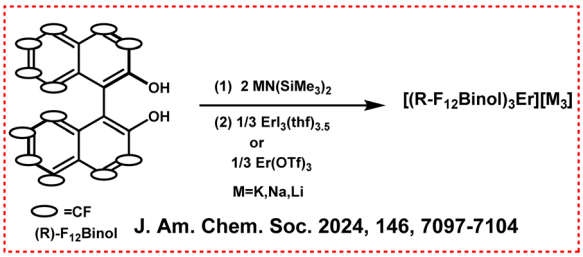

Scheme 40 Chemical structures of the ligands and Ln complexes [(*R*/*S*-F_{12} Binol)$_3$Er][M]$_3$.[90]

Li *et al.* explored the replacement of coordinated two water molecules in Yb(tta)$_3$(H_2O)$_2$ with enantiomerically pure bidentate and tridentate N-donor ligands.[97] This replacement in the sphere results in eight- and nine-coordinated Yb(III) enantiomeric pairs ((Yb-*R*-1/Yb-*S*-1) and (Yb-*R*-2/Yb-*S*-2) Scheme 48c). Yb-*R*-1 coordinated to ligand (^1L_R) has a high NIR photoluminescence quantum yield of 1.26% at room temperature. However, Yb-*R*-2, which uses a *C*2-symmetric tridentate ligand (^2L_R), shows a lower quantum yield of 0.48%. The emission decay lifetime for the $^2F_{5/2}$ to $^2F_{7/2}$ transition is 20 μs for Yb-*R*-1 and 8 μs for Yb-*R*-2 at room temperature. This suggests that Yb-*R*-1 has a more favorable emitting center due to its mononuclear structure. The g_{lum} for Yb-*R*-1 is 0.077, which is significantly higher than the value of Yb-*R*-2 (0.018) (CPL recorded on an Olis CPL Solo NIR) (Table 3). Yb-*R*-1 exhibits a stronger second-harmonic generation response (0.8 × KDP) than Yb-*R*-2 (0.1 × KDP). Yb(tta)$_3$(H_2O)$_2$ has a strong third-harmonic generation response (41 × α-SiO_2). However, replacing two coordinated water molecules in Yb(tta)$_3$(H_2O)$_2$ with enantiomerically pure bidentate and tridentate N-donor ligands results in a switch from THG to SHG in the chiral complexes.

Marydasan *et al.* synthesized a series of optically active heterobimetallic Eu(III) complexes with the formula M^+[Eu((+)-tfac)$_4$]$^-$, where M = Cs, Rb, K, Na (Scheme 49, left).[106] The synthesized complex M^+[Eu((+)-tfac)$_4$]$^-$, where M = Cs shows the highest inhibition rate of approximately 88% against *Staphylococcus aureus*. The other complexes exhibit 70–75% inhibition. The complexes display high CPL (on a Jasco CPL-300 instrument), with the Cs derivative showing a high g_{lum} value of approximately −0.29 for the $^5D_0$ to $^7F_1$ transition at 595 nm (Scheme 49, right). The luminescence intensity increases with the size of the alkali metal ion. The synthesized complexes could self-assemble into well-defined chiral nanostructures. Scanning electron microscopy (SEM) and transmission electron microscopy (TEM) reveal long wire-like structures with an average width of 200 nm and lengths of several micrometers.

Willis *et al.* synthesized Ln enantiomeric homo- and heteroleptic complexes emitting in the range of 1400 to 1600 nm (CsEr(hfbc)$_4$, [TMG-H$^+$]$_3$Er(BINOLate)$_3$, Er(NTA)$_3$iPr/PhPyBox) (Scheme 50, left).[98] Inexpensive optics were used to measure left and right CPL components with a custom-built instrument. The homoleptic complex CsEr(hfbc)$_4$ exhibits the highest g_{lum} value of 0.83 at 1510 nm. The heteroleptic complex [TMG-H$^+$]$_3$Er(BINOLate)$_3$ shows a g_{lum} value of 0.29 at 1545 nm (Table 3). The CsEr(hfbc)$_4$ complex displays a structured emission profile with four distinct maxima at 1477, 1509, 1530, and 1542 nm (Scheme 50, right). These CPL signals depict a mirror image behavior, highlighting the chiral nature of the emission. The Er(NTA)$_3$PhPyBox complex exhibits a narrow emission band with simple chiroptical features. However, the Er(NTA)$_3$iPrPyBox shows no measurable chiroptical activity.

3. Different types of CPL spectrometers

A CPL spectrofluoropolarimeter generally consists of a light source, quarter-wave plate, or photoelastic modulator (PEM), and linear polarizers, monochromators, and detectors. The PEM and a linear polarizer distinguish between left and right CPL. A monochromator is used to filter specific wavelengths and detectors such as photomultiplier tubes (PMT) amplify

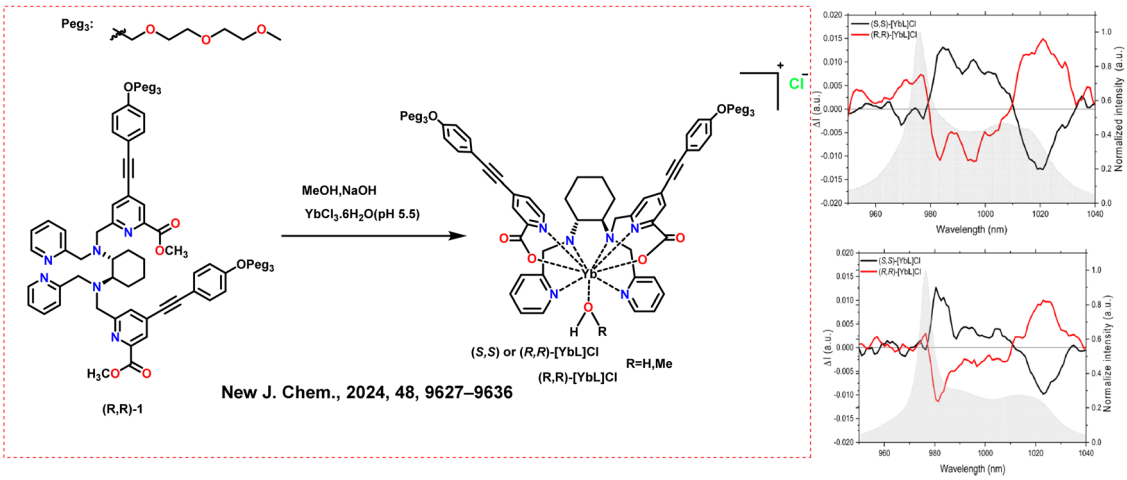

Scheme 41 (Left) Chemical structures of the ligands and Ln complexes (*R*,*R*)/(*S*,*S*)-[YbL]Cl.[91] (Right) CPL spectra of (*S*,*S*)-[YbL]Cl and (*R*,*R*)-[YbL]Cl complexes in water (up) and in methanol (bottom) emitting in the near-infrared region. Reproduced from ref. 91 with permission from the Royal Society of Chemistry, copyright [2024].[91]

Open Access Article. Published on 02 April 2025. Downloaded on 4/4/2026 1:46:32 AM.
This article is licensed under a Creative Commons Attribution-NonCommercial 3.0 Unported Licence.

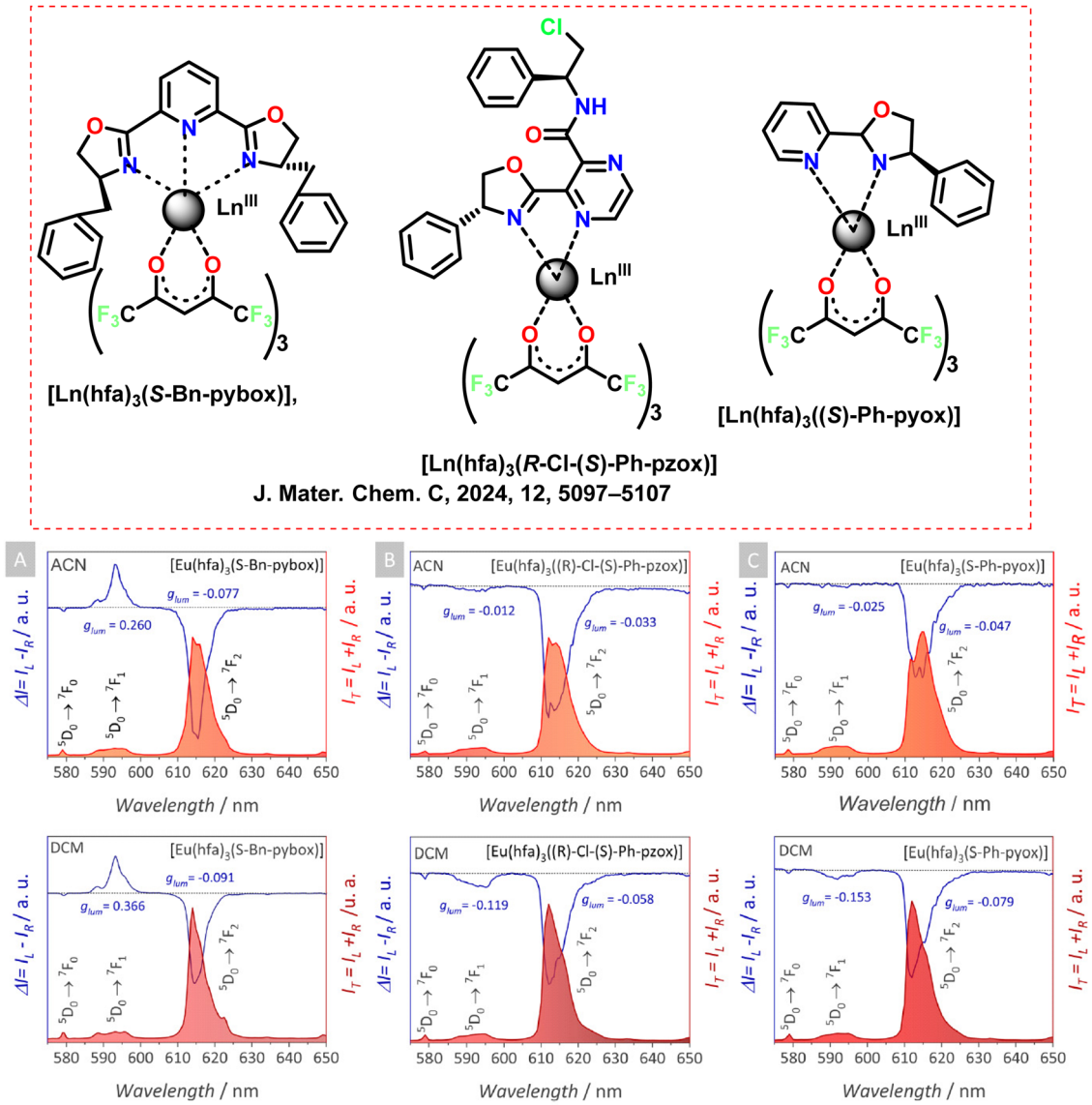

Scheme 42 (Above) Chemical structures of the ligands and Ln complexes [Eu(hfa)$_3$(chiral)]; chiral = *S*-Bn-pybox, *S*-Ph-pyox, and (*R*)-Cl-(*S*)-Phpzox, adapted from ref. 92. (Below) Total emission spectra (red area) and CPL spectra of (A) [Eu(hfa)$_3$(*S*-Bn-pybox)], (B) [Eu(hfa)$_3$((*R*)-Cl-(*S*)-Ph-pzox)], and (C) [Eu(hfa)$_3$(*S*-Ph-pyox)]. Reproduced from ref. 92 with permission from the Royal Society of Chemistry, copyright [2024].[92]

weak signals. The basic diagram is represented in Fig. 6a.[107] The CPL signal of compounds with large *g*-values can be measured by a cost-efficient quarter-waveplate. Kitzmann *et al.* have discussed the artifacts in CPL spectroscopy in detail[108] and we have briefly described below the different types of CPL spectrometers following their details.

A quarter-wave plate is oriented at ±45° with respect to a linear polarizer (Fig. 6b).[108] This quarter-wave plate causes a 90° phase retardance in the light that passes through it. It transforms LCP and RCP light into linearly polarized light with a plane of polarization at +45° and −45° relative to the fast axis of the optic.[108] The modified light goes through the linear polarizer, which filters the light. To measure both LCP and RCP, the quarter-wave plate is rotated by 90°. This allows the spectrometer to record two different emission spectra sequentially. The g_{lum} value is calculated using the LCP and RCP intensity. A quarter-wave plate generates orthogonal linear polarizations of LCP and RCP (Fig. 6b).[108] The linear polarizer filters the polarized light. The quarter-wave plate should be turned by 90° to measure the RCP and LCP. This method of measuring CPL has some drawbacks. For example, it can introduce artifacts if the quarter-wave plate is rotated manually. This method can also cause a delay between the two sequential measurements. This delay can cause changes in the sample or the light source, leading to inaccurate results. Moreover, this setup works well for strong CPL signals and can be difficult to measure weaker signals. However, the broadband quarter-wave plates can detect CPLs in broadband without scanning the emission wavelength.

A 50/50 beam splitter placed behind the quarter-wave plate can address the delay in measuring both signals (Fig. 6c).[108]

 This journal is © The Royal Society of Chemistry 2025

Open Access Article. Published on 02 April 2025. Downloaded on 4/4/2026 1:46:32 AM.
This article is licensed under a Creative Commons Attribution-NonCommercial 3.0 Unported Licence.

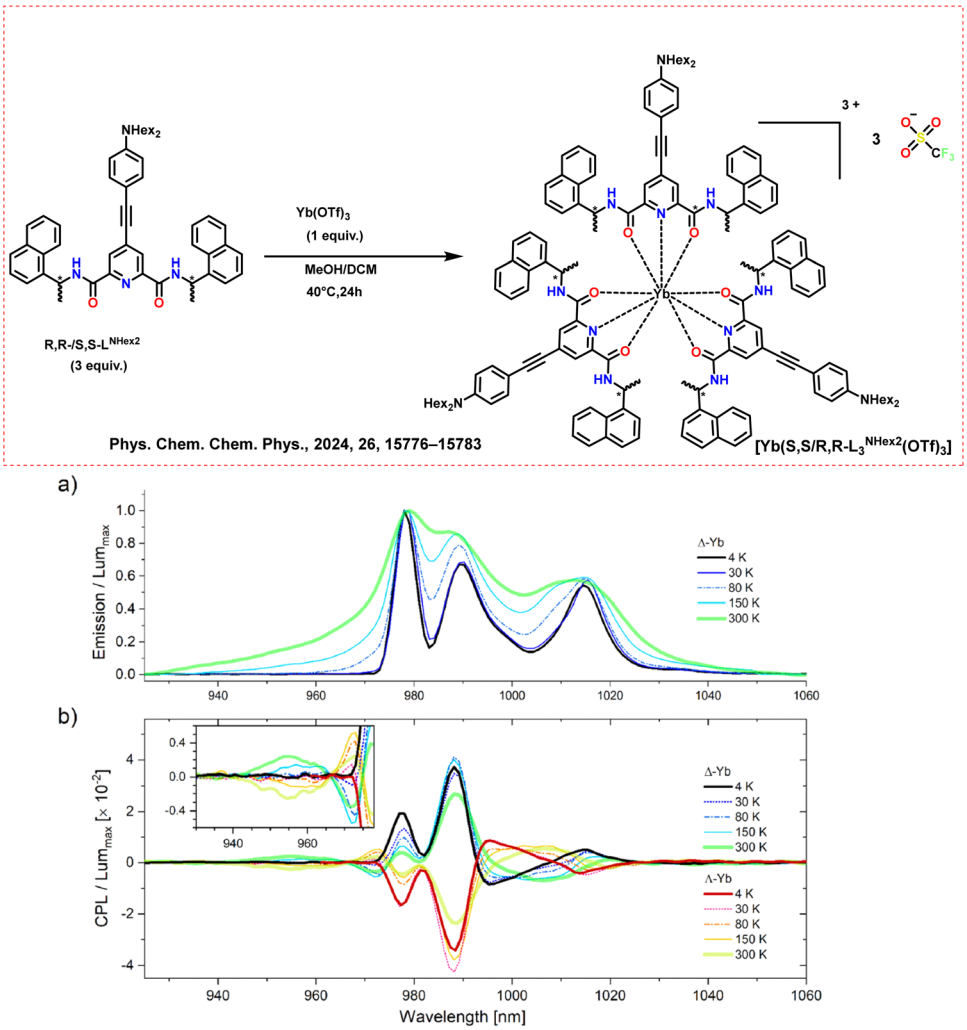

Scheme 43 (Above) Chemical structures of the ligands and Ln complexes [Yb(*S,S/R,R*-$L^{NHex2}{}_3(OTf)_3$)], adapted from ref. 103. (Below) Variable temperature spectra of the two Yb^{3+} complexes in PDMS at 4, 30, 80, 150 and 300 K. (a) Variable temperature-luminescence spectra for D-Yb. (b) Variable temperature-CPL spectra. Inset shows the enlarged region of hot bands. Reproduced from ref. 103 with permission from the Royal Society of Chemistry, copyright [2024].[103]

This setup allows for the simultaneous detection of RCP and LCP. LCP and RCP components can be separated using a 50/50 non-polarizing beam-splitter (Fig. 6c).[108] Two identical linear polarizers and detectors are kept on the orthogonal detection position. These detectors measure the L- and R CP simultaneously. However, minor differences in the sensitivities of the two detectors or the detection pathways and flaws in the quarter-wave plates can also cause errors in data processing.

Baguenard *et al.* recently revealed a more sensitive setup (Fig. 7a) to detect low CPL signals.[108,109] This configuration uses a polarizing beam splitter and directs the two linearly polarized components onto the same CCD camera or detectors *via* fiber optics. The wave plate is adjusted to −45° after spectra are obtained using the quarter-wave plate at 45°. Instead of using two separate detectors to measure the light, the new method sends both types of polarized light to the same camera. This setup can automatically adjust for issues like unequal light transmission and differences in wavelength, making the results more reliable. However, stray light requires a correction factor in the results, and the issues with linear polarization components in the emitted light must be addressed.

Another type of CPL measuring instrument relies on the photoelastic modulator (PEM) over most quarter-wave plate-based techniques (Fig. 7b).[108] This instrument is better as it resolves most of the limitations of other instruments described above. A PEM is a quarter-wave plate that alternately transforms LCP and RCP at a certain wavelength into 45° linearly polarized light. Its fast axis orientation oscillates between 0° and 90° at a resonance frequency.[108] The PEM works at one particular tunable wavelength at a time. This requires a PEM instrument for a full wavelength scan to capture an emission spectrum. It is also possible to detect small dissymmetry factors with the help

Open Access Article. Published on 02 April 2025. Downloaded on 4/4/2026 1:46:32 AM.
This article is licensed under a Creative Commons Attribution-NonCommercial 3.0 Unported Licence.

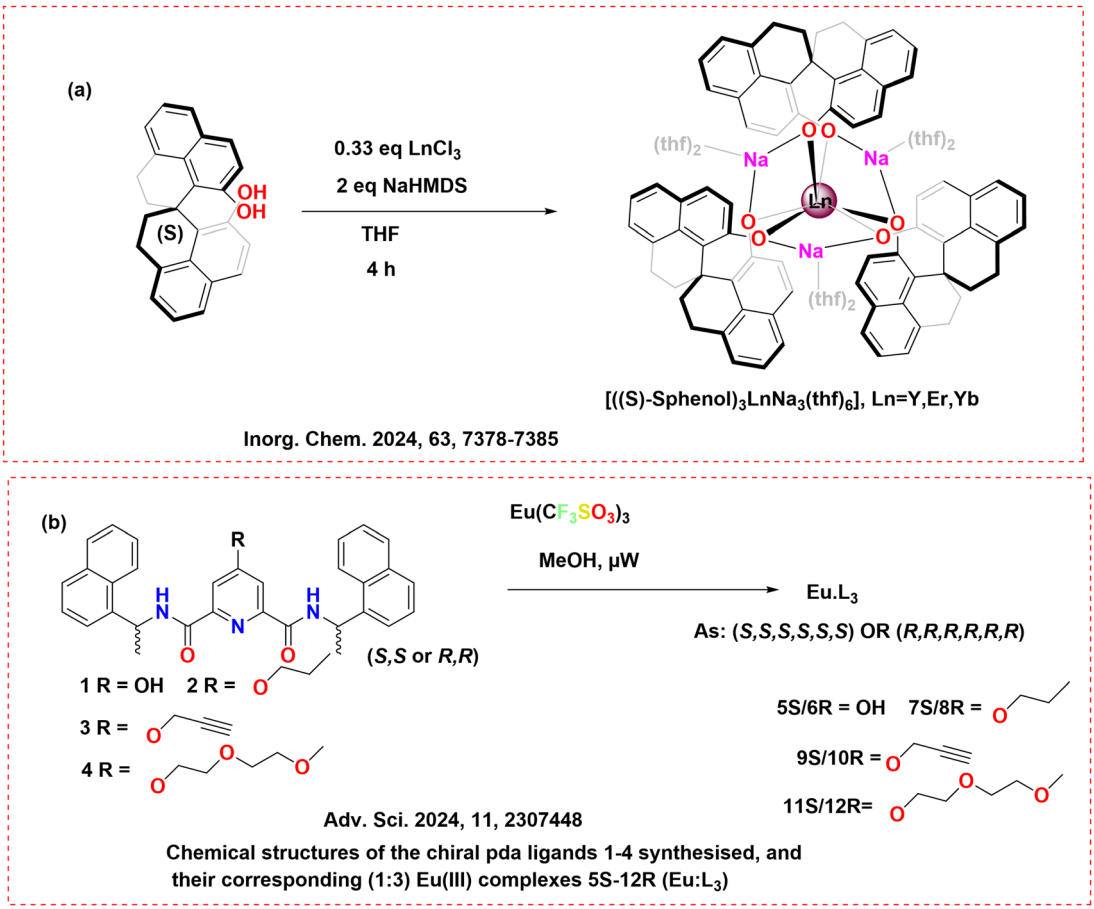

Scheme 44 Chemical structures of the ligands and Ln complexes (a) [(sphenol)$_3$LnNa$_3$(thf)$_6$ Ln = Y, Er and Yb], adapted from ref. 15 (b) (5*S*–12*R*), adapted from ref. 93.

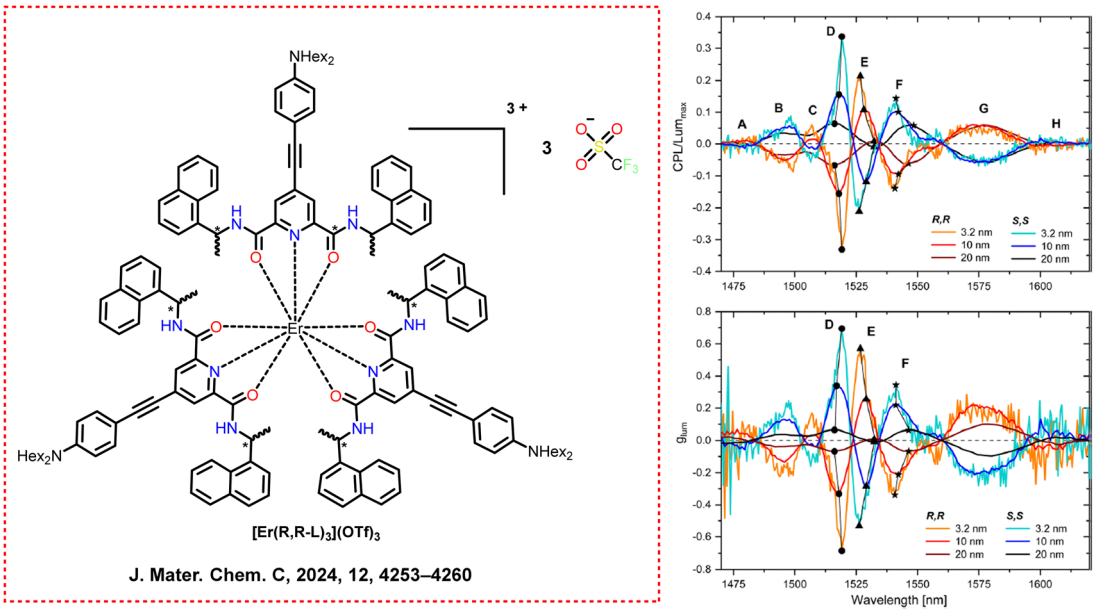

Scheme 45 (Left) Chemical structures of the ligands and Ln complexes [Er(*S*,*S*)/(*R*,*R*)(L)$_3$](OTf)$_3$, adapted from ref. 104. (Right) (Top) Merged CPL spectra for [Er(*S*,*S*-L)$_3$](OTf)$_3$ and [Er(*R*,*R*-L)$_3$](OTf)$_3$ measured at different experimental bandwidths. (Bottom) Resulting curves of the emission dissymmetry factor g_{lum} over the emission ranges. Reproduced from ref. 104 with permission from the Royal Society of Chemistry, copyright [2024].[104]

This journal is © The Royal Society of Chemistry 2025

Open Access Article. Published on 02 April 2025. Downloaded on 4/4/2026 1:46:32 AM.
This article is licensed under a Creative Commons Attribution-NonCommercial 3.0 Unported Licence.

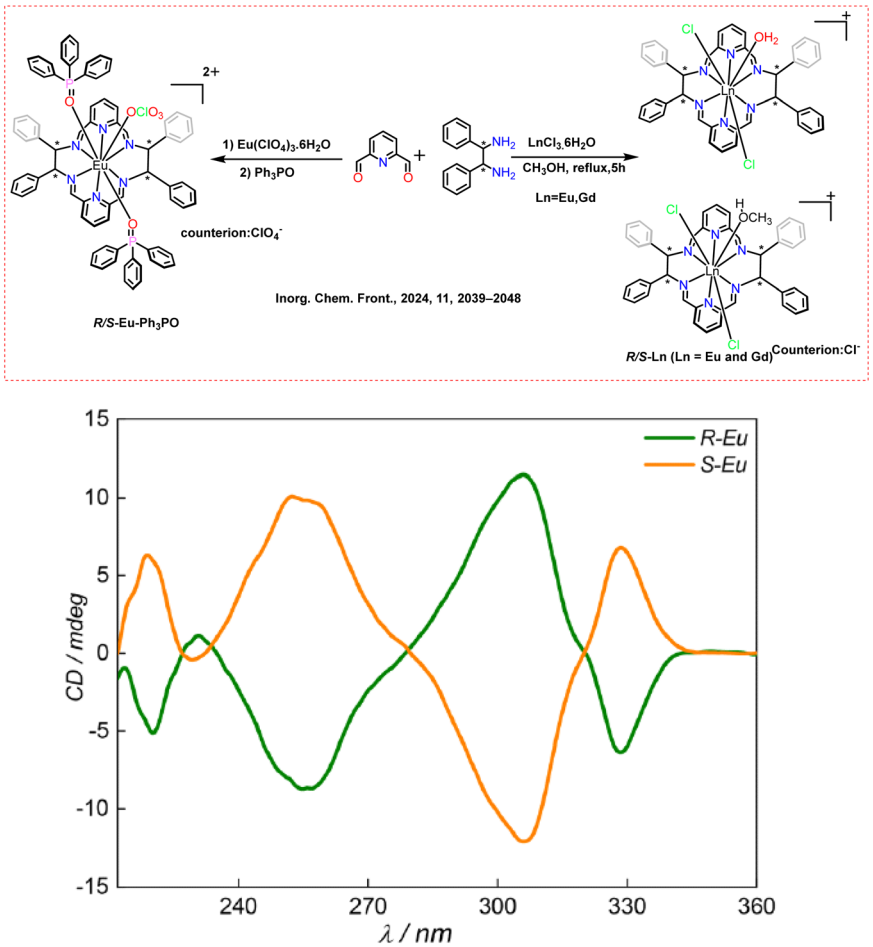

Scheme 46 (Above) Chemical structures of the ligands and Ln complexes (*R*/*S*-Ln and *R*/*S*-Eu-Ph_3PO, Ln = Eu, Gd), adapted from ref. 94. (Below) CD spectra of *R*/*S*-Eu in CH_3OH. Reproduced from ref. 94 with permission from the Royal Society of Chemistry, copyright [2024].[94]

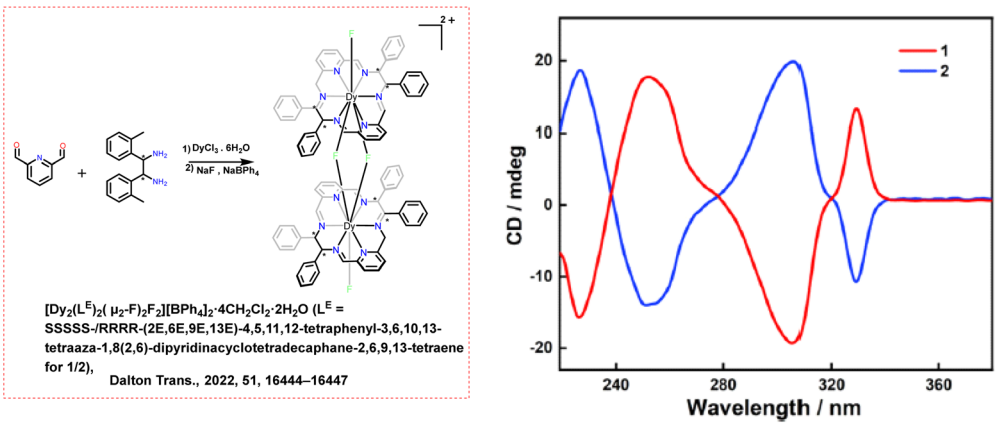

Scheme 47 (Left) Chemical structures of the ligands and Ln complexes (1/2), adapted from ref. 105. (Right) CD spectra of 1 (red) and 2 (blue) in CH_2Cl_2, reproduced from ref. 105 with permission from the Royal Society of Chemistry, copyright [2022].[105]

of this instrument. The PEM acts as a quarter-wave plate oscillating between $+\lambda/4$ and $-\lambda/4$ retardance (Fig. 7b).[108] The intensity at the detector varies when CPL is passed through the linear polarizer and PEM. The square-wave signal of PEM acts as a reference signal to separate the modulated CPL signal from the unmodulated background using lock-in amplification.[108]

Open Access Article. Published on 02 April 2025. Downloaded on 4/4/2026 1:46:32 AM.
This article is licensed under a Creative Commons Attribution-NonCommercial 3.0 Unported Licence.

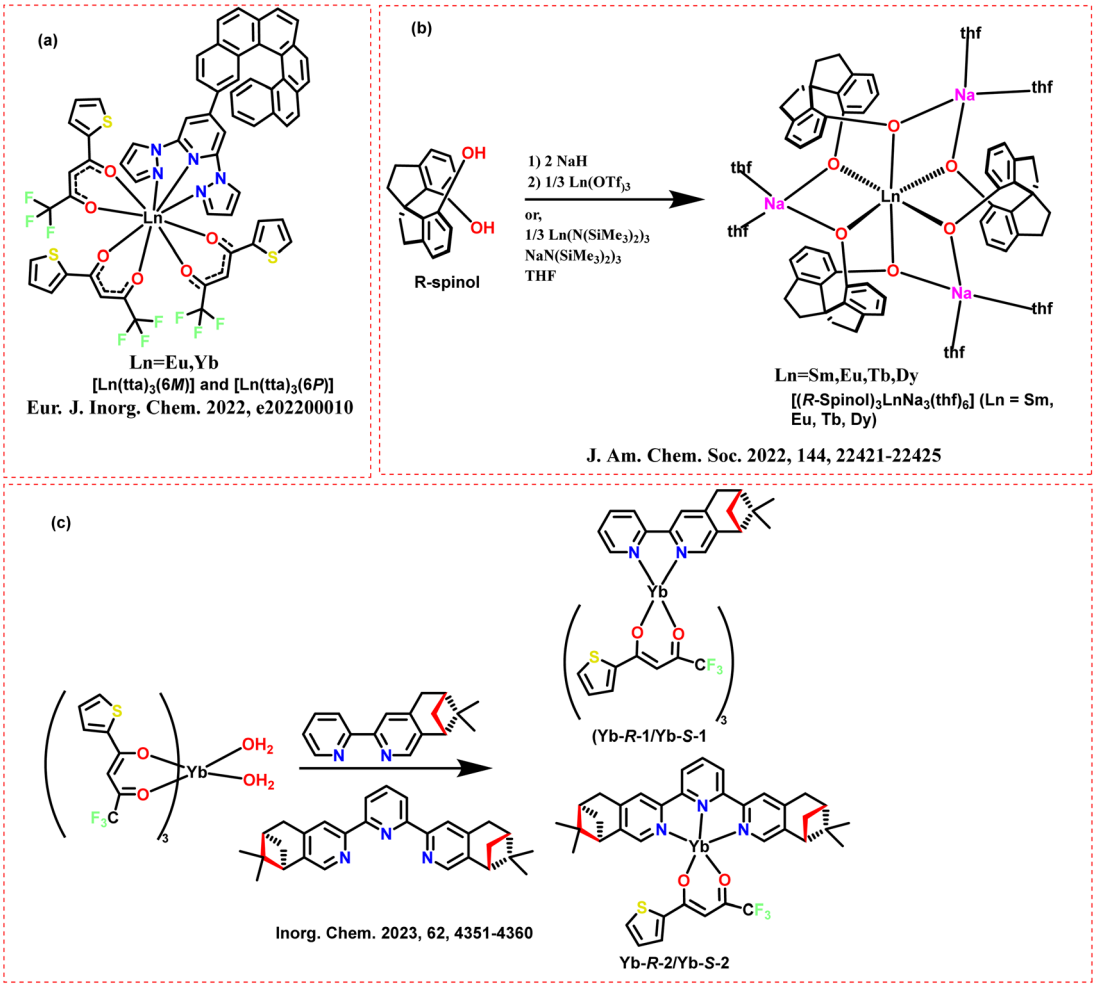

Scheme 48 Chemical structures of the ligands and Ln complexes reported (a) $Ln(tta)_3(6M$ or $6P)$), adapted from ref. 95. (b) ($[(R\text{-Spinol})_3LnNa_3(thf)_6]$), adapted from ref. 96 and (c) ((Yb-*R*-1/Yb-*S*-1)) and (Yb-*R*-2/Yb-*S*-2), adapted from ref. 97.

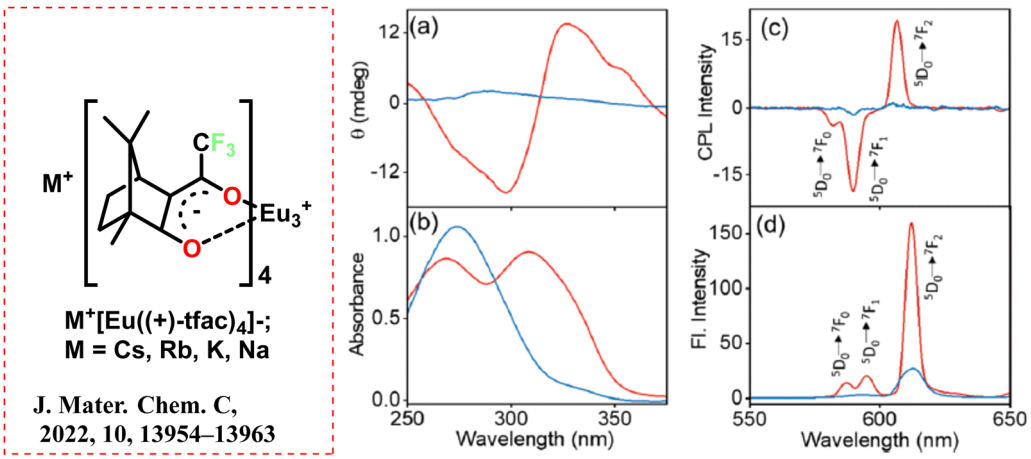

Scheme 49 (Left) Chemical structures of the ligands and Ln complexes ($M^+[Eu((+)\text{-tfac})_4]^-$, where M = Cs, Rb, K, Na).[106] (Right) (a) CD, (b) absorption, (c) CPL and (d) luminescence spectra of $Cs^+[Eu((+)\text{-tfac})_4]$ (red traces) and $Rb^+[Eu((+)\text{-tfac})_4]$ (blue traces) in chloroform. Reproduced from ref. 106 with permission from the Royal Society of Chemistry, copyright [2022].[106]

This journal is © The Royal Society of Chemistry 2025

Open Access Article. Published on 02 April 2025. Downloaded on 4/4/2026 1:46:32 AM.
This article is licensed under a Creative Commons Attribution-NonCommercial 3.0 Unported Licence.

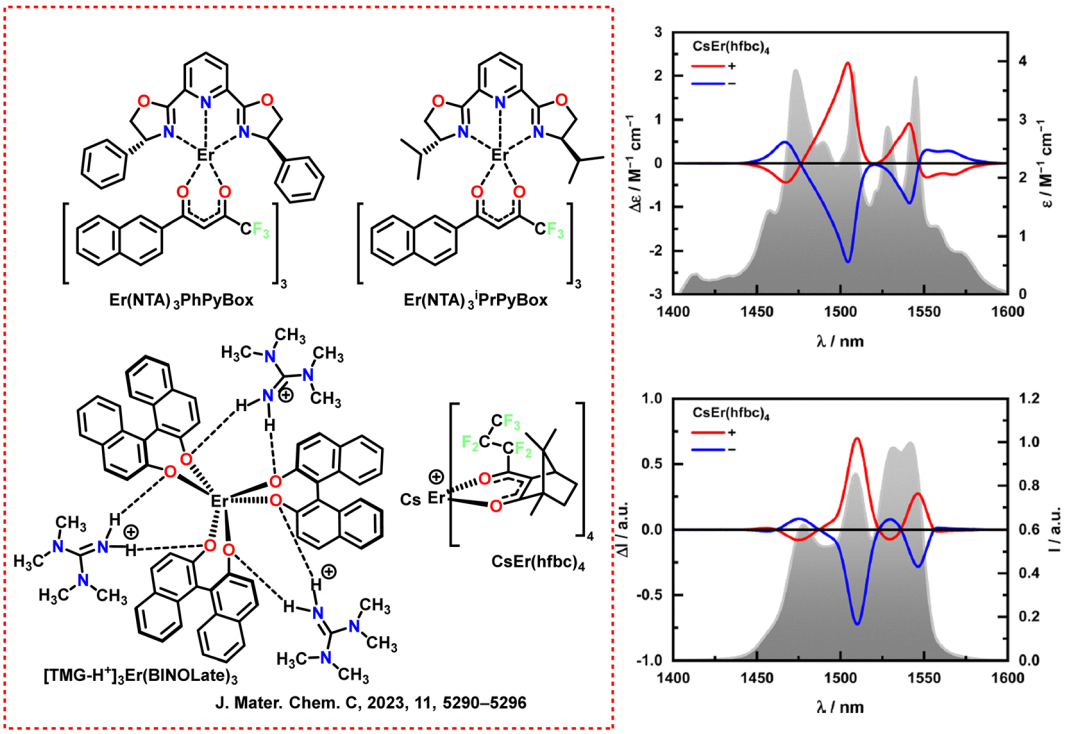

Scheme 50 (Left) Chemical structures of the ligands and Ln complexes ($CsEr(hfbc)_4$, $[TMG\text{-}H^+]_3Er(BINOLate)_3$, and $Er(NTA)_3iPr/PhPyBox$), adapted from ref. 98. (Right) (Top) NIR-CD spectra of $CsEr(hfbc)_4$ (16 mM) with average total absorption traced in the background (in grey). (Bottom) NIR-CPL spectra of $CsEr(hfbc)_4$ (1 mM) with normalised average total emission traced in the background (in grey). Reproduced from ref. 98 with permission from the Royal Society of Chemistry, copyright [2023].[98]

4. Conclusion and outlook

The display industry and the researchers are highly fascinated by the practical applications of the CPL in almost every field of life. The unique properties of CPL emitters have significant implications for various fields, including biological imaging, optoelectronics, and more. As mentioned in the first section, CPL may be produced using a linear polarizer and quarter-wave plate combination, but the brightness of the output light is compromised in this process. Anti-glare filters that combine a quarter-wave plate with a linear polarizer are used in most display devices. However, the aforementioned problem has compelled research to create unique CPL emitters. Thus, research on CPL-based materials is still growing and producing metal complexes, supramolecular assemblies, nano-assemblies, and small organic molecules that emit CPL. Chiral Ln complexes are the best molecular structures to illustrate the high luminescence dissymmetry factor. However, these Ln complexes are poor emissive candidates because they have forbidden electric-dipole 4f–4f transitions and allowed magnetic dipole transitions. Nonetheless, the well-designed antenna ligands can efficiently transmit energy to the Ln metal ions and reduce the complex's symmetry, partially permitting the electric dipole 4f–4f transition. This mini-review article elaborates the basic principles and key factors for assessing CPL activity. This review article discusses small lanthanide complexes with various antenna ligands and distinct chirality transfer and induction from chiral ligands to metal complexes. We have organized this article based on the different binding ligands to the Ln metal ions. The binding ligands comprise β-diketonate-based ligands, cyclen-based ligands, pyridine dicarboxylate-based ligands, multiple oxygen atoms-based ligands, and multiple nitrogen atom-based ligands. We highlight the role of coordination ligands in controlling the antenna effect. For instance, β-diketonates can function as perfect antennas to increase the luminescence of central Ln^{3+} effectively. In this review, we have summarized the chiral lanthanide complexes and their role in CPL. We highlight the significant milestones that have shaped this vibrant area of research to understand how chiral Ln complexes have become essential tools in CPL studies and applications. The highlight the importance of ligand design, coordination chemistry, and the role of chirality in enhancing CPL efficiency. Moreover, we aim to motivate future research by identifying challenges like improving quantum yields, dissymmetry factor, and stability in the chiral lanthanide complexes. This research interest in chiral lanthanide complexes is dignified to contribute to emerging technologies, including advanced optical devices, molecular electronics, and biomedical applications. The continued exploration of multifunctional lanthanide complexes and novel chiral ligands will be vital in pushing the frontiers of these materials.

The detection of CPL is easy using the emission spectrometer equipped with a quarter-wave plate placed at $\pm 45^\circ$ to a linear polarizer. This custom-built CPL spectrometer must be manually adjusted by rotating the quarter-wave plate. This manual adjustment in the quarter-wave plate or the linear polarizer leads to significant errors in the final results. The manual rotation of the quarter-wave plate adds a source of error

Open Access Article. Published on 02 April 2025. Downloaded on 4/4/2026 1:46:32 AM.
This article is licensed under a Creative Commons Attribution-NonCommercial 3.0 Unported Licence.

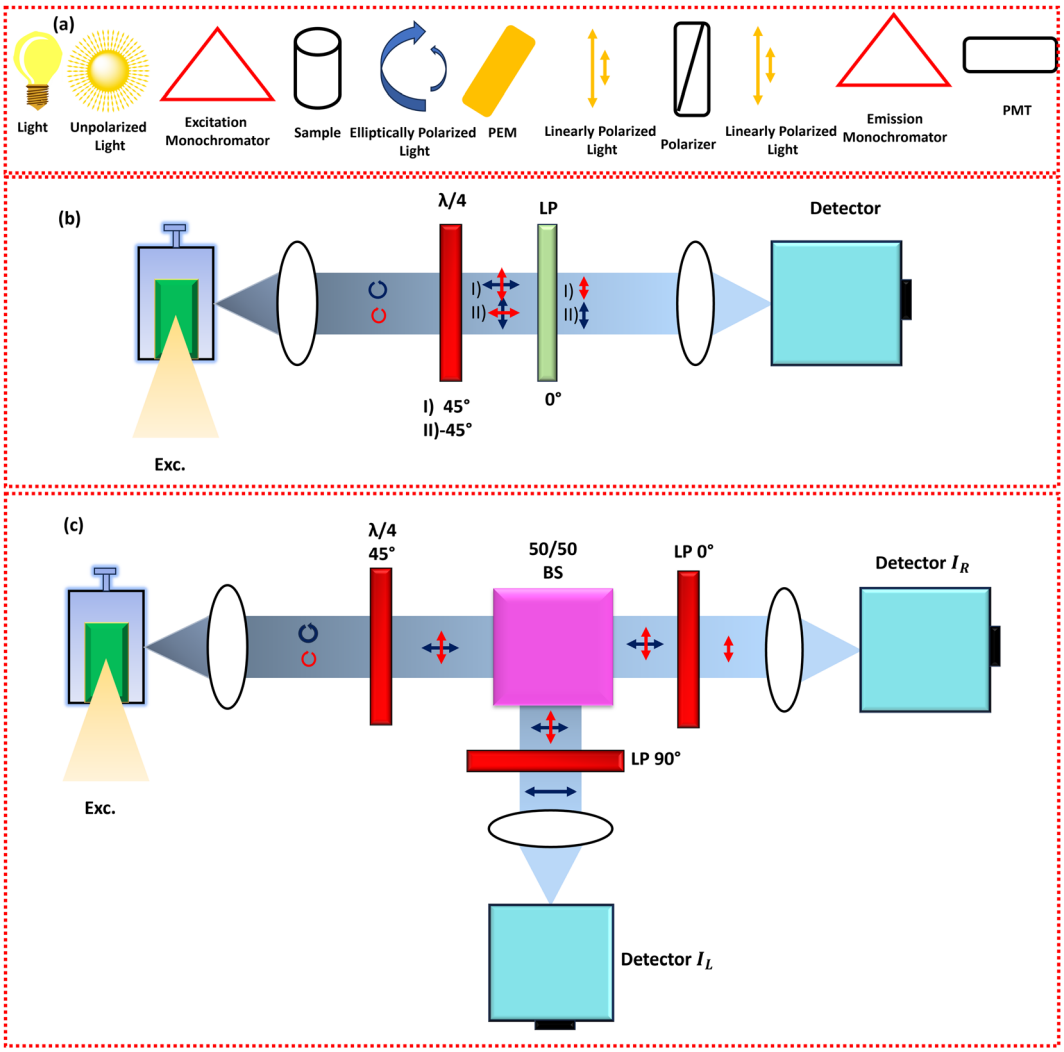

Fig. 6 (a) Basic diagram of CPL instrument (redrawn from ref. 107) (b) and (c) different types of instrument setup for CPL detection. Exc. is excitation, LP is a linear polarizer, BS is a beam splitter, I_L is the intensity of LCP, and I_R is the intensity of RCP. The blue curved arrow is LCP and the red curved arrow is RCP. Explanation for the diagrams is in the main text (redrawn from ref. 108).

and unpredictability. The time delays between LCP and RCP light measurement can also result in sample decay or CPL artifacts. Moreover, this arrangement can be challenging for small dissymmetry factors, while high dissymmetry ($g_{lum} > 0.1$) values can be easily measured. This is why the chiral lanthanide complexes (high dissymmetry values) often rely on custom-built equipment. A PEM-based instrument for the measurement of CPL is superior since it addresses most of the drawbacks of custom-built instruments. Minor dissymmetry factors may also be detected with the help of PEM-based equipment. Thus, the PEM-based CPL instruments have significant major advantages compared to a custom-built spectrometer in terms of data accuracy. These PEM-based instruments increase accuracy by avoiding manual rotation. To maintain consistency across this field, it is recommended to use PEM-based CPL spectrometers.

Lanthanide compounds with a magnetic-dipole-allowed transition are preferred to produce highly polarized light. These materials can be used to generate CP-OLED devices by using them as emissive layers. Bari's group demonstrated CP-OLEDs devices based on lanthanide compounds in 2015, using mononuclear $CsEu(hfbc)_4$ with the largest g_{lum} factor of 1.38.[54] It is possible to formulate security inks using CPL emitters. These chiral emitters emit CPL light when excited with the light. As human eyes are not sensitive enough to detect polarized light orientation, CPL can be a security measure instead of a traditional fingerprint method.[17] External visual aids such as bandpass filters are typically preferred to selectively filter polarized photons with different orientations to perceive CPL-coded security inks with the unaided eye. Ionic detection can also be done with the help of CPL emitters. The dissymmetry values and the CPL strength play a crucial role here. The fluctuations in the CPL signals of the original chiral lanthanide complexes can be studied to detect the ions. The mechanism of ionic detection includes the binding of the chiral emitter with the ion, which changes its environment. The change in environment results in luminescent changes leading to increased or decreased CPL signals.

 This journal is © The Royal Society of Chemistry 2025

Open Access Article. Published on 02 April 2025. Downloaded on 4/4/2026 1:46:32 AM.
This article is licensed under a Creative Commons Attribution-NonCommercial 3.0 Unported Licence.

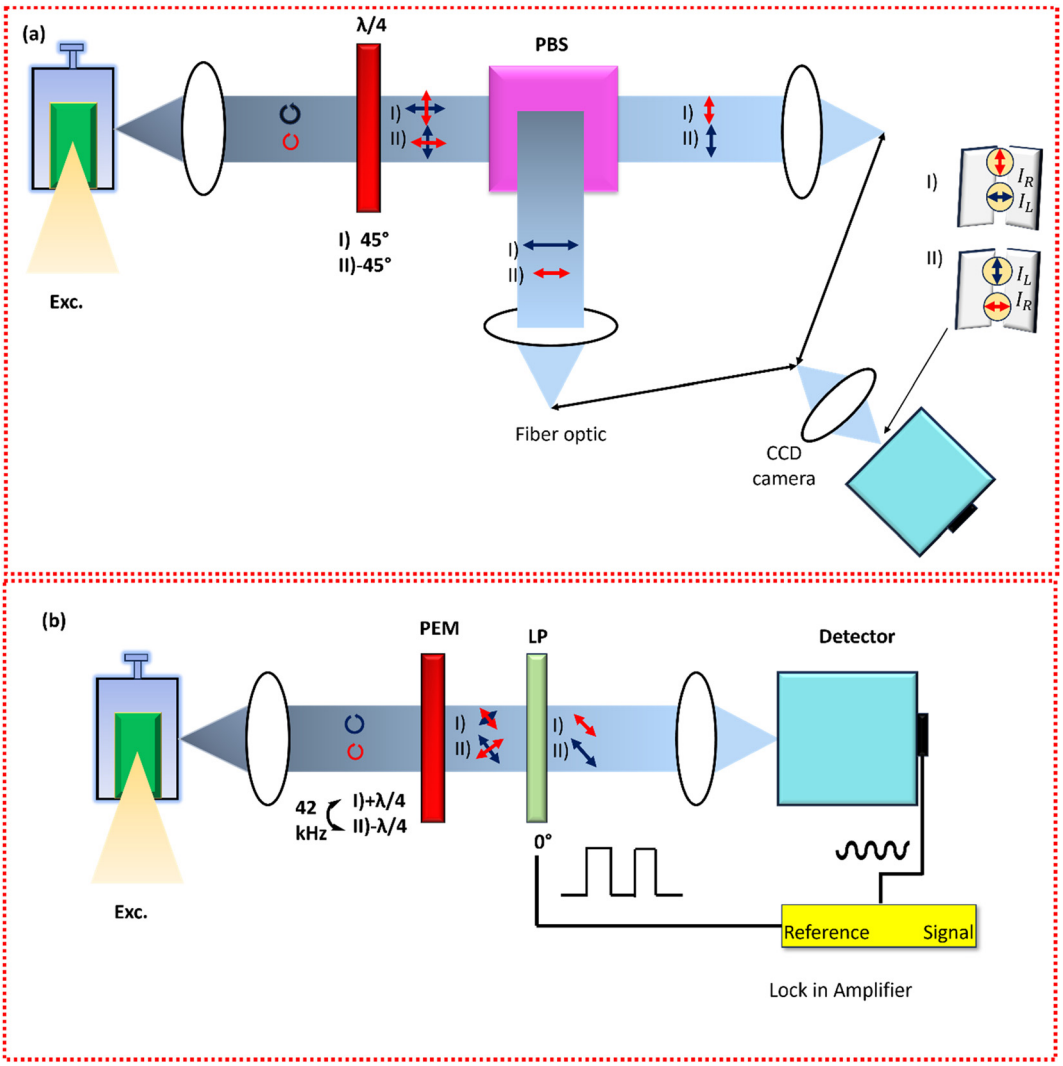

Fig. 7 (a) and (b) Different types of instrument setup for CPL detection. Exc. is excitation, LP is a linear polarizer, PBS is a polarizing beam splitter, I_L is the intensity of LCP, I_R is the intensity of RCP, and PEM is photoelastic modulator. The blue curve arrow is LCP, and the red curve is RCP. Explanation for the diagrams is in the main text. (redrawn from ref. 108).

The binding ability of the ligands is heavily affected by their denticity and hard–soft acid–base concept. Designing a complex with high quantum yield and g_{lum} value is also necessary. The most feasible energy-transferring route to Ln ions is through the triplet state of the ligands. Therefore, the energy gap between the ligands' triplet state and the Ln's excited state energy level plays a crucial role in enhancing the quantum yield of the complex. It has already been mentioned that the gap between the ligand's triplet state and the Ln's excited state should be small. Moreover, the triplet state should be slightly higher than the energy level of the Ln ion. If the triplet state of the ligand is situated at a lower level than the Ln's excited state level, it may act as an energy quencher. To boost the sensitizing efficacy from outer coordinated ligands to Ln^{3+} luminescent centers, ligands need to possess a high molar extinction coefficient and a minimal energy gap between the triplet excited state of the ligands and the excited state of Ln^{3+}.

Material stability and high quantum efficiency are important parameters to consider while designing the ligands for the Ln ions. The devices with long operational lifetimes must have high thermally stable Ln complexes. Also, the fabrication methods of the devices need specific requirements in metal complexes; for instance, the solution-process fabrication method needs the metal complex to be soluble in common organic solvents. Deep NIR region Ln complexes are highly effective in tissue imaging and telecommunications; therefore, expanding the emission range of these complexes is the need of the hour. Developing a composite system of Ln complexes and inorganic/organic materials can open new application pathways. The chiral Ln complexes can be embedded in nanoparticles, MOFs, and polymer matrices to enhance their performance. Synthesizing stimuli-responsive chiral Ln complexes (pH, light, and temperature sensitive) enables numerous application options for CPL emitters.

Open Access Article. Published on 02 April 2025. Downloaded on 4/4/2026 1:46:32 AM. This article is licensed under a Creative Commons Attribution-NonCommercial 3.0 Unported Licence.

TADF ligands are well-known for their high efficiency as they can harness singlet and triplet excitons through reverse inter-system crossing pathways. The structural design of TADF structures is such that the gap between the lowest singlet and triplet energy levels is very small. This small energy gap favors the reverse inter-system crossing of the triplet excitons to the singlet state, enabling them to possess high quantum yields. Kalluvettukuzhy *et al.* synthesized TADF emitters to sensitize Eu(III) efficiently.[110] The TADF molecules can effectively act as photosensitizers for Eu(III). The coordination polymers formed with TADF ligands exhibit high PLQY ranging from 79% to 85% and sensitization efficiencies between 90% and 94% in PMMA films. The TADF ligands have well-aligned energy levels with the excited states of the Eu(III) ions. This optimal energy matching significantly enhances the luminescence quantum yield. The potential of TADF ligands can be extended beyond Eu(III) coordination polymers. This concept could be applied to other organo-lanthanide emitters. They investigated different electronic properties of the developed TADF ligands and found minimal singlet–triplet energy splitting. This minimum energy gap allows for efficient energy transfer to the lanthanide ions. This property is vital for achieving high energy transfer efficiency, making TADF ligands suitable for sensitizing Ln metal ions. By judicious choice of moieties, we can successfully develop the NIR emissive TADF ligands, which can bind to the Ln metal ions. Thus, we can achieve a broadband emission that is beneficial for advanced lighting and display technologies by connecting the high-efficiency NIR TADF antennas to the Ln(III) ions. Combining the NIR TADF ligands with the Ln(III) ions may achieve the broad NIR region with high efficiency. Thus, high-efficiency NIR TADF-based ligands can be complexed with the Ln(III) metal, giving a broad emission with high efficiency.

The self-assembled structures generally help to achieve high dissymmetry factors. Ln complexes generally have a high coordination number which helps them make supramolecular assemblies, including helicates, metallacycles, and metallacages.[111] The symmetry of ligands and metal ions mainly influences the self-assembly of Ln complexes. The symmetry of these moieties is a primary driving force for forming well-defined structures such as duplex, triple, and quadruple helicates.[111] A balance between rigidity and flexibility in the molecular framework is vital for the self-assembly of Ln complexes. The rigid, multi-branched ligands help restrict conformational movement. The rigidity of the molecular framework favors structural stability, and flexible spacers ensure the dynamics to facilitate the self-assembly process.[111] The interaction between ligands and metal centers holds a lock-and-key arrangement. This arrangement is responsible for specific structural control. This can also be termed coordination-driven self-assembly, and it is desirable for the overall stability of the supramolecular frameworks.

Our mini survey will benefit academics across various scientific and display engineering fields. We also hope that our efforts will significantly contribute to the advancement of display technology in the future.

Data availability

The data supporting this article are available in the reported (cited) literature.

Conflicts of interest

The authors have no conflicts of interest.

Acknowledgements

The author DT acknowledges NPDF, SERB, Department of Science and Technology (DST), India (PDF/2023/000022) and VS acknowledges SERB, DST, Government of India (EMR/2016/002462 and CRG/2021/000494) and IIT Hyderabad (IITH/F324/2022-23/SG-138) for the financial support.

References

1 R. Hu, Y. Yuan, M. Gu and Y.-Q. Zou, *Eng. Regener.*, 2022, **3**, 323–338.
2 X.-Y. Luo and M. Pan, *Coord. Chem. Rev.*, 2022, **468**, 214640.
3 Y. Sang, J. Han, T. Zhao, P. Duan and M. Liu, *Adv. Mater.*, 2020, **32**, 1900110.
4 G. Longhi, E. Castiglioni, J. Koshoubu, G. Mazzeo and S. Abbate, *Chirality*, 2016, **28**, 696–707.
5 T. Ikeda, T. Masuda, T. Hirao, J. Yuasa, H. Tsumatori, T. Kawai and T. Haino, *Chem. Commun.*, 2012, **48**, 6025–6027.
6 Y.-H. Kim, Y. Zhai, H. Lu, X. Pan, C. Xiao, E. A. Gaulding, S. P. Harvey, J. J. Berry, Z. V. Vardeny, J. M. Luther and M. C. Beard, *Science*, 2021, **371**, 1129–1133.
7 Z. Chen, C. Zhong, J. Han, J. Miao, Y. Qi, Y. Zou, G. Xie, S. Gong and C. Yang, *Adv. Mater.*, 2022, **34**, 2109147.
8 D.-W. Zhang, M. Li and C.-F. Chen, *Chem. Soc. Rev.*, 2020, **49**, 1331–1343.
9 R. Carr, N. H. Evans and D. Parker, *Chem. Soc. Rev.*, 2012, **41**, 7673–7686.
10 Y. Xu, G. Yang, H. Xia, G. Zou, Q. Zhang and J. Gao, *Nat. Commun.*, 2014, **5**, 5050.
11 J. Kim, J. Lee, W. Y. Kim, H. Kim, S. Lee, H. C. Lee, Y. S. Lee, M. Seo and S. Y. Kim, *Nat. Commun.*, 2015, **6**, 6959.
12 C. He, G. Yang, Y. Kuai, S. Shan, L. Yang, J. Hu, D. Zhang, Q. Zhang and G. Zou, *Nat. Commun.*, 2018, **9**, 5117.
13 Y. Zhang, S. Yu, B. Han, Y. Zhou, X. Zhang, X. Gao and Z. Tang, *Matter*, 2022, **5**, 837–875.
14 A. Nowak-Król, P. T. Geppert and K. R. Naveen, *Chem. Sci.*, 2024, **15**, 7408–7440.
15 D. Schnable and G. Ung, *Inorg. Chem.*, 2024, **63**, 7378–7385.
16 L. Frédéric, A. Desmarchelier, L. Favereau and G. Pieters, *Adv. Funct. Mater.*, 2021, **31**, 2010281.
17 Y. Zhong, Z. Wu, Y. Zhang, B. Dong and X. Bai, *InfoMat*, 2023, **5**, e12392.
18 J. L. Greenfield, J. Wade, J. R. Brandt, X. Shi, T. J. Penfold and M. J. Fuchter, *Chem. Sci.*, 2021, **12**, 8589–8602.
19 A. Nitti and D. Pasini, *Adv. Mater.*, 2020, **32**, 1908021.

 This journal is © The Royal Society of Chemistry 2025

Open Access Article. Published on 02 April 2025. Downloaded on 4/4/2026 1:46:32 AM.
This article is licensed under a Creative Commons Attribution-NonCommercial 3.0 Unported Licence.

20 X. Yang, X. Jin, T. Zhao and P. Duan, *Mater. Chem. Front.*, 2021, **5**, 4821–4832.
21 B. He, Q. Zhong, Q. Dong, X. Yang, S. J. Cowling, W. Qiao, D. W. Bruce, W. Zhu, P. Duan and Y. Wang, *Mater. Horiz.*, 2024, **11**, 1251–1260.
22 C. Liao, Y. Zhang, S.-H. Ye and W.-H. Zheng, *ACS Appl. Mater. Interfaces*, 2021, **13**, 25186–25192.
23 L. Qu, H. Xiao, B. Zhang, Q. Yang, J. Song, X. Zhou, Z.-X. Xu and H. Xiang, *Chem. Eng. J.*, 2023, **471**, 144709.
24 Z. Chen, M. Huang, C. Zhong, S. Gong, V. Coropceanu, J.-L. Brédas and C. Yang, *Chem. Sci.*, 2023, **14**, 6022–6031.
25 S. Freed, S. I. Weissman, F. E. Fortess and H. F. Jacobson, *J. Chem. Phys.*, 1939, **7**, 824–828.
26 S. I. Weissman, *J. Chem. Phys.*, 1942, **10**, 214–217.
27 I. Hemmilä, *J. Alloys Compd.*, 1995, **225**, 480–485.
28 C. K. Luk and F. S. Richardson, *J. Am. Chem. Soc.*, 1975, **97**, 6666–6675.
29 H. G. Brittain and F. S. Richardson, *J. Am. Chem. Soc.*, 1976, **98**, 5858–5863.
30 H. G. Brittain, F. S. Richardson and R. B. Martin, *J. Am. Chem. Soc.*, 1976, **98**, 8255–8260.
31 L. Spaulding and H. G. Brittain, *Inorg. Chem.*, 1985, **24**, 3692–3698.
32 J. L. Lunkley, D. Shirotani, K. Yamanari, S. Kaizaki and G. Muller, *Inorg. Chem.*, 2011, **50**, 12724–12732.
33 L. Llanos, P. Cancino, P. Mella, P. Fuentealba and D. Aravena, *Coord. Chem. Rev.*, 2024, **505**, 215675.
34 Y. Kitagawa, M. Tsurui and Y. Hasegawa, *ACS Omega*, 2020, **5**, 3786–3791.
35 J.-C. G. Bünzli, *Coord. Chem. Rev.*, 2015, **293–294**, 19–47.
36 K. Binnemans, *Coord. Chem. Rev.*, 2015, **295**, 1–45.
37 J. P. Byrne, J. A. Kitchen and T. Gunnlaugsson, *Chem. Soc. Rev.*, 2014, **43**, 5302–5325.
38 J. Gregoliński, P. Starynowicz, K. T. Hua, J. L. Lunkley, G. Muller and J. Lisowski, *J. Am. Chem. Soc.*, 2008, **130**, 17761–17773.
39 E. G. Moore, A. P. S. Samuel and K. N. Raymond, *Acc. Chem. Res.*, 2009, **42**, 542–552.
40 S. R. Banerjee, E. J. Ngen, M. W. Rotz, S. Kakkad, A. Lisok, R. Pracitto, M. Pullambhatla, Z. Chen, T. Shah, D. Artemov, T. J. Meade, Z. M. Bhujwalla and M. G. Pomper, *Angew. Chem., Int. Ed.*, 2015, **54**, 10778–10782.
41 S. D. Bonsall, M. Houcheime, D. A. Straus and G. Muller, *Chem. Commun.*, 2007, 3676–3678.
42 B. Doistau, J.-R. Jiménez and C. Piguet, *Front. Chem.*, 2020, **8**, 555.
43 F. S. Richardson, *Inorg. Chem.*, 1980, **19**, 2806–2812.
44 J.-C. G. Bünzli and C. Piguet, *Chem. Soc. Rev.*, 2005, **34**, 1048–1077.
45 P. Stachelek, L. MacKenzie, D. Parker and R. Pal, *Nat. Commun.*, 2022, **13**, 553.
46 B. Kunnen, C. Macdonald, A. Doronin, S. Jacques, M. Eccles and I. Meglinski, *J. Biophotonics*, 2015, **8**, 317–323.
47 G. H. Dieke, *Spectra and Energy Levels of Rare Earth Ions in Crystals*, 1968.
48 G. Muller, *Dalton Trans.*, 2009, 9692–9707.
49 P. Dorenbos, *J. Lumin.*, 2000, **91**, 91–106.
50 K. A. Forbes, D. S. Bradshaw and D. L. Andrews, *J. Chem. Phys.*, 2019, **151**, 034305.
51 M. Cui, A.-L. Wang, C.-L. Gao, L. Zhou, T. Wu, S. Fang, H.-P. Xiao, F.-C. Li and X.-L. Li, *Dalton Trans.*, 2021, **50**, 1007–1018.
52 T. Harada, H. Tsumatori, K. Nishiyama, J. Yuasa, Y. Hasegawa and T. Kawai, *Inorg. Chem.*, 2012, **51**, 6476–6485.
53 O. G. Willis, F. Zinna, G. Pescitelli, C. Micheletti and L. D. Bari, *Dalton Trans.*, 2022, **51**, 518–523.
54 F. Zinna, U. Giovanella and L. D. Bari, *Adv. Mater.*, 2015, **27**, 1791–1795.
55 F. Zinna, M. Pasini, F. Galeotti, C. Botta, L. Di Bari and U. Giovanella, *Adv. Funct. Mater.*, 2017, **27**, 1603719.
56 F. Zinna, C. Resta, S. Abbate, E. Castiglioni, G. Longhi, P. Mineo and L. Di Bari, *Chem. Commun.*, 2015, **51**, 11903–11906.
57 X. Du, Z. Zhang, C. Gao, F. Li and X.-L. Li, *Dalton Trans.*, 2023, **52**, 17758–17766.
58 Y. Peng, T. Wang, C. Gao, F. Li and X.-L. Li, *CrystEngComm*, 2024, **26**, 3867–3873.
59 J. Yuasa, H. Ueno and T. Kawai, *Chem. – Eur. J.*, 2014, **20**, 8621–8627.
60 S. Di Pietro and L. Di Bari, *Inorg. Chem.*, 2012, **51**, 12007–12014.
61 J. W. Walton, L. Di Bari, D. Parker, G. Pescitelli, H. Puschmann and D. S. Yufit, *Chem. Commun.*, 2011, **47**, 12289–12291.
62 L. Dai, J. Zhang, Y. Chen, L. E. Mackenzie, R. Pal and G.-L. Law, *Inorg. Chem.*, 2019, **58**, 12506–12510.
63 L. Dai, W.-S. Lo, I. D. Coates, R. Pal and G.-L. Law, *Inorg. Chem.*, 2016, **55**, 9065–9070.
64 C. Lincheneau, C. Destribats, D. E. Barry, J. A. Kitchen, R. D. Peacock and T. Gunnlaugsson, *Dalton Trans.*, 2011, **40**, 12056–12059.
65 O. Kotova, J. A. Kitchen, C. Lincheneau, R. D. Peacock and T. Gunnlaugsson, *Chem. – Eur. J.*, 2013, **19**, 16181–16186.
66 O. Kotova, S. Blasco, B. Twamley, J. O'Brien, R. D. Peacock, J. A. Kitchen, M. Martínez-Calvo and T. Gunnlaugsson, *Chem. Sci.*, 2015, **6**, 457–471.
67 S. J. Bradberry, A. Jayant Savyasachi, R. D. Peacock and T. Gunnlaugsson, *Faraday Discuss.*, 2015, **185**, 413–431.
68 J. P. Byrne, M. Martínez-Calvo, R. D. Peacock and T. Gunnlaugsson, *Chem. – Eur. J.*, 2016, **22**, 486–490.
69 D. E. Barry, J. A. Kitchen, L. Mercs, R. D. Peacock, M. Albrecht and T. Gunnlaugsson, *Dalton Trans.*, 2019, **48**, 11317–11325.
70 C. P. Montgomery, E. J. New, D. Parker and R. D. Peacock, *Chem. Commun.*, 2008, 4261–4263.
71 G.-L. Law, C. Man, D. Parker and J. W. Walton, *Chem. Commun.*, 2010, **46**, 2391–2393.
72 D. F. De Rosa, M. Starck, D. Parker and R. Pal, *Chem. – Eur. J.*, 2024, **30**, e202303227.
73 G. Muller, B. Schmidt, J. Jiricek, G. Hopfgartner, J. P. Riehl, J.-C. G. Bünzli and C. Piguet, *J. Chem. Soc., Dalton Trans.*, 2001, **0**, 2655–2662.
74 J. P. Leonard, P. Jensen, T. McCabe, J. E. O'Brien, R. D. Peacock, P. E. Kruger and T. Gunnlaugsson, *J. Am. Chem. Soc.*, 2007, **129**, 10986–10987.

Open Access Article. Published on 02 April 2025. Downloaded on 4/4/2026 1:46:32 AM. This article is licensed under a Creative Commons Attribution-NonCommercial 3.0 Unported Licence.

75 C. Lincheneau, J. P. Leonard, T. McCabe and T. Gunnlaugsson, *Chem. Commun.*, 2011, **47**, 7119–7121.
76 S. Petoud, G. Muller, E. G. Moore, J. Xu, J. Sokolnicki, J. P. Riehl, U. N. Le, S. M. Cohen and K. N. Raymond, *J. Am. Chem. Soc.*, 2007, **129**, 77–83.
77 M. Deng, N. D. Schley and G. Ung, *Chem. Commun.*, 2020, **56**, 14813–14816.
78 N. F. M. Mukthar, N. D. Schley and G. Ung, *J. Am. Chem. Soc.*, 2022, **144**, 6148–6153.
79 M. Seitz, E. G. Moore, A. J. Ingram, G. Muller and K. N. Raymond, *J. Am. Chem. Soc.*, 2007, **129**, 15468–15470.
80 T. Harada, Y. Nakano, M. Fujiki, M. Naito, T. Kawai and Y. Hasegawa, *Inorg. Chem.*, 2009, **48**, 11242–11250.
81 N. Koiso, Y. Kitagawa, T. Nakanishi, K. Fushimi and Y. Hasegawa, *Inorg. Chem.*, 2017, **56**, 5741–5747.
82 M. Tsurui, Y. Kitagawa, K. Fushimi, M. Gon, K. Tanaka and Y. Hasegawa, *Dalton Trans.*, 2020, **49**, 5352–5361.
83 D. Liu, Y. Zhou, Y. Zhang, H. Li, P. Chen, W. Sun, T. Gao and P. Yan, *Inorg. Chem.*, 2018, **57**, 8332–8337.
84 F. Zinna, L. Arrico and L. D. Bari, *Chem. Commun.*, 2019, **55**, 6607–6609.
85 M. Górecki, L. Carpita, L. Arrico, F. Zinna and L. D. Bari, *Dalton Trans.*, 2018, **47**, 7166–7177.
86 J. Yuasa, T. Ohno, K. Miyata, H. Tsumatori, Y. Hasegawa and T. Kawai, *J. Am. Chem. Soc.*, 2011, **133**, 9892–9902.
87 F. Song, G. Wei, X. Jiang, F. Li, C. Zhu and Y. Cheng, *Chem. Commun.*, 2013, **49**, 5772–5774.
88 M. Leonzio, M. Bettinelli, L. Arrico, M. Monari, L. Di Bari and F. Piccinelli, *Inorg. Chem.*, 2018, **57**, 10257–10264.
89 Z.-Y. Liu, D.-C. Liu, X.-K. Huang, J. Gong, Z.-L. Chen, H.-H. Zou, D. Yan and F.-P. Liang, *J. Mol. Struct.*, 2025, **1321**, 139780.
90 J. A. Adewuyi and G. Ung, *J. Am. Chem. Soc.*, 2024, **146**, 7097–7104.
91 S. Mizzoni, A. Sickinger, S. Ruggieri, F. Riobé, L. Guy, O. Maury, B. Baguenard, A. Bensalah-Ledoux, Y. Guyot, S. Guy, M. Sanadar, A. Melchior and F. Piccinelli, *New J. Chem.*, 2024, **48**, 9627–9636.
92 I. M. S. Diogenis, A. G. Bispo-Jr, R. V. Pirovani, L. F. Saraiva, F. C. Gozzo, C. R. D. Correia, I. O. Mazali, R. A. Nome and F. A. Sigoli, *J. Mater. Chem. C*, 2024, **12**, 5097–5107.
93 D. F. Caffrey, T. Gorai, B. Rawson, M. Martínez-Calvo, J. A. Kitchen, N. S. Murray, O. Kotova, S. Comby, R. D. Peacock, P. Stachelek, R. Pal and T. Gunnlaugsson, *Adv. Sci.*, 2024, **11**, 2307448.
94 Y. Tang, M. Jian, B. Tang, Z. Zhu, Z. Wang and Y. Liu, *Inorg. Chem. Front.*, 2024, **11**, 2039–2048.
95 A. Abhervé, M. Mastropasqua Talamo, N. Vanthuyne, F. Zinna, L. Di Bari, M. Grasser, B. Le Guennic and N. Avarvari, *Eur. J. Inorg. Chem.*, 2022, e202200010.
96 B.-A. N. Willis, D. Schnable, N. D. Schley and G. Ung, *J. Am. Chem. Soc.*, 2022, **144**, 22421–22425.
97 X.-L. Li, A. Wang, Y. Li, C. Gao, M. Cui, H.-P. Xiao and L. Zhou, *Inorg. Chem.*, 2023, **62**, 4351–4360.
98 O. G. Willis, A. Pucci, E. Cavalli, F. Zinna and L. D. Bari, *J. Mater. Chem. C*, 2023, **11**, 5290–5296.
99 S. Petoud, S. M. Cohen, J.-C. G. Bünzli and K. N. Raymond, *J. Am. Chem. Soc.*, 2003, **125**, 13324–13325.
100 M. Atzori, K. Dhbaibi, H. Douib, M. Grasser, V. Dorcet, I. Breslavetz, K. Paillot, O. Cador, G. L. J. A. Rikken, B. Le Guennic, J. Crassous, F. Pointillart and C. Train, *J. Am. Chem. Soc.*, 2021, **143**, 2671–2675.
101 J. Wu, G.-L. Wang, Z. Zhu, C. Zhao, X.-L. Li, Y.-Q. Zhang and J. Tang, *Chem. Commun.*, 2022, **58**, 7638–7641.
102 Z. Zhu, C. Zhao, T. Feng, X. Liu, X. Ying, X.-L. Li, Y.-Q. Zhang and J. Tang, *J. Am. Chem. Soc.*, 2021, **143**, 10077–10082.
103 A. Sickinger, M. Grasser, B. Baguenard, A. Bensalah-Ledoux, L. Guy, A. T. Bui, Y. Guyot, V. Dorcet, F. Pointillart, O. Cador, S. Guy, O. Maury, B. L. Guennic and F. Riobé, *Phys. Chem. Chem. Phys.*, 2024, **26**, 15776–15783.
104 A. Sickinger, B. Baguenard, A. Bensalah-Ledoux, Y. Guyot, L. Guy, F. Pointillart, O. Cador, M. Grasser, B. L. Guennic, F. Riobé, O. Maury and S. Guy, *J. Mater. Chem. C*, 2024, **12**, 4253–4260.
105 X. Liu, C. Zhao, J. Wu, Z. Zhu and J. Tang, *Dalton Trans.*, 2022, **51**, 16444–16447.
106 B. Marydasan, K. Suryaletha, A. M. Lena, A. Sachin, T. Kawai, S. Thomas and J. Kumar, *J. Mater. Chem. C*, 2022, **10**, 13954–13963.
107 S. Suzuki, in *Circularly Polarized Luminescence of Isolated Small Organic Molecules*, ed. T. Mori, Springer, Singapore, 2020, pp. 309–325.
108 W. R. Kitzmann, J. Freudenthal, A.-P. M. Reponen, Z. A. VanOrman and S. Feldmann, *Adv. Mater.*, 2023, **35**, 2302279.
109 B. Baguenard, A. Bensalah-Ledoux, L. Guy, F. Riobé, O. Maury and S. Guy, *Nat. Commun.*, 2023, **14**, 1065.
110 N. K. Kalluvettukuzhy, M. R. Maciejczyk and N. Robertson, *Phys. Chem. Chem. Phys.*, 2024, **26**, 18129–18137.
111 X.-Z. Li, C.-B. Tian and Q.-F. Sun, *Chem. Rev.*, 2022, **122**, 6374–6458.

 This journal is © The Royal Society of Chemistry 2025